KINETIC MODELLING OF HIGH MANGANESE STEEL IN LMF PROCESS

KINETIC MODELLING OF HIGH MANGANESE STEEL IN THE LADLE METALLURGY FURNACE

By

MURALIDHARAN KUMAR, B. Eng.

A Thesis Submitted to the School of Graduate Studies

in Partial Fulfillment of the Requirements for the

Degree Master of Applied Science

McMaster University

MASTER OF APPLIED SCIENCE (2016)

Department of Materials Science and Engineering

McMaster University

Hamilton, Ontario, Canada

TITLE: Kinetic modelling of High manganese steel in the Ladle Metallurgy Furnace

AUTHOR: Muralidharan Kumar

B. Eng. (Metallurgical Engineering, PSG College of Technology-affiliated to Anna University, India)

SUPERVISOR: Dr. Ken Coley

NUMBER OF PAGES: 131,

Abstract

Presence of inclusions in high manganese steel are a major concern in the steel making industry, since these particles affect the processing and properties of the steel. During the refining of high manganese steel in the ladle furnace, the types of inclusions present and their growth in the liquid steel, or during solidification of the steel, caused by the addition of manganese and other alloying elements are to be examined.

This research developed a kinetic model for the presence and growth of inclusions in the liquid high manganese steel for the ladle metallurgy process. The diffusion of dissolved elements, and the seed of inclusions for the growth and consumption of inclusions, were both addressed in the model.

The present model for inclusions was coupled to the updated kinetic model for slag-steel reactions in the ladle furnace for high manganese steel. The coupled model allows for verifying the process analysis plant data for the highest manganese concentration presently available in the steel industry.

Finally, an analysis of the coupled kinetic model was performed to compare the effect of the different processing conditions, and the presence and growth of inclusions in the high manganese steel from the ladle metallurgy process.

Acknowledgement

I am grateful for having had the opportunity to pursue my Master's degree, which enabled me to explore an unforgettable experience in an academic, personal and professional manner.

I am extremely thankful for my supervisor, Dr. Ken Coley, for the patience, freedom and independence he granted me throughout the course of my research project. Personally, I truly value and appreciate the academic meetings and discussions with Dr. Ken Coley, which gave me the confidence to carry out the development of the inclusion model for high manganese steel. I am also thankful for Dr. Ken Coley providing me with the opportunities to attend conferences, industrial meeting and lectures, as it served to be a great learning experience to be aware of current developments within the steel industry.

I am thankful for all members of the industrial partners, from the high manganese project, for their continued support, enquires, assistance and observations during the industrial meetings. The input from monthly industrial meetings with the experienced members was a crucial component of this research process.

I appreciate Dr. Stanley Sun, from ArcelorMittal Dofasco, for his support on several discussions related to the industrial process in high manganese steel. The comments and observations provided by those with industrial experience was important for this research.

I take this opportunity to convey my thanks and appreciation for the discussions and comments about my project that I had received from Dr. Neslihan Dogan. I would like to also thank Dr. Anthony Petric, the discussions and observations he provided were helpful for the research project.

It is important to convey my hearty thanks to all my close friends, who had become a part of this incredible journey. I would like to mention a few people: Athinthra, Abirami, Karthika, Kavitha, Preetham, Steel research group colleagues, and those who have directly or indirectly shared their stories, activities, thoughts, emotions and their time. These opportunities have created memories I will cherish for years to come. I appreciate Yousef Tabatabaei and Alan Galindo, for their tolerant responses to my questions during academic discussions, and Nils Andersson for his help with my research.

The financial support provided by the Natural Sciences and Engineering Research Council of Canada (NSERC), and the McMaster Steel Research Center are greatly appreciated.

As very important mention, I dedicate my Master's degree to my family for their constant encouragement and moral support they provided. I want to convey my gratitude to my mom and grandmother for their constant love and affection; and my father for the life lessons and principles regarding patience, hard work and the sacrifices he made to bring me to where I am today. Finally, a special thanks to my brother for having initially nurtured my interest in graduate studies, and his belief in my abilities. I hope that this journey has helped shape me into a better person, and I hope to contribute information of value to society and for the future.

Contents

List of figures

Chapter 2

Chapter 3

Chapter 4

List of tables

Chapter 2

Chapter 3

Chapter 4

List of symbols

*	Indicates a value at the contact interphase between two phases
a_i	Activity of component *i*
A	Reaction area [m^2]
b	Indicates a value at the bulk of the phase
b_i	Mobility of species *i*
C_i	Molar concentration of species *i*[mol/m^3]
C_S'	Modified sulphide capacity in the slag
C_{v_m}	Total molar concentration of the metal phase [mol/m^3]
$C_{v_{sl}}$	Total molar concentration of the slag phase [mol/m^3]
D_i	Diffusivity of component *i* [m^2/sec]
D	Particle diameter [m]
f_i	Activity coefficient of dissolved species *i* in liquid steel
h_i	Henrian activity of the dissolved species *i* in liquid steel
J_i	Molar flux of species *I* [mol.m^{-2}.s^{-1}]
K	Equilibrium constant of reaction
k_m^i	Mass transfer coefficient of the dissolved species *i* in steel [m/s]
k_{sl}^i	Mass transfer coefficient of the species *i* in slag [m/s]
L_S	Equilibrium partition coefficient for desulphurization with the slag, $L_S = \frac{(wt\%\ S)^*}{[wt\%S]^*}$
L_S'	Equilibrium partition coefficient for desulphurization with the slag, $L_S = \frac{(X_{S,sl}^*)}{[X_{S,St}^*]}$
M	Metallic species in the steel
Mw_i	Molecular weight of species *i* [gr/mol]
M_xO_y	Oxide component in the slag
n_i	Number of moles of component *i* [mol]
N_i	Mass transfer rate of species *i* [mol/sec]

N_p	Total number of particles/inclusions in the steel
p_i	Vapor pressure
Q	Argon gas flowrate [Nm^3/sec]
R	Gas constant [$J.mol^{-1}.K^{-1}$]
Sl	Slag
Sl_{mass}	Total mass of slag in the ladle [kg]
St	Steel
St_{mass}	Total mass of steel in the ladle [kg]
T	Temperature [K]
t	Time [sec]
Tol	Mathematical tolerance in the numerical method
Δt_q	Time step for the time integration of the kinetic model [sec]
t_q	Time coordinate in the kinetic model [sec]
V	Volume of the phase [m^3]
v_i	Velocity of species i [m/sec]
V_m	Molar volume[m^3/mol]
[wt% i]	Weight percent of dissolved species *i* in steel
(wt% i)	Weight percent of component *i* in the slag
X_i	Molar fraction of component *i*
ε	Effective gas stirring energy [W/tonne]
ε_i^j	First order interaction parameter of Wagner's thermodynamic formalism
γ_i	Activity coefficient of component *i*
μ_i	Chemical potential of component *i* [J/mol]
ρ	Density [Kg/m^3]
ρ_i^{ij}	Second order interaction parameter of Wagner's thermodynamic formalism
Λ	optical basicity

Declaration of achievement

This master's thesis was written by Muralidharan Kumar under the supervision of Dr. Kenneth Coley.

The original contribution to this thesis was made by Muralidharan Kumar and consist of mathematical development and theoretical analysis for the kinetic model for to predict the presence and growth of inclusions in liquid steel with high manganese content. The kinetic model for growth of inclusions was coupled to a kinetic model for slag-steel reactions previously developed by Graham & Irons(2008). The slag-steel model was extended by Muralidharan Kumar to include high manganese steel.

The supervisor of this research project Dr. Kenneth Coley actively participated on offering guidance, orientation and discussion analysis to achieve the objective of this research. Dr. Coley provided important suggestions and information on the development of the coupled kinetic model for inclusions in high manganese steel.

1 Chapter

Introduction

1.1 Background of the research

Recent trends have focused on the development of stronger steels with better properties for automobile applications, because of consideration stringent safety, environmental policy on greenhouse gas emissions, and increased use of aluminum in the automobile industry. Recently researchers have drawn attention to the development and production of the next generation of Advanced High Strength Steels (AHSS), including Twinning Induced Plasticity (TWIP) steels and Third Generation Advanced High Strength Steels,

Major challenge in the development of third generation AHSS and TWIP steels are the production process of high alloy steels, while considering cost. Although, steelmakers are well versed in making low alloy steels using a cost efficient production process, Ladle Metallurgy Furnace (LMF) simulations and models are necessary for a better understanding of the process.

Though there is a shortage of literature focusing on the production process techniques for high manganese steel, recent literature highlights advances by POSCO, who have taken TWIP steels to commercial level production(Chin et al., 2015), however the production techniques have not been revealed. For better prediction of the conditions in the ladle metallurgy process, thermodynamic models coupled with kinetic models can be used

to predict the liquid steel, slag, and inclusion behavior during the ladle process. It offers cost savings to steelmakers by reducing the number of costly experimental trials required.

Ladle refining has been a focal point for numerous researchers over the years, due to its implications on the final chemistry, properties and quality of the steel. After this process, the final composition of the steel cannot be changed. Non-metallic inclusions play a major role in influencing the quality of the steel, however there are not many models available for predicting their presence and growth, and none to the authors knowledge that have been validated for high manganese steel.

Non-metallic inclusions are always associated with steel and there are various factors influence their formation and growth which includes steel composition, production techniques, reactions within the steel, slag-steel interactions, and steel-refractory interactions. The current research was aimed at predicting the and kinetics of important reactions in LMF processing of high manganese steel.

1.2 Objectives of the research

The objectives of this research project are :

- Modify the previously developed slag-metal-inclusion model, to accommodate high manganese steel.

- Develop a mathematical kinetic model to predict the formation and growth of major inclusions in high manganese steel.

- Couple the inclusion model to the process model for slag-metal reactions.

- Validate and verify the updated slag-metal-inclusion model for high manganese steel using the processing parameters from industrial plant data.

1.3 Outline of the thesis

This thesis has five chapters. The first chapter introduces and describes the purpose of the current research and the main objectives in pursuing this research. The second chapter presents a literature review of topics in secondary steelmaking, particularly pertaining to refining of high manganese steel and includes a detailed discussion on the different experimental work conducted on high manganese steel and prediction of inclusions. The literature review also highlights the updates required to the previously developed kinetic model for slag-metal-magnesium aluminate inclusion reactions.

The third chapter describes the proposed updated slag-metal-inclusion model, providing a detailed analysis related to high manganese steel. It proposes a kinetic model for formation of expected (Manganese Sulphide - MnS, Aluminum Nitride - AlN) inclusions present in the high manganese steel. This model considers the kinetic interactions of dissolved manganese and sulphur to form MnS inclusions, and aluminum and nitrogen to form AlN inclusions. It also details the approach used to couple the inclusion model to the model of slag-metal reactions in the ladle furnace and specifically addresses its use for high manganese steel.

The fourth chapter details the approach used to analyze the coupled slag-steel-inclusion model for high manganese steel. This includes the industrial verification of the model for high manganese steel by comparing it to the highest manganese content in steels that are

currently produced by our industrial collaborators. Additionally, this chapter includes a sensitivity analysis of the updated coupled model for the inclusion formation in the steel. Finally, a brief analysis on the shortcomings of this slag-steel –inclusion model is presented.

The fifth chapter presents the major conclusions and results gathered from this research, along with suggested directions for future research.

2 Chapter

Literature review

2.1 High manganese steel

For the past two decades, extensive research studieshave focused on the development of Advanced High Strength Steels (AHSS). The AHSS includes Dual Phase (DP) steels, High Strength Low Alloy steels (HSLA), Transformation Induced Plasticity (TRIP) steels, Twinning Induced Plasticity (TWIP) steels, and medium manganese steels (Bouaziz, Zurob, & Huang, 2013). Recently, a majority of the research has been focused on the development of third generation AHSS steels, due to an interest in the mechanical properties of high manganese steel. It received considerable attention, owing to the increasing demand for high-performance auto materials for the automobile manufacturing industry (Kwon, Lee, Kim, & Chin, 2010; Grajcar, Galisz, Bulkowski, Opiela, & Skrzypczyk, 2012), cryogenic applications (Choi, Lee, Park, Han, & Morris Jr., 2012), and the military and transportation industry (Bartlett & Van Aken, 2014). It possesses a good combination of strength and elongation properties, as shown in figure (2-1), in comparison to other types of steels, including toughness, fatigue resistance, and welding properties.

The mechanical properties are mainly controlled by the chemical composition of the steel. In high manganese steel, manganese is a major alloying element, accounting for a larger weight percentage (Hils et al., 2015).

Regarding the major alloying elements in high manganese steel, Table (2-1) gives the approximate range of contents currently being studied.

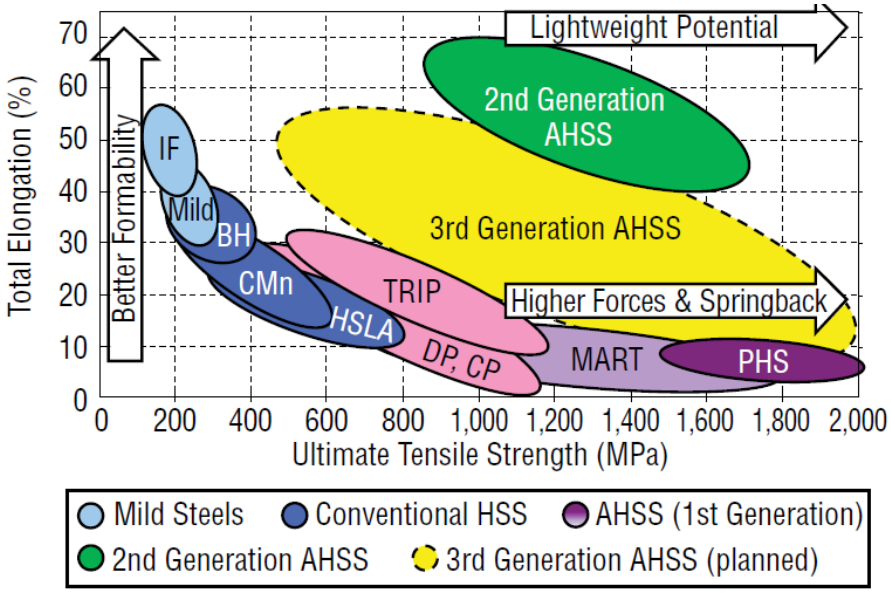

Figure 2-1: Third generations of Advanced High Strength Steels (AHSS) (Billur, Dykeman & Altan, 2014)

Table 2-1: High Manganese steel composition, 3rd generation-AHSS)(Aydin, Essadiqi, Jung, & Yue, 2013)

Major elements in high manganese steel	% Weight
Mn	5 - 11.0
Al	0.0 - 3.0
Si	0 - 3.0
C	0.1 - 0.2
Fe	Remaining

2.2 Process Metallurgy of steel making

Typical modern integrated steel plants have several stages comprised of ironmaking, primary and secondary steelmaking, continuous casting, hot rolling and finishing process for the production of steels. Figure (2-2) shows the stages of the steel production processing route. First, ironmaking involves production of the hot metal from reductions of the iron ores using either the blast furnace process or the direct reduction process. The primary

liquid steel is produced, from either pig iron or recycled steel, through two different practices, namely, Basic Oxygen Furnace or the Electric Arc Furnace. Basic Oxygen Furnace (BOF) has oxygen converters, which convert the hot metal from the iron making process to molten steel which contains low carbon and phosphorous. The Electric Arc Furnace (EAF) operates by melting scrap or recycled metals to produce the primary liquid steel. Subsequently, the molten primary steel is treated in a secondary refining process, called the Ladle Metallurgy Furnace (LMF). This process is done o achieve the desired chemical composition, homogenization, make the required alloy additions, and to maintain the temperature of the molten steel.

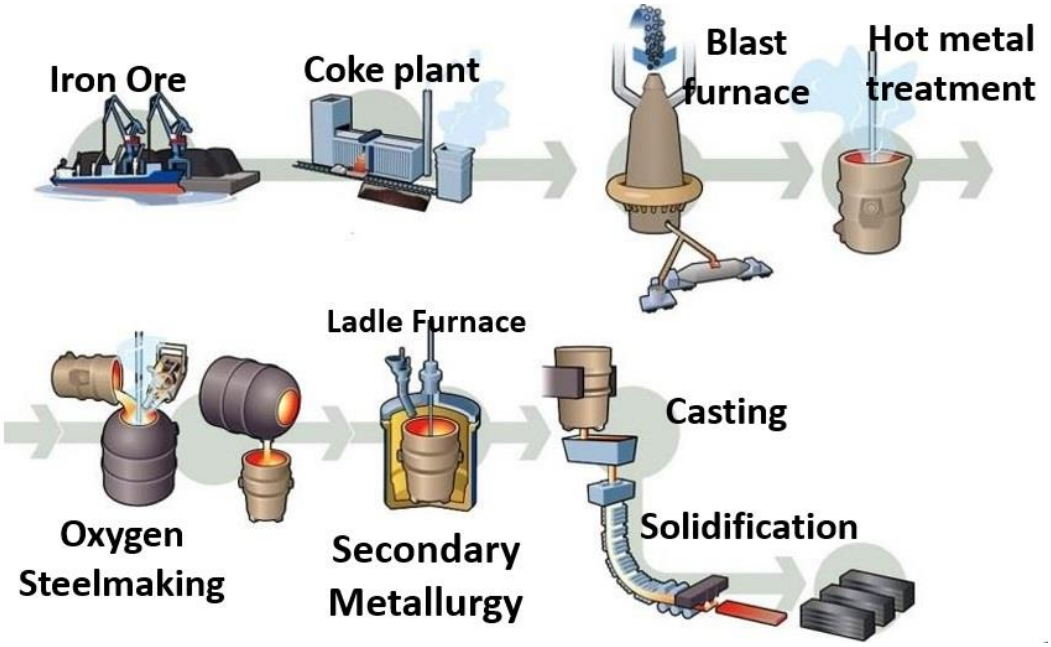

Figure 2-2: Process routes in a modern Integrated steel plant
(Image source: http://www.ssab.com/en/Products--Services/About-SSAB/Steel-making-process/)

Finally, the treated molten steel is cast with the help of a tundish to assist the continuous casting process that produces solidified blooms, billets or slabs. Based on the customer's requirement, these blooms, billets or slabs are charged into hot rolling mills and

finishing mills to reduce the cross sectional area of the cast steel (Ghosh, 2001).

Although the above mentioned processes in the steelmaking plant vary for different conditions and requirements of the steels produced but the stages undertaken in any steelmaking plant remain essentially the same. Integrated steel plants make different grades of steels based on the steel chemistry, including low alloy steels. Most of the alloy additions are carried out during the secondary steelmaking process. Steelmakers have been resistant towards second generation TWIP steels containing very high manganese contents, hence third generation steels have gained greater popularity recently due to their mechanical properties at a more reasonable production cost.

2.3 Secondary Steelmaking process

Secondary steelmaking has become an integral feature of modern steel plants. Different processes applied to liquid steel after the initial steelmaking process, prior to the continuous casting process, are considered part of secondary steelmaking. The tolerance level of impurities and inclusions are lower in continuous casting than ingot casting, and this made secondary refining a critical component in order to control the impurities found in the liquid steel. Ladles containing primary liquid steel are positioned in a car at LMF stations. Ladle Metallurgy Furnace (LMF), as shown in figure (2-3), has graphite electrodes that heats the molten steel, using an electric arc to regulate the temperature in the ladle. Argon stirring is done from the bottom of the ladle, however in some plants induction stirring is carried out in place of argon stirring. Using bottom gates, molten steel from the ladle is teemed into the tundish for casting.

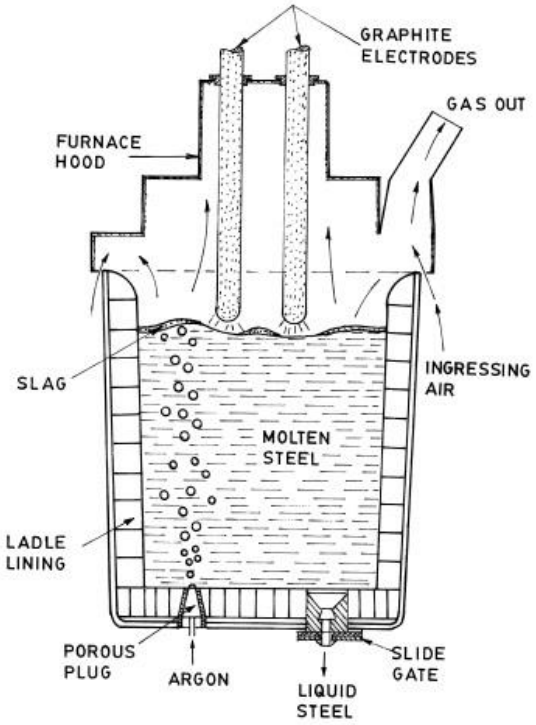

Figure 2-3: Schematic diagram of Ladle Metallurgy Furnace (Ghosh,2001)

The top of the ladle is enclosed with a furnace hood equipped to handle alloying additions. It is also used for composition adjustments in the steel chemistry and additional refinements through deoxidation and desulphurization. Most ladle plants are equipped with wire injection for small and controlled alloy additions at the end of the process, called trimming of steels, and for calcium treatment. Inclusions in steels are caused by harmful impurities such as oxygen, sulfur and nitrogen. The major detriments caused by these inclusions can lead to the loss of mechanical and corrosion properties. Each element has its own influence on the steel properties. Erosion of refractory lining in the ladle and clogging of the nozzles are considered to be significant problems caused by inclusions in the LMF (Ghosh, 2001).

The major objectives of secondary steelmaking are (Srinivasan, 1989):

i. Major alloy additions are carried out in this process and controls the composition of the steel to the aim chemistry.

ii. Maintaining the temperature of the liquid steel and attaining the recommended teeming temperature.

iii. Degassing the liquid steel from nitrogen, oxygen and hydrogen control.

iv. Homogenization of composition, temperature in the liquid steel bath and inclusion floatation through argon purging.

v. Modification of inclusions, desulfurization, deoxidation by alloy additions or wire injection in the ladle**.**

2.4 Treatments in the steelmaking process

2.4.1 Deoxidation

Steelmaking is a process of selective oxidation of impurities in molten iron (Ghosh, 2001). Excess oxygen in the steel causes defects during solidification, such as blowholes and non-metallic inclusions, because the solubility of oxygen in the solid steel is smaller in comparison to the solubility limit in liquid steel. Control of the oxygen content in the steel bath is very important during steelmaking and it is carried out by the deoxidation process. It is carried out after the primary steelmaking process, using either aluminum or silicon which have a high affinity for oxygen. After deoxidation in the ladle, the dissolved oxygen content in the steel decreases drastically, resulting in nitrides, sulphides, or mixed inclusions, which form as precipitates in the liquid steels (Choudhary & Ghosh, 2008).

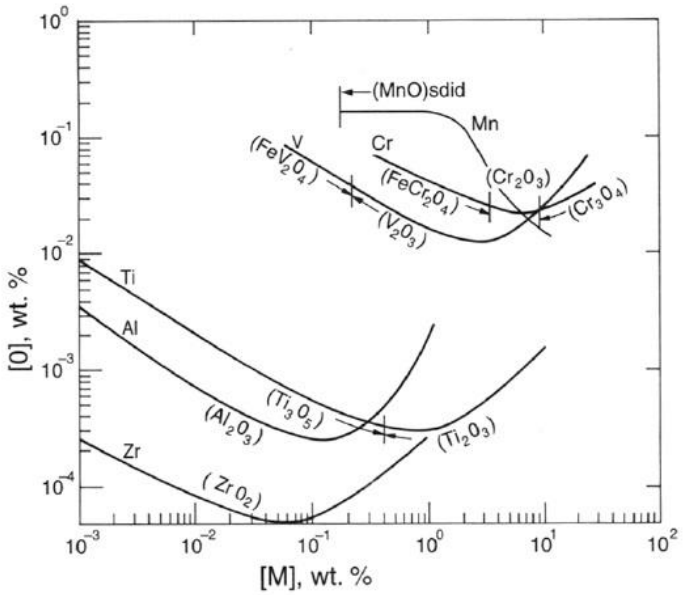

Figure 2-4: Deoxidation equilibria potential in liquid iron at 1873K (Ghosh, 2001)

Aluminum acts as a deoxidizer, however deoxidation products such as alumina inclusions have been proven to be harmful for the steelmaking process and the final product (Xin et al., 2015). Figure (2-4) shows the deoxidation equilibria in liquid iron at 1873 K, for the different elements shown, we can infer from this diagram that Manganese (Mn) is a relatively weak deoxidizer. Zirconium (Zr) is the strongest deoxidizer among the elements showed, followed by aluminum. There are lots of deviations observed in the plot, most of which are caused by strong negative interactions between the deoxidizer and oxygen in the steel (Ghosh, 2001). During deoxidation, if more than one deoxidizing agent is used, it is called mixed deoxidation. The steels that are not deoxidized are termed unkilled steels, the oxygen content in the liquid steel will range from 200-900 ppm based on the processing conditions.

$$[C] + [O] = CO_{(g)} \qquad (2\text{-}1)$$

The steel melt should be well deoxidized and desulphurized before attempting to

remove the dissolved nitrogen in the liquid steel through vacuum degassing. The desorption rate of nitrogen would be retarded by the presence of oxygen and sulfur in the liquid steel (Ghosh, 2001).

2.4.2 Desulphurisation

In general, sulphur is considered a harmful impurity, since it causes hot shortness, affects the corrosion properties of the steel, and has a deleterious effect on mechanical properties. Very little removal of sulfur takes place during the primary steelmaking process. At the end of EAF and BOF processes, sulphur ranges from 150 ppm to 400 ppm and 100 ppm to 200 ppm respectively. Desulfurization is an important step in the refining of high-quality steels with target sulphur content below 20 ppm. During secondary steelmaking operations, the control of dissolved sulphur content, at very low levels, requires the knowledge of the properties of metallurgical slags. It is an exchange of O and S between the steel and slag.

$$[S] + (O^{2-}) = [O] + (S^{2-}) \quad (2\text{-}2)$$

Desulfurization occurs as a reaction between steel and top slag, and with slag droplets generated by inert gas stirring. (Helmut, Xie, Thorsten, & Wolfgang, 2003).

The corresponding equilibrium constant of sulphur, K_S at slag-steel reaction is:

$$K_S = \frac{(a_{S^{2-}})[h_O]}{[h_S](a_{O^{2-}})} = \frac{(\gamma_{S^{2-}})(wt\%S)[h_O]}{f_S.[wt\%S](a_{O^{2-}})} \quad (2\text{-}3)$$

From (2-3) the equilibrium distribution of sulphur between the slag and steel interface, L_S is

$$L_S = \frac{(wt\%S)^*}{[wt\%S]^*} = \frac{K_S(a_{O^{2-}})f_S^*}{(\gamma_{S^{2-}})[h_O^*]} = C_S'.\frac{f_S^*.K_S}{[h_O^*]} \quad (2\text{-}4)$$

Where, K_S is the equilibrium constant of sulphur, L_S is sulphur partition ratio, C_S' is

the sulphide capacity, $a_{S^{2-}}$, $a_{O^{2-}}$ represents the activity of sulphur and oxygen in the slag, respectively, and h_S, h_O denote the Henrian activity of sulphur and oxygen in the steel.

For a given steel composition, the equilibrium partitioning ratio of sulphur between slag and metal increases with higher slag sulfide capacity and lower oxygen activity within the steel, which demonstrates the significance of having a low oxygen potential at the slag-steel interface. FeO and MnO components are the major source of oxygen for the steel. The sulfide capacity (C_S') depends on the slag composition and on the given temperature. It can be defined as the ability of the slag to absorb sulphur, and capacity of slag to hold sulphur as sulphides. The sulphur partition ratio (L_S) is an equilibrium distribution of sulphur between the slag and steel. Hence for good desulfurization, a large value of L_S is required. The desulphurization kinetics analyzed by Ghosh (2001) found it to behave approximately as a first order reversible process, with respect to the concentration of sulfur within the metal. The expression for rate of change in the bulk content of sulphur can be written as:

$$\frac{d[wt\%S]}{dt} = -\frac{k_m.A}{V}\left[[wt\%S] - \frac{(wt\%S)}{L_S}\right] \qquad (2\text{-}5)$$

k_m is the mass transfer coefficient of sulphur in the liquid metal [m/sec], A is the slag-steel interfacial area [m^2] and V is the volume of the steel [m^3]. L_S is the equilibrium distribution of sulphur between the slag and steel interface. For the interphase mass transfer between the steel and slag in the ladle, k_m and A are a function of stirring power ε. Therefore, the amount of slag composition, temperature and the liquid bath stirring condition (time, intensity) are important process parameters for steel desulfurization.

Different approaches have been proposed to correlate the sulfide capacity with the composition of slags. Among the most popular models are those that are based on the

optical basicity concept (Sosinsky, Sommerville, & McLean, 1986), which expresses the sulfide capacity as a linear function of slag compositions. Optical basicity can be described as a measure of basicity or the electron donor power of oxides, which is used to relate the slag composition to sulphide and phosphate capacity. The merit lies in the simplicity of the mathematical expressions.

2.4.3 Gas stirring in the ladle furnace

Secondary steelmaking deals with liquid-state processing. The molten steel in the ladle is stirred by inert gas, usually argon, injected through one or more porous plug located at the bottom of the ladle. Besides promoting chemical reactions, stirring has several purposes in the ladle. This includes homogenization of the composition and temperature in the melt, dissolution of alloying elements added during the process, deoxidation, decarburization (Deo & Boom, 1993), separation of non-metallic inclusion from the steel melt, loss and gain of heat content in the melt, and promotes mass transfer for the slag-steel reactions (Ghosh, 2001). The buoyancy of the injected gas from the porous plug causes stirring energy, effective stirring power given by equation (2-6) and ε [W/tonne] can be calculated with the expression (Pluschkell, 1981).

$$\varepsilon = \left(\frac{101330}{273}\right).\left(\frac{Q.T}{M}\right).ln\left(\frac{\rho.g.h}{101330}\right) \quad (2\text{-}6)$$

Where Q is the argon gas flow rate [Nm^3/s], T is the temperature [Kelvin], M is the total mass of the steel [kg], ρ is the steel density [kg/m^3] and h is the depth of the gas injection [m]. Asai, Kawachi, & Muchi (1983) proposed a relationship between mass transfer rate with the injection of gas flow rate, Q, for water model and molten iron experiments shown in (2-7).

$$k_m \alpha \ Q^n \tag{2-7}$$

n indicates the value of the power influence of Q on mass transfer coefficient in the metal, since the stirring energy is proportional to the gas flow rate. Slag-steel interfacial area in the bath is affected by stirring power.

$$k_m . A \ \alpha \ \varepsilon^n \tag{2-8}$$

From the findings of Kitamura et al. (1991), the mass transfer coefficient in the metal phase (k_m) depends on temperature, stirring energy, concentration in the metal bath, and dimensions of the furnace.

2.4.4 Manganese vaporization during degassing

In vacuum degassing, due to the addition of alloying elements during the LMF process, many elements have high vapour pressure. These are expected to distill off to some extent during the vacuum treatment. Vapour pressure (p_i) for Fe-i binary solutions are carried out (Ghosh, 2001).

$$p_i = p_i^o . a_i = p_i^o . \gamma_i . X_i = p_i^o . \gamma_i . \frac{\frac{W_i}{M_i}}{\frac{W_i}{M_i}+\frac{W_{Fe}}{M_{Fe}}} \tag{2-9}$$

For dilute binary solutions ($W_{Fe} = 100, \gamma_i = \text{constant} = \gamma_i^o$ (Henry law constant)

$$p_i = p_i^o . \gamma_i^o . \frac{W_i M_{Fe}}{100 M_i} \tag{2-10}$$

The temperature dependence of p_i is obtained from the Clausius Clapeyron equation p_i^o vapour pressure of pure element *i* at temperatures under consideration; a_i = activity of element *i* dissolved in liquid iron; X_i= mole fraction of *i* in liquid iron; γ_i = activity coefficient (Raoultian) of *i* in liquid iron; M_i = molecular mass of element *i*.

Table 2-2: Equilibrium vapour pressure of some elements dissolved in the molten iron at 1600°C, (Ghosh, 2001)

Element (i)	M_i	p_i^o at 1600°C, milliatmosphere (approx.)	γ_i^o at 1600°C	p_I, milliatmosphere (calculated)	
				@ $W_i = 0.05$	@ $W_i = 1$
Al	27.0	2.66	0.029	8.0×10^{-5}	1.6×10^{-3}
Cu	63.5	1.2	8.6	4.5×10^{-3}	0.09
Mn	54.9	665	1.3	0.44	8.8
Si	28.1	0.027	0.0013	0.35×10^{-6}	6.9×10^{-6}
Sn	118.7	2.66	2.8	1.7×10^{-3}	0.035
Fe	55.85	0.76	–	–	–
S*	32.1	–	–	10^{-5}	–
P*	31.0	–	–	10^{-9}	–

During degassing, the equilibrium vapour pressure of manganese dissolved in molten iron, at 1600°C, is 665 milliatmospheres, Table (2-2) from (Ghosh, 2001). Loss of manganese and iron occurs during the vacuum degassing process. From an analysis of the flue dust collected at the outlet of the vacuum chamber, the following (in weight percentages) were found: FeO, 17.9; MnO, 47.0; Zn, 1.4; Cu, 2.6; Sn, 0.2; and Pb, 1.0 (Tix, 1956). This indicates that the vapourization of Mn has to be taken into consideration during the production of high manganese steel. Ollette (1961) reported that during vacuum distillation of minor elements from liquid iron alloys, elimination of phosphorous remains constant, but showed increased elimination of other minor elements, including Mn. However, Ghosh (2001) has little information on the significance of the volatilization of minor elements.

2.5 Description of the Cell model for the slag systems

Slag making is an important part of modern steelmaking. To produce effective slags, consideration of thermodynamic properties is of utmost importance. Thermodynamic models are used for predicting the properties of multi-component slag. One such model is the cell model. The cell model belongs to a group of quasichemical approaches to liquid slag thermodynamics and follows the approach proposed by Kapoor & Frohberg (1973) for binary and ternary silicate melts. The Kapoor &Frohberg (1973) model was. later, extended and generalized to multicomponent slags (Gaye & Welfringer, 1984; Gaye, Lehmann, Matsumiya, & Yamada, 1992; Lehmann & Gaye, 1993).

Slags are considered ionic in nature and the liquid slag phase is described in terms of cells; each cell contains an anion surrounded by two cations. Two sublattices are assumed to exist; one filled with anions assumed to have the same valency, and a cationic sublattice, where sites are filled in decreasing order of the charge(e.g. Si^{4+}, ….,Ca^{2+}). The structure of the cell is described in i-K-j cells, where 'K' represents the anions (oxides, sulphide or fluorides) surrounded by cations 'i' and 'j'. Cells may be either symmetrical (i-K-i) or asymmetrical (i-K-j). Each cell is represented by R_{ij}^{K}, denoting a fraction of i-K-j cells for a random distribution of cations on their sublattice.

There are formation and interaction energy parameters associated with each cell, these are binary parameters and are assumed to be independent of temperature.

Formation energy parameters

The energy, W_{ij}^{A}, represents the energy of formation of an asymmetric cell from two symmetrical cells according to the reaction (2-11).

$$\frac{1}{2}(i-A-i)+\frac{1}{2}(j-A-j)=(i-A-j) \quad (2\text{-}11)$$

W_{ii}^{A}, represents the stability of a symmetric cell based on the central anion, A, relative to the equivalent cell with a central oxygen anion according to the reaction (2-12).

$$(i-O-i)+A=(i-A-i)+O \quad (2\text{-}12)$$

Interaction energy parameters

Various cells are assumed to be distributed randomly and interactions between the cells are represented by, for example E_{ij}^{A}, which is the interaction between cells of type (i-A-i) and (i-A-j). One independent cell interaction energy parameter is used per binary system in the liquid oxide model. E_{i}^{AB}, in a polyanionic system represents the interaction between (i-A-i) and (i-B-i) cells. For some systems, linear dependence, as a function of composition, has been adopted for both the formation and the interaction parameters.

The formation and interaction energy parameters for multicomponent slags are used for calculating the mole number of cells, R_{ij}^{K}. This is accomplished by the maximization of the partition function under a mass balance constraint for the anions and cations, from which Gibbs free energy of the system is obtained. Chemical potential and activities are calculated from Gibbs free energy using thermodynamic expressions for multicomponent systems. One of the useful features in the cell model is that the structural information, in terms of the fraction of free, bridging, and non-bridging oxygen, can be calculated to describe the degree of polymerization of silicate melt in the slag system. Li, Morris, & Robertson (1998) correlated the thermodynamic properties of slags with the cell model, and calculated values with reasonable agreement for ferro manganese slag, which had a high wt% of MnO.

Gaye & Lehmann (1997) expanded the cell model to oxysulphide systems, however some of the binary parameters for different components in the slags were not available, for usage in the cell model.

According to Zhang, Sun, & Jahanshahi (2007), there is a good description of the binary system in the cell model using binary parameters, disagreement between the model and experimental data grows as Al_2O_3 content in the slag increases in the ternary components. This is caused by the inability of the model to account for complex behavior in the system by mixing of two binary silicates CaO-SiO_2 and Al_2O_3-SiO_2 with uneven interactions. Examination of the behavior of the various components to introduce ternary parameters of the cell model, was performed to account for the effect of a third component, C, on an A-B binary system. In order to improve the accuracy of the model, an approach was carried out to include ternary parameters for CaO-Al_2O_3-SiO_2 system. When there are only cell formation energy terms for binary parameters W_{ij}'s were expressed as

$$W_{ij} = W_{ij}^{(0)} + W_{ij}^{(1)}.X_i + W_{ij}^{(2)}.X_i^2 \qquad (2\text{-}13)$$

Ternary parameters are expressed by including, W_{ij}

$$W_{ij} = W_{ij}^{(0)} + W_{ij}^{(1)}.X_i + W_{ij}^{(2)}.X_i^2 + \sum_{k=1\neq i,j}^{m} W_{ijk}\frac{X_k}{(1-X_i)} \qquad (2\text{-}14)$$

where $W_{ij}^{(0)}, W_{ij}^{(1)}, W_{ij}^{(2)}$ are coefficients obtained by fitting the experimental data of the binary systems, X_i *and* X_k are the mole fraction of component *i* and *k*; m is the number of components in the slags.

Recently in terms of the development of thermodynamic modelling, ArcelorMittal Maiziéres worked on the development of the Generalized Central Atom (GCA) (Lehmann

& Zhang, 2010) model, for modelling liquid slag and the liquid steel phase to improve the prediction of the cell model for metallurgical slags, and for the prediction of properties for high alloyed liquid steels.

2.6 Kinetic model for ladle metallurgy furnace

Process models are a system of equations and conditions which are solved numerically or using analytical solutions, through computational techniques, to behave like a real life process. The process model serves different purposes, which include providing a better understanding of the fundamentals, helping in evaluation and validation of experimental results, optimization and control of the process for better efficiency, and can be used to minimize the number of plant trials required in scaling-up or modifying the process.

Although many models are available for the many aspects of steelmaking, this study focuses on the composition changes of slag, metal phase and inclusions on the LMF process and particularly focuses on high manganese steel. Previously, several kinetic models had been proposed by researchers (Andersson, Hallberg, Jonsson, & Jönsson, 2002; Graham & Irons, 2008; Harada, Maruoka, Shibata,& Kitamura, 2013; Galindo et al., 2015) on the LMF process. Graham & Irons (2008) developed an LMF model to calculate the compositional changes of slag and steel based on the model developed by Robertson, Deo, & Ohguchi (1984). Additionally, the model was validated with several industrial heats at ArcelorMittal Dofasco for the refining of steel in a 165 ton LMF. Galindo et al. (2015) further developed the model (Graham & Irons, 2008) to include the transformation of alumina inclusions to magnesium aluminate spinel. This work showed excellent agreement with plant data in

predicting the timing of the changes in major inclusion type. The current work seeks to build on the work of Galindo et al. (2015).

2.6.1 Description of thermodynamic model for the steel system

The Wagner Interaction Parameter Formalism (WIPF) (Wagner, 1952) is the most common thermodynamic model used in metallurgy for the description of dilute solutions. In order to overcome the thermodynamic inconsistency of this classical formalism and obey the Gibbs–Duhem relationship in non-dilute solutions, Bale & Pelton (1990) introduced the Unified Interaction Parameter Formalism (UIPF) containing the correction term in the activity coefficient of a solvent.

The Unified Interaction Parameter Formalism (UIPF) (Pelton & Bale, 1986), was used to calculate the activity coefficients for dissolved elements in steel. High manganese steel is unexplored due to high alloy additions and the high manganese concentration , requires the Bale & Pelton (1990) approach. Additionally, Bale & Pelton (1990) mentioned that UIPF can be used in both dilute and non dilute regions, and that the thermodynamics are consistent at finite concentrations for multicomponent systems. This is a modification of the standard formalism (Wagner, 1962; Darken, 1967; Margules, 1895) that has been frequently used for dilute solutions. Pelton and Bale (1986) reviewed the shortcomings of Wagner's theory for higher solute concentrations, demonstrated the characteristics of UIPF, which include the following:

1. Is thermodynamically consistent at finite concentrations in binary, ternary, and multicomponent systems.

2. Can be derived from general Margules-type polynomial expressions (Margules, 1895).
3. Reduces to the standard first-order Wagner's interaction parameter formalism at infinite dilutions (Wagner, 1952).
4. Reduces to the standard second-order interaction, Lupis and Elliot parameter Formalism, at infinite dilutions (Lupis, 1983).
5. Reduces to the quadratic Darken's formalism, which is thermodynamically consistent at finite concentrations (Darken, 1967).
6. Can be employed with existing compilations of interaction parameters, or Gibbs energy expressions.

The modified activity coefficients for the solvent component in a solution are:

$$lnf_i = \sum_{j=1}^{N} \varepsilon_{ij} X_j + \sum_{j,k=1}^{N} \varepsilon_{ijk} X_j X_k + lnf_{Fe} \quad (2\text{-}15)$$

$$lnf_{Fe} = -\frac{1}{2}\sum_{j,k=1}^{N} \varepsilon_{ijk} X_j X_k - \frac{2}{3}\sum_{j,k,l=1}^{N} \varepsilon_{jkl} X_j X_k X_l \quad (2\text{-}16)$$

The parameters ε_{ij} and ε_{ijk}, of the UIPF, can be calculated from the reported first order ε_i^j, and second order ρ_i^{ij}, interaction parameters of Wagner's theory (Hino & Ito, 2010) the present model uses this approach.

Moreover, $\ln f_{Fe}$ is the correction term in UIPF, that is set to be zero in WIPF. The 1 wt % standard state with Fe, as a solvent, can be also used, but the validity of thermodynamic parameters (Henrian activity coefficients and interaction parameters) can be limited to Fe-rich solutions, rather than in a wide range of solutions. Paek, Chatterjee, Pak, & Jung (2016) highlight that WIPF has two inherent limitations. The first limitation

results from the assumption of ideal random entropy, regardless of the interactions between solvent and solute and between solutes themselves. In order to overcome this limitation, Jung, Kang, Decterov, & Pelton (2004) introduced the Associate model for deoxidation equilibria. The second limitation is that as the WIPF is originally designed for the description of dilute solutions, there is no interpolation technique integrated in the Gibbs energy formalism. When the model is applied to non-dilute solutions, there are always additional interaction terms required to correct the activity coefficients of solutes.

2.6.2 Kinetic model for the Slag-Steel reaction

To describe the kinetics of the multicomponent reactions between slag and metal, Robertson, Deo, & Ohguchi (1984) developed a mixed couple reaction model that could be used for dephosphorization and desulphurization, which also has applications in other processes. The work of Graham & Irons (2008), has demonstrated the coupled nature of the slag-steel reaction during the LMF process on the industrial scale. The model proposed by Robertson, Deo, & Ohguchi (1984), assumed that the rates are controlled by multicomponent transport in the metal and slag phases, considering thermodynamic equilibrium at the slag/metal interface. Their model assumes the charge balance of species and considers electro neutrality in the system. There exists a local equilibrium at the interface of respective elements and their oxides. The chemical kinetics of all the reactions were assumed to be fast. The actual driving forces used, were molar concentration differences for the oxides and sulphides between the bulk phases and the interface.

The model proposed by Robertson, Deo, & Ohguchi (1984) assumes that the reaction between the oxides in the slag and the respective species in the steel are:

$$x[M] + y[O] = (M_x O_y) \tag{2-17}$$

[ ] represents the species in steel, ( ) represents the compounds in slag. These types of reactions were considered in the work of Graham & Irons (2008) for FeO, CaO, MnO, SiO_2, MgO, TiO_2, and Al_2O_3 slag oxides. The equilibrium constant for all slag-steel reactions at the interface are:

$$K_{M-O} = \frac{(\gamma^*_{M_xO_y})(X^*_{M_xO_y})}{[f^*_M X^*_M][f^*_O X^*_O]} \tag{2-18}$$

where $f^*_M$and f^*_O are the Henrian activity coefficients for species in the steel determined for the composition at the interface, and $X^*_M, X^*_O, X^*_{M_xO_y}$ are the equilibrium molar fractions of the respective species at the slag-steel interface. Assuming that the kinetics are controlled by the transport of species from the bulk of the phase to the interface, the expression for the mass transport considering each reaction is:

$$k^M_m C_{v_m}\left(X^b_M - X^*_M\right) = k^{M_xO_y}_{sl} C_{v_{sl}} \left(X^*_{M_xO_y} - X^b_{M_xO_y}\right) \tag{2-19}$$

C_{v_m} and $C_{v_{sl}}$, are the total molar concentrations of the metal and slag phase respectively; k^M_m and $k^{M_xO_y}_{sl}$, are the mass transfer coefficients in the metal and slag respectively. By coupling all of the mass transport equations with the overall balance of oxygen and equilibria at the interface, the model generates a nonlinear system of equations that can be solved for the unknown interfacial concentrations.

$$k^O_m C_{v_m}\left(X^b_O - X^*_O\right) = \sum_{i=1}^{n} y_i k^{M_xO_y}_{sl} C_{v_{sl}} \left(X^*_{M_xO_y} - X^b_{M_xO_y}\right) \tag{2-20}$$

At each time step, the concentration of the bulk steel and slag are updated using the first order time integration equation for each species.

$$\frac{dX_{M_xO_y}}{dt} = -k_{sl}^{M_xO_y}\left(\frac{A}{V_{St}}\right)(X_{M_xO_y}^{b} - X_{M_xO_y}^{*}) \quad (2\text{-}21)$$

$$\frac{dX_{M}}{dt} = -k_{m}^{M}\left(\frac{A}{V_{St}}\right)(X_{M}^{b} - X_{M}^{*}) \quad (2\text{-}22)$$

Robertson (1995) suggested that the model could be used to describe several processes, such as the production of low carbon ferromanganese, desulphurization of pig iron, and the refining of stainless steel. Graham & Irons (2008) reported an empirical correlation for the mass transfer coefficient of [S], in the steel, for an industrial ladle. The exact form of this for the ArcelorMittal Dofasco ladle is:

$$k_m^S.A = 0.006 \pm 0.002\varepsilon^{1.4\pm0.002} \quad (2\text{-}23)$$

Where the effective stirring power ε [Watt/tonne] is calculated with Pluschkell's correlation (Pluschkell, 1981), as shown in equation (2-21). The mass transfer coefficients for all the species in the steel were assumed to be the same, while those for the species in the slag were expressed as ratio to the mass transfer coefficients in the metal, $k_m^M / k_{sl}^{M_xO_y}$,that were fitted to the data obtained from the plant. The suggested average slag phase mass transfer ratios for $k_m^{Fe}/k_{sl}^{\mathrm{FeO}}$, is 115; $k_m^{Mn}/k_{sl}^{\mathrm{MnO}}$is 7 ; $k_m^{Si}/k_{sl}^{\mathrm{SiO2}}$ is 125; and for $k_m^{Al}/k_{sl}^{\mathrm{Al2O3}}$, is 1. Graham & Irons, (2008) found that the coefficients vary depending on process conditions within the ladle, namely slag and steel compositions, stirring rate and electrical arcing. The kinetic model for desulphurization in the ladle is modeled considering mass balance from metal to slag:

$$k_m^S C_{v_m}\left(X_{S,m}^{b} - X_{S,m}^{*}\right) = k_{sl}^S C_{v_{sl}}\left(X_{S,sl}^{*} - X_{S,sl}^{b}\right) \quad (2\text{-}24)$$

The interfacial concentrations are related by means of an equilibrium partition coefficient for desulphurization, L_S'

$$L'_S = \frac{X^*_{S,sl}}{X^*_{S,m}} = C'_S . \frac{f^*_S . K_S}{[h^*_O]} \quad (2\text{-}25)$$

Where, C'_S is the slag sulphide capacity calculated with the empirical expressions proposed by Zhang, Chou, & Pal (2013), as the function of optical basicity in the slag, f^*_S is the interfacial activity coefficient for [S], K_S is the equilibrium constant of desulphurization reaction, and h^*_O is the interfacial activity of oxygen in the slag-metal interface. Figure (2-5), shows the flowchart of the numerical routine implemented for the multicomponent kinetic model (Graham & Irons, 2008).

Recently, a kinetic coupled model to describe industrial operations in the ladle furnace was proposed by Harada et al. (2013). This is a complex model that considers: 1) reactions between steel and slag, based on the multicomponent kinetic model (Robertson, Deo, & Ohguchi, 1984), 2) reactions between steel and inclusions originating from slag entrapment, 3) deoxidation caused by the additions, 4) dissolution of the refractory into the slag phase, and 5) formation, flotation and agglomeration of inclusions. Rates for slag entrapment, agglomeration of inclusions, and inclusions flotation are described using constant ratios. At each time step the composition of the different phases are updated. Figure (2-6) shows a schematic of the kinetic model proposed by Harada et al. (2013).

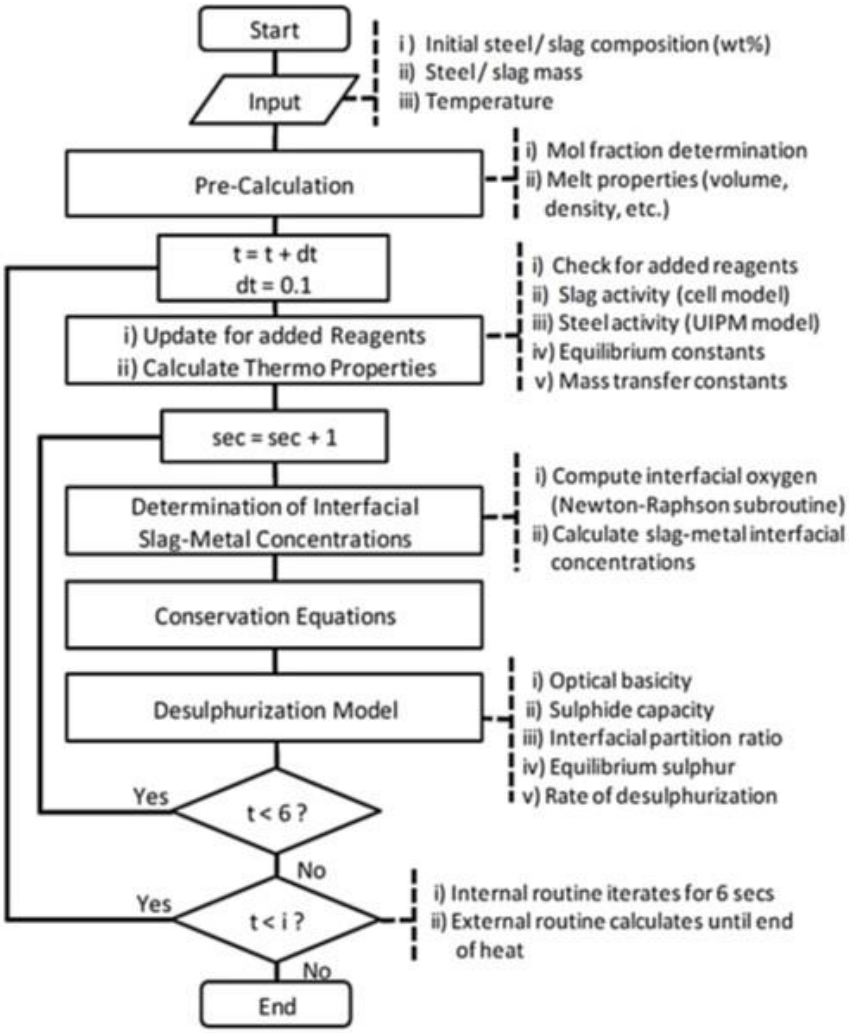

Figure 2-5: Flowchart of Multicomponent kinetic model (Graham & Irons, 2008)

Galindo et al. (2015) developed a kinetic model for the transformation of alumina inclusions to magnesium aluminate spinel inclusions. Compared to the previous kinetic model for slag-steel reactions (Graham & Irons, 2008), for Low Carbon Aluminum Killed (LCAK) process through LMF, it thoroughly describes the diffusion of magnesium in the solid inclusions during spinel formation. This model (Galindo et al., 2015) also takes into consideration the effects of reoxidation, caused by electrical arching, that takes place under different stirring conditions.

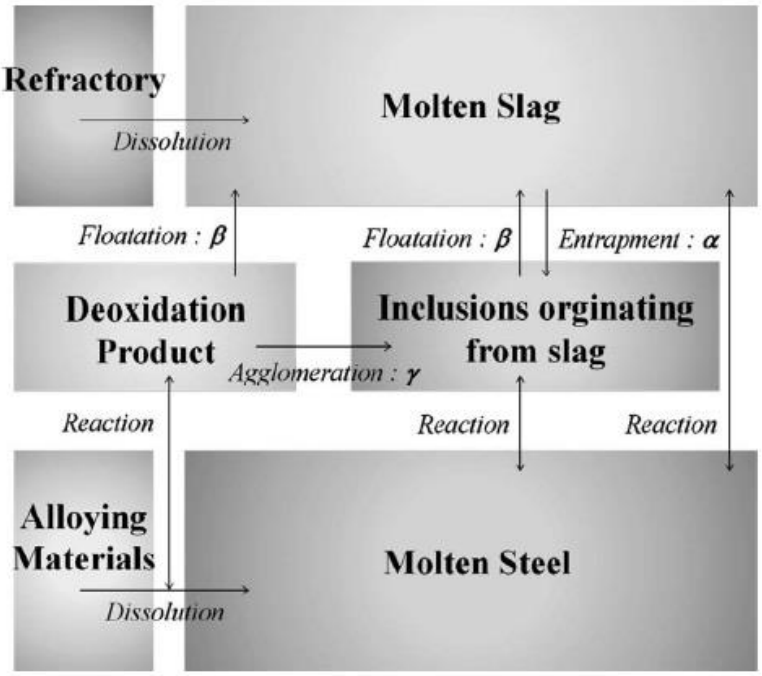

Figure 2-6: Schematic of the kinetic model proposed by Harada, et al.,(2013)

2.7 Non metallic inclusions in the high manganese steel

Non-metallic inclusions are an inevitable consequence of the steelmaking process, and foreign phases are always present in solid and liquid metal. Inclusions have different shapes and size, and may range from several microns to several hundred microns in diameter. They are randomly distributed in the matrix of the base metal and form a dispersion phase in both liquid and solid metallic phases (Kang et al., 2005).

Based on origin, inclusions are classified as exogenous or indigenous. Particles that come from external sources such as slag entrapment, erosion of refractories during processing of liquid steels are exogenous inclusions; indigenous inclusions are those that form during the reaction of the dissolved species in the liquid steel processing or during solidification of the steel (Ghosh, 2001).

Non-metallic inclusions are smaller in size and are hard to remove. They are easily carried by the flow of steel melt into the mold and adversely affect the steel's cleanliness and the clogging of nozzles while casting. The large inclusions can be disastrous, whereas the very small inclusions are unavoidable and are usually not dangerous. By composition, non-metallic inclusions are classified as oxides, sulphides, oxy-sulphides, nitrides, carbides and carbonitrides (Shannon & Sridhar, 2005).

Inclusions have remarkable influences on the properties of steels non–metallic inclusions may directly affect the properties of metals, leading to a deterioration of the mechanical properties and severe problems during steel processing. Reduction of the contents of non-metallic particles in the metal, avoiding windows or gaps to prevent the inclusion formation during the process, and the introduction of a modification process are significant methods for decreasing the unfavourable effects.

2.7.1 Background studies on classification of inclusions

Studies on inclusions and inclusion precipitation behaviour, in high Mn TWIP steel, have rarely been reported. Although the work of Gigacher et al. (2006) provided useful information on inclusions in high Mn steels, the effects of aluminum and manganese contents on the formation of oxides, nitrides, and sulfide compounds in high Mn-Al–alloyed steels were not explained. Park, Kim, & Min (2012) studied the effects of Al and Mn contents on the size, composition, and three-dimensional morphologies of inclusions in high Mn-Al–alloyed steels.

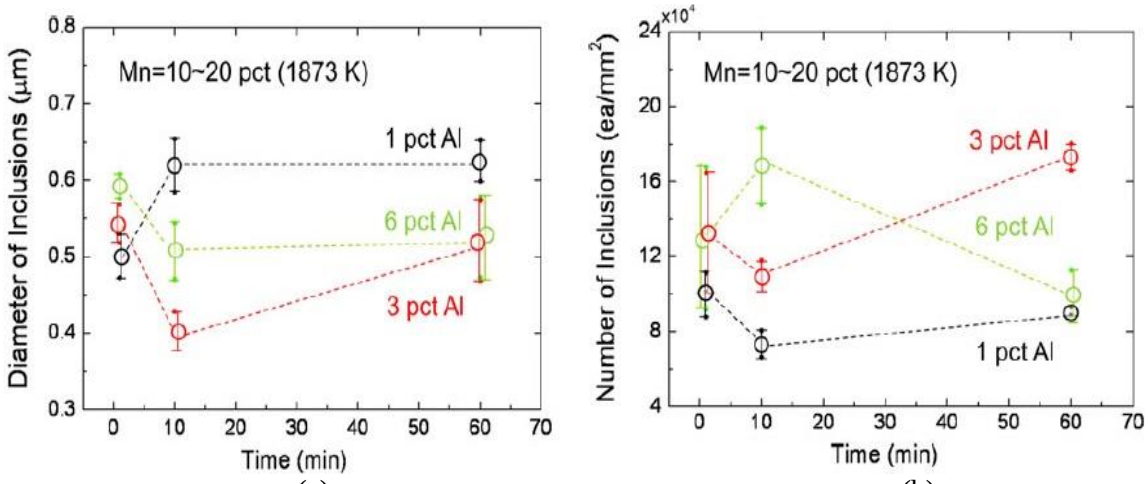

(a) (b)

Figure 2-7: Diameter (a) and number (b) of inclusions in Fe-Mn-Al–alloyed steels as a function of reaction time after the Al addition(Park et al, 2012)

Experiments were carried out for manganese contents at 10 and 20 wt% by melting the FeMn samples at 1873K, pure aluminum was added by varying the aluminum contents at 1, 3 and 6 wt%, under Ar- 3pct H_2 atmosphere. The system was equilibrated for 60 minutes, steel samples were collected at the 1, 5, 10, 30 and 60 minutes after the aluminum additions. The diameter and number of inclusions are studied as a function of time as shown in Figure (2-7). It was found that the size of the inclusions in Fe-Mn-1Al steels initially increases until reaching a constant value of 0.6 μm, which is mentioned in the figure below. However, in the Fe-Mn-3Al and Fe-Mn-6Al steels, the diameters of the inclusions decrease initially, followed by an increase and a plateau, respectively.

Inclusions in high manganese steel are classified, as shown in figure (2-8), according to chemistry and morphology (Park et al., 2012), and are categorized as the following types:

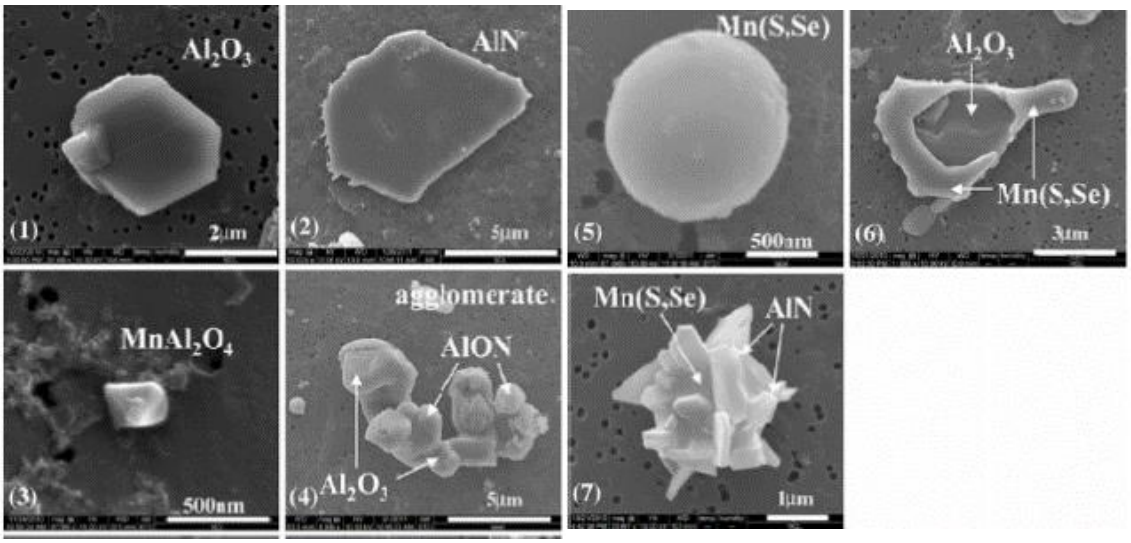

Figure 2-8: Morphologies of inclusions in high manganese content in steels. Type 1: Al_2O_3; type 2: single AlN or AlON particle; type 3: $MnAl_2O_4$ galaxite spinel particle; type 4: Al_2O_3(-Al(O)N); type 5: Mn(S,Se); type 6: oxide core with Mn(S,Se); and type 7: Mn(S,Se) core with Al_2O_3(-Al(O)N) aggregate)(Park et al.,2012)

(1) Al_2O_3; single alumina particle

(2) AlN or AlON; single aluminum nitride or oxynitride particle

(3) $MnAl_2O_4$; single galaxite spinel particle

(4) Al_2O_3(-Al(O)N) agglomerate

(5) Mn(S,Se); single manganese sulfur-selenide particle

(6) Oxide core with a Mn(S,Se) skin (wrap)

(7) Mn(S,Se) core with an Al_2O_3(-Al(O)N) aggregate

It was noted that the presence of complex Mn(S,Se) particles are found in the inclusions, caused by electrolytic manganese contamination with Se, which was used in their experiment (Park et al., 2012). As the manganese content increased, it resulted in an increase of selenium content in the steel. Work was carried out on a relative fraction of inclusions observed in EDS for in the Fe-10Mn-yAl and Fe-20Mn-yAl (y = 1, 3, and 6 mass

pct) steels, as a function of aluminum, with time during the processing at 1600°C.

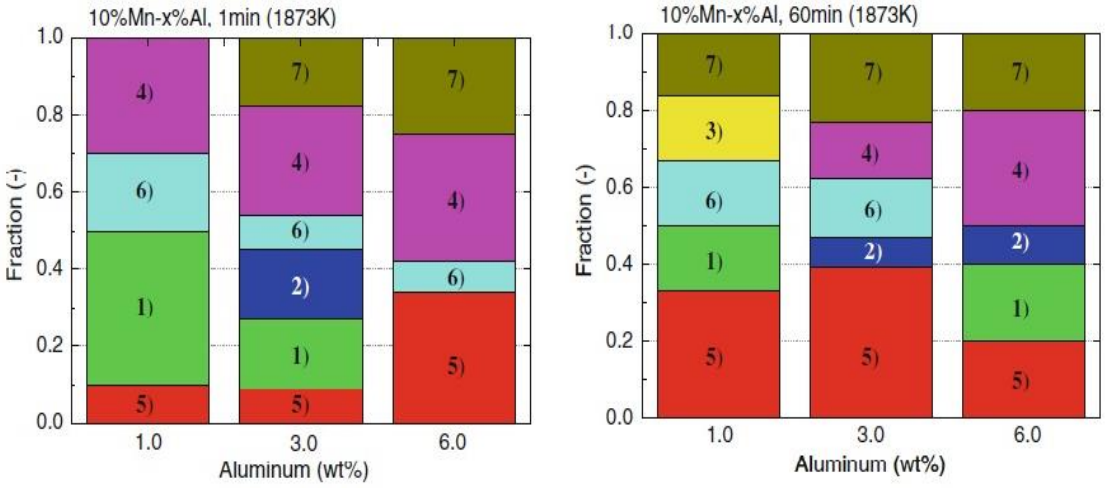

(a) ***(b)***

Figure 2-9: Relative fraction of inclusion in Fe-10Mn-xAl (y = 1, 3, and 6 mass pct) with respect to time of 1minute(a) and 60 minutes(b) Type 1 through 7 inclusions are defined in table 2-3(Park et al., 2012)

Table 2-3:Types of inclusions 1 through 7 are defined (Park et al., 2012)

Type	1	2	3	4	5	6	7
Inclusions	Al_2O_3	AlN/AlON	$MnAl_2O_4$	Al_2O_3(-AlON)	Mn(S,Se)	Oxide with Mn(S,Se)	Mn(S,Se) with Al_2O_3(-AlON)

Figure (2-9) shows the relative fraction of different inclusions for Fe-10Mn-xAl (y = 1, 3, and 6 mass pct), with respect to time of 1 minute and 60 minutes in the process. We can observe that single alumina (type 1) inclusions are dominant in the Fe-10Mn-1Al steel. However, alumina particles decrease with increasing time, mainly because of agglomeration and floatation to the melt surface. As the aluminum content increases, Al_2O_3(-Al(O)N) inclusions increase over the period of processing time.

The size of AlN aggregate is generally larger than AlON aggregate, which is observed in the SEM analysis. A qualitative explanation for the growth and sintering of AlON particles, which are controlled, possibly by low diffusion concentrations of oxygen and nitrogen. Moreover the nitrogen diffusion is more energetically favoured for growth and sintering of AlN, compared to AlON aggregates (Park et al., 2012).

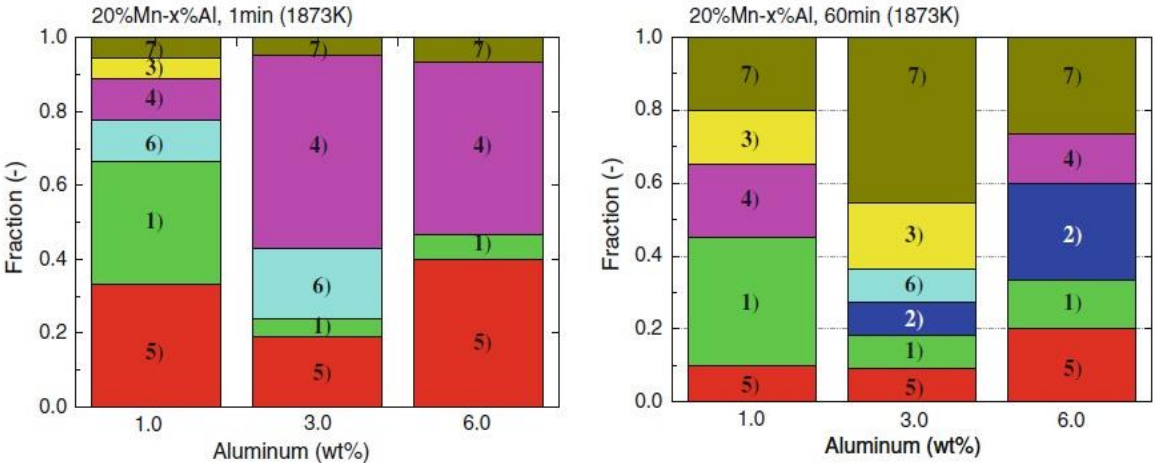

(a) (b)

Figure 2-10: Relative fraction of inclusion in Fe-20Mn-xAl (y = 1, 3, and 6 mass pct) with respect to time of 1 minute (a) and 60 minutes (b) (Park et al.,2012)

Table 2-4: Types of inclusions 1 through 7 are defined (Park et al., 2012)

Type	1	2	3	4	5	6	7
Inclusions	Al_2O_3	AlN/AlON	$MnAl_2O_4$	Al_2O_3(-Al(O)N)	Mn(S,Se)	Oxide with Mn(S,Se)	Mn(S,Se) with Al_2O_3(-Al(O)N)

Figure (2-9) shows the relative fraction of inclusions formed in Fe-20Mn-xAl (y = 1, 3, and 6 mass pct) as a function of aluminum with increasing time. It should be noted that the fraction of Mn (S,Se) inclusions increased profoundly with an increasing Mn content. From the microscopic examination, the Mn (S,Se) had formed and small AlN particles or large

AlN plates were attached and sintered to the surfaces of the Mn (S,Se) inclusions, with small amounts of Al_2O_3 inclusions present at the end of the 60 minute process. Although these workers reported relative fractions of inclusions, they did not report the total amount of inclusions present.

Recently, Wang et al. (2016) investigated the effects of the characteristics of inclusions in high manganese steel containing different aluminum contents of Fe-16Mn-xAl-0.6C (x = 0.002, 0.033, 0.54, 2.10 mass pct). These were analyzed using a SEM equipped with automated EDS. The chemical composition of the different grades of steel are shown in the table (2-5).

Table 2-5: Chemical composition in weight pct for different grades of TWIP steels (Wang et al., 2016)

Grade	C	Mn	P	S	Mg	Al	O	N
H000	0.58	16.41	0.007	0.0034	<0.0002	0.002	0.0015	0.0051
H003	0.68	16.01	0.008	0.0015	<0.0002	0.033	0.0008	0.0076
H054	0.65	16.30	0.008	0.0010	0.0002	0.54	<0.0005	0.0063
H210	0.58	17.07	0.007	<0.0005	0.0038	2.10	<0.0005	0.0043

Over 5000 inclusions were analyzed and classified in thirteen categories: (1)Al_2O_3; (2)AlN; (3)MgO; (4)MnO; (5)MnS; (6)$MgAl_2O_4$; (7)$MnAl_2O_4$; (8)Al_2O_3+MnS; (9)AlN+MgO; (10) MgO+MgS; (11) MnO+MnS; (12) $MgAl_2O_4$+MnS and (13) $MnAl_2O_4$+MnS. The fraction of inclusions, in percentages, formed in the TWIP steels are shown in figure (2-11).

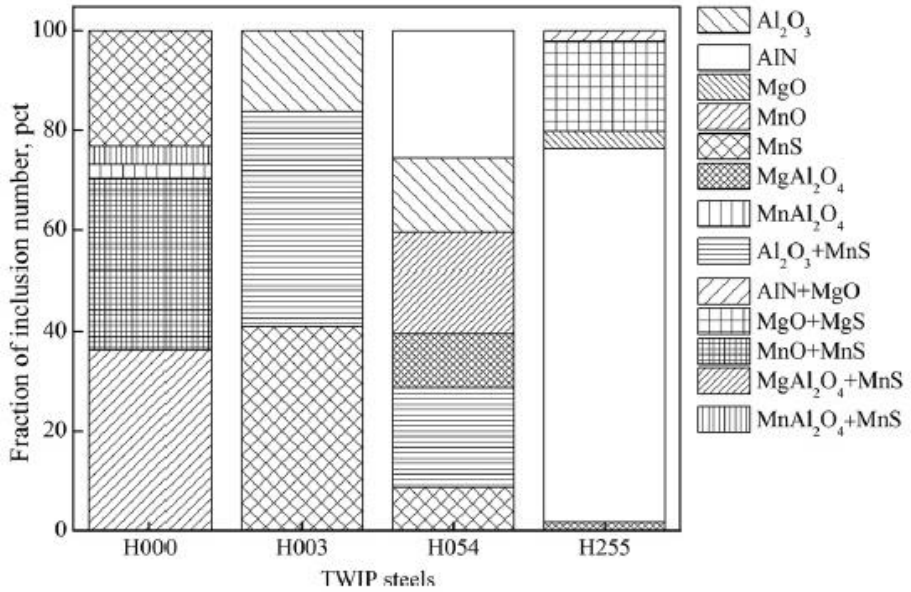

Figure 2-11: Fraction of inclusions number in pct for different grades of TWIP steels (Wang et al., 2016)

Main types of inclusions found in the above grades of chemical composition are:

H000 (Mn- 16.41wt%; Al- 0.002wt%) are MnS,MnO, MnS+MnO,$MnAl_2O_4$.

H003 (Mn- 16.01wt%; Al-0.033wt%) are MnS, Al_2O_3, MnS+Al_2O_3.

H054 (Mn- 16.30wt%; Al-0.54wt%) are AlN, MnS, Al_2O_3, $MgAl_2O_4$, Al_2O_3+MnS, $MgAl_2O_4$+MnS (The presence of Mg is a result of the reaction between the dissolved aluminum in the molten steel, with MgO in the crucible during experiment).

H210 (Mn- 17.07wt%; Al-2.10wt%) are AlN and MgO +MgS.

The average size of each inclusion in the TWIP steels, are shown in figure (2-12). The grades that have a high aluminum content, have sizes of inclusions that are less than 1 µm in the steel, for H054 and H210 for AlN and MgO+MgS respectively. It is seen that the average size of inclusions reduces with the addition of Al, where most of the inclusions are smaller than 4 µm. Moreover, some large inclusions have sizes greater than 4 µm in the

steel for Al of 0.002 wt%, such as $MnAl_2O_4$, $MnAl_2O_4$+MnS, and MnO+MnS.

The size of inclusions in the steel, range from 1 to 10 µm. Liu et al. (2016) observed that the dominant types of inclusions found in laboratory ingots and AOD processes, are AlN including single Al(O)N and MnS(Se)-Al(O)N, Al_2O_3, MnS. Inclusions found in samples for Fe–25Mn–3Si–3Al TWIP steels and their experiments, showed that after the ESR (Electro Slag Remelting) process, the amount of inclusions decreased (Zhuang et al., 2014; Liu et al., 2016).

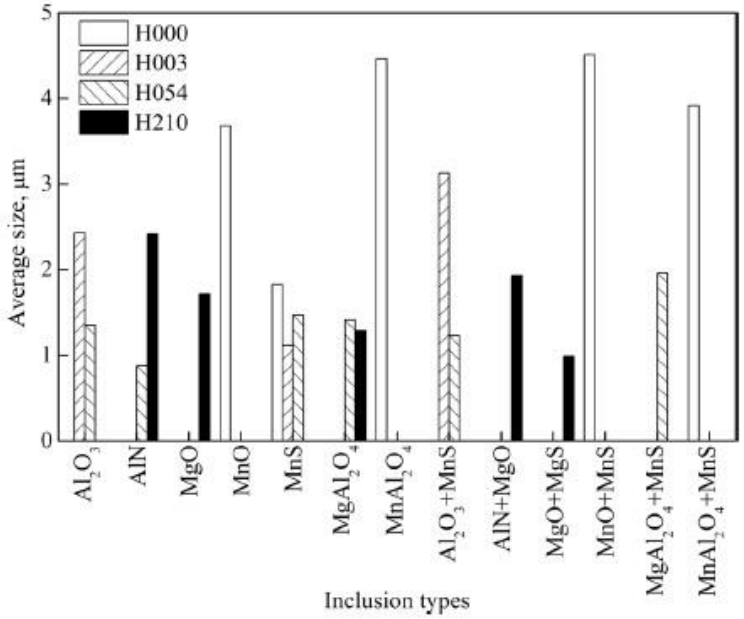

Figure 2-12: Average size of the types of inclusions in TWIP steels(Wang et al., 2016)

Wang et al. (2016) found that with an increase in the aluminum content from 0.002 wt% to 2.1 wt%, the main inclusions change along the route MnO/(MnO+MnS)→ MnS(Al_2O_3+MnS)→AlN/(Al_2O_3+MnS)/($MgAl_2O_4$+MnS)→AlN. Kang et al. (2011) found that the MnS inclusions appear to act as a nucleation sites for the precipitation of AlN on fracture surfaces. However, a study reveals that AlN particles, which appear on the fracture surface of the steel for 0.05 wt% of Al, are separate (Wang et

al., 2016).

Prior research (Park et al., 2012; Grajcar et al., 2012; Kang et al., 2011), found that the majority of inclusions in high manganese steel are MnS and AlN inclusions, coupled with Al_2O_3 inclusions. Work has been carried out in modelling Al_2O_3 inclusions across steel-slag interfaces (Shannon & Sridhar, 2005), which is not discussed in the present work. However, the presence of $MnAl_2O_4$ inclusions are observed (Park et al., 2012) with 1 wt% of Al, to better understand the formation of manganese spinel, the use thermodynamic software calculations was considered.

In order to better understand the observed inclusion types, a discussion of the thermodynamics of inclusion formation is presented below.

2.7.2 Analysis of Manganese Aluminate($MnAl_2O_4$) spinels

Efforts were carried out for the prediction of inclusions in high manganese steel using THERMOCALC, because of the availability of a separate database for high manganese steel. The database used for manganese spinel inclusions, TCFE7, is comprised of Fe-liquid, gas, AlN systems and Slag3, which includes data for slag and all of the inclusions. By varying the weight percentage of the aluminum, as a function of the manganese content, a stability map for inclusions in the Fe-Al-Mn-O system can be developed as a function of the initial oxygen content of the steel. The data retrieved from THERMOCALC for a high manganese system was plotted using MATLAB software. The typical oxygen content of metal from the BOF process was approximately 600 ppm (Cicutti et al., 2000). From figure (2-13), we could infer from the map the presence of $MnAl_2O_4$ spinels observed below 0.1 wt% of aluminum for a range of manganese contents, remaining

inclusions are mainly Al_2O_3 in the Fe-Mn-Al-O system.

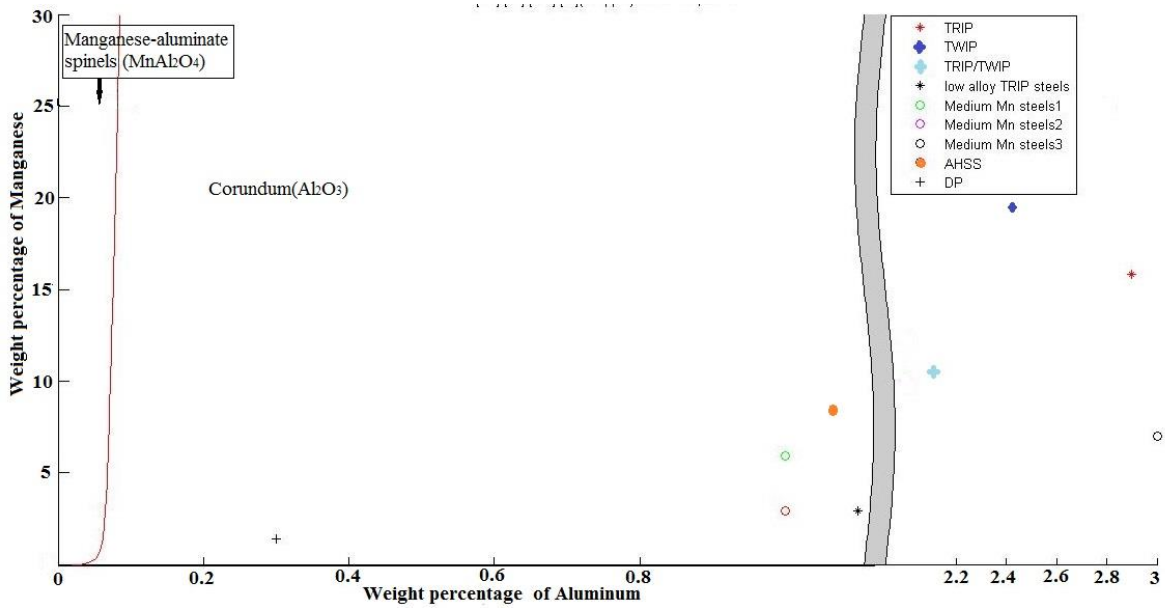

Figure 2-13: Inclusion map in Fe-Mn-Al-O system for 600ppm of Oxygen at 1600^oC using Thermocalc

Figure (2-14) shows a similar map for deoxidized steel with 10 ppm oxygen. From the plots on this map, we can see that $MnAl_2O_4$ spinels should not be formed. Al_2O_3 inclusions will exist for any steel with greater than 0.007 wt% of aluminum. The legends in the figures represent the manganese and aluminum contents for different types of steels, such as TWIP, TRIP, and AHSS. The figures of Fe-Al-Mn-O system are shown below for 600 ppm and 10 ppm of oxygen in steels.

Therefore, $MnAl_2O_4$ inclusions are likely to be insignificant for the expected range of Mn and Al content, under ladle metallurgy conditions. Recent literature (Wang et al., 2016) reports that for these steels, the majority of the inclusions found in samples are MnS, AlN and Al_2O_3.

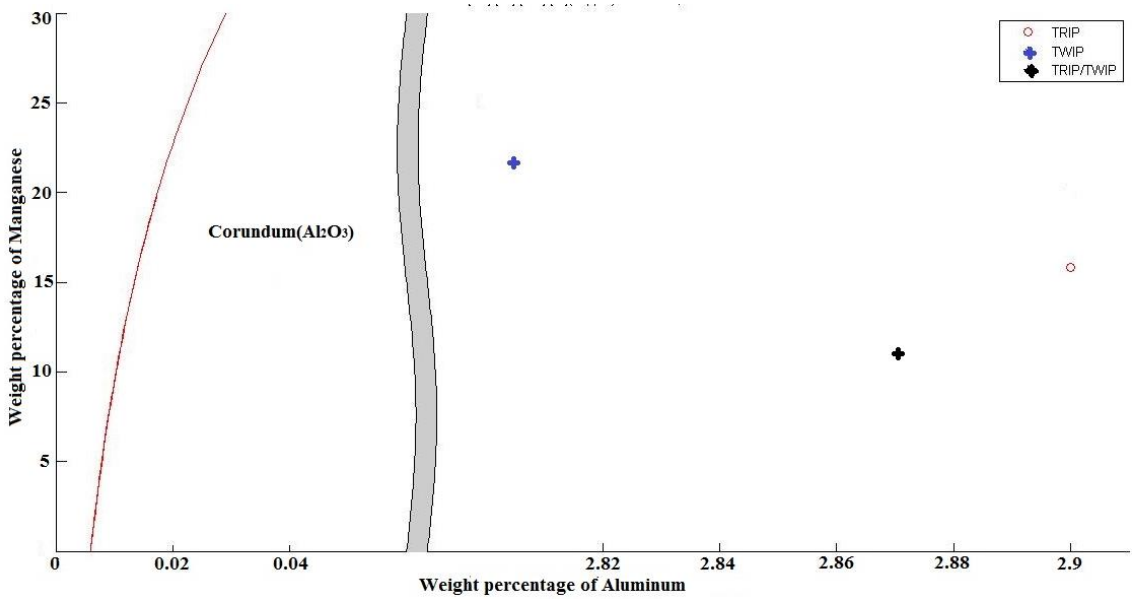

Figure 2-14: Inclusion map in Fe-Mn-Al-O system for 10ppm of Oxygen at 1600°C using Thermocalc

High-manganese steels contains Mn, Al and Si, with a high chemical affinity for oxygen, sulphur and nitrogen. Therefore, the presence of various sulphide and oxide inclusions should be expected. Manganese, silicon, and aluminum alloying additions present in high manganese steel are strong deoxidants, therefore limited dissolved oxygen will be present in molten steel. Manganese aluminate spinel inclusions are initially formed in the liquid metal at a high oxygen content, however no manganese aluminate spinel will be formed at low oxygen contents in the steel. Based on calculation, minimum oxygen content for the presence of manganese aluminate spinels in steel of 5wt% manganese is 20ppm.

2.8 Dominant inclusions in the high manganese steel

2.8.1 Aluminum Nitride(AlN) inclusions

2.8.1.1 Background information of Aluminum Nitride inclusions

Inclusions and steel cleanliness can greatly affect the casting process and the properties of the final products. Whilst the types of inclusions formed in conventional grades of steel are well known and well understood, the inclusions formed in newer grades, such as TWIP steels and third generation advanced high strength steel, requires study.

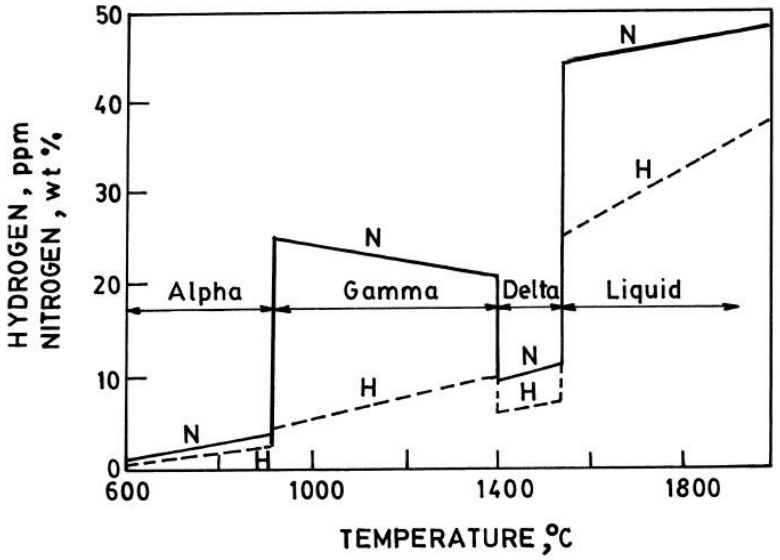

Figure 2-15: Solubility of H and N in pure iron at 1 atm (Ghosh, 2001)

Aluminum Nitride (AlN) is considered a detrimental phase for the hot ductility of steels (Vedani, Dellasega, & Mannuccii, 2009). Generally, gases such as hydrogen, nitrogen, and oxygen dissolve as atomic H, N, and O, respectively, in molten steel. However, their solubility in solid steel is very low. The solubility of hydrogen and nitrogen in pure iron, at 1 atm pressure of the respective gases, is shown in figure (2-15) (Ghosh, 2001). Nitrogen is picked up from the air during steel making, and affects the toughness and aging characteristics of steel, enhancing the tendency toward stress corrosion cracking.

Low nitrogen levels have become extremely important for ultra-low carbon, cold-rolled steels with a high formability for the automotive industry. However, it is worth mentioning that nitrogen has beneficial effects, such as grain refinement, and solid solution strengthening. Steelmakers endeavor to lower the extent of such pickup, while trying to flush out these gases from the melt using various strategies (Ghosh, 2001).

The majority of new AHSS grades feature a higher aluminum content, from 0.5% up to 2%, about 10 to 40 times higher than conventional aluminum-killed steels (Yin, 2006). Due to the high aluminum content, the type, size, and morphology of inclusions are expected to be different, which poses a major challenge in maintaining the steel's properties throughout the steelmaking and casting process.

2.8.1.2 Studies on precipitation of AlN inclusion

$$[Al]+[N] =(AlN)_s \quad (2\text{-}26)$$

Aluminum from the liquid metal and nitrogen gas, which is picked up from air, tends to precipitate AlN. Yin (2006) observed that for normal Al killed steels, at aluminum level of 0.04 wt%, slab transverse cracking occurred during straightening due to AlN precipitation. At a higher aluminum level of 1.2 wt%, more transverse cracking during casting would be expected, however transverse cracking has not been observed. Using the solubility product for AlN inclusions in austenite, equilibrium between aluminum and nitrogen at various temperatures is calculated using Thermocalc software, which is represented by equation (2-27).

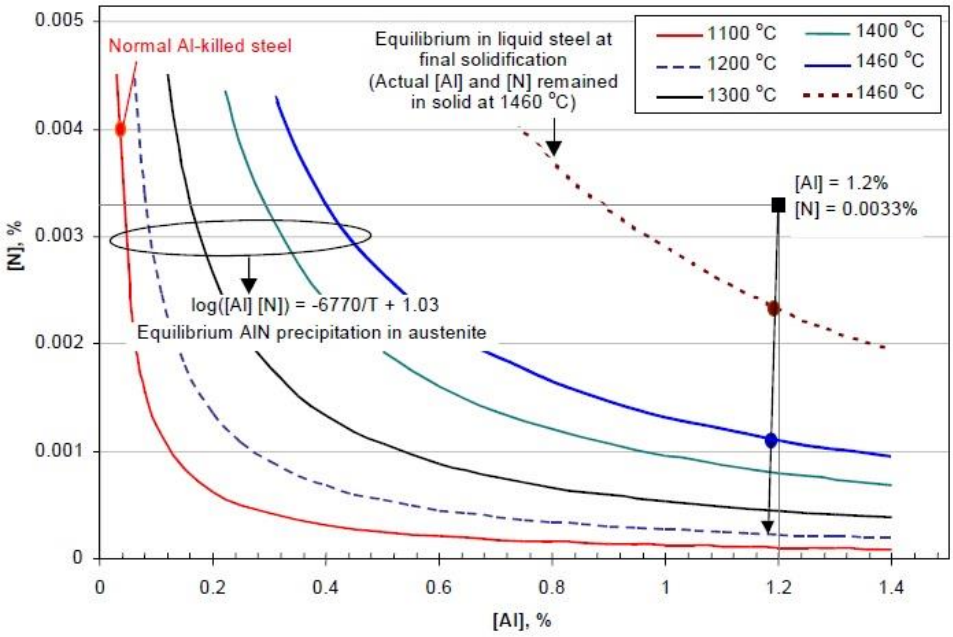

Figure 2-16: Thermodynamics of AlN precipitation (Yin, 2006)

$$Log[Al][N] = -6770/T+1.03 \quad (2\text{-}27)$$

From figure (2-16) of Fe-Al-N system, it becomes clear that, although the formation of AlN in liquid steel consumes some aluminum and nitrogen, the remaining [Al] and [N] is still far beyond the solubility limit of AlN when austenite appears (solid blue curve). This means that the driving force for AlN precipitation in solid austenite is huge, even at elevated temperatures. Therefore, AlN precipitation may be expected at higher temperatures than for lower Al steel. Hence, coarsening of early-precipitated AlN particles at high temperatures may dominate the consumption of aluminum and nitrogen during cooling, instead of a sudden explosion of huge amounts of tiny AlN precipitates below 1100°C, as seen in normal Al-killed steels. In support of this hypothesis, Yin (2006) found evidence of a much larger number of smaller AlN inclusions in the lower Al grade.

Kalisz and Rzadkosz (2013) mentioned that AlN inclusions are formed during the final stages of the solidification process for silicon steels. However, it has been found that the solubility of nitrogen in liquid iron decreased with the increasing aluminum content (Kim et al., 2007). Pure AlN was formed as critical aluminum and nitrogen contents in liquid iron. Moreover, Paek et al. (2013) suggested that AlN inclusions formed on the $MnO.Al_2O_3$ spinels, based on their research, and proposed first and second order interaction parameters, along with solubility limits for AlN formation. Figure (2-17) for Fe-Mn-Al-N system, shows the solubility limit of a percentage of nitrogen and aluminum in the steel, for different temperature ranges, for the Fe-20wt%Mn-Al-N melt system.

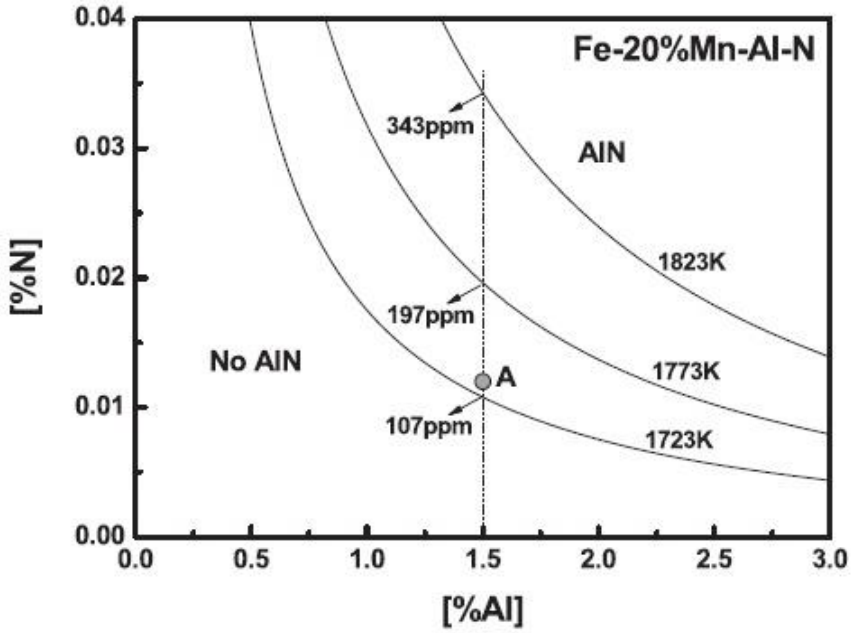

Figure 2-17: Solubility limit for AlN precipitation at different temperatures for the Fe-20wt%Mn-Al-N melt system (Paek et al. 2013)

Liu et al., (2015) studied the TWIP steels containing 0.05% carbon, 25% manganese, as well as 3% silicon, and 3% aluminum, and noted that the formation of AlN in liquid steel is theoretically possible at a certain levels of [Al], when [N] is in the range

of 30–70 ppm. Thermodynamic calculations by Liu et al. (2015) agree with previous findings (Yin, 2006; Paek et al., 2013) on AlN inclusion formation in liquid steel, demonstrating that the possibilities in Fe–Mn–Si–Al in TWIP steels, containing up to 3% aluminum, are expected to be different from regular Al-killed steels. Increasing manganese content, increases the maximum dissolved nitrogen content. A new first and second order interaction parameter for N in Mn, for up to 30wt%, were proposed (Liu et al., 2016) and parameters are also used in the present kinetic modelling for high manganese steel. Figure (2-18) (Liu et al., 2016) shows that the solubility limit of nitrogen increases , for high manganese and an increase in the aluminum content.

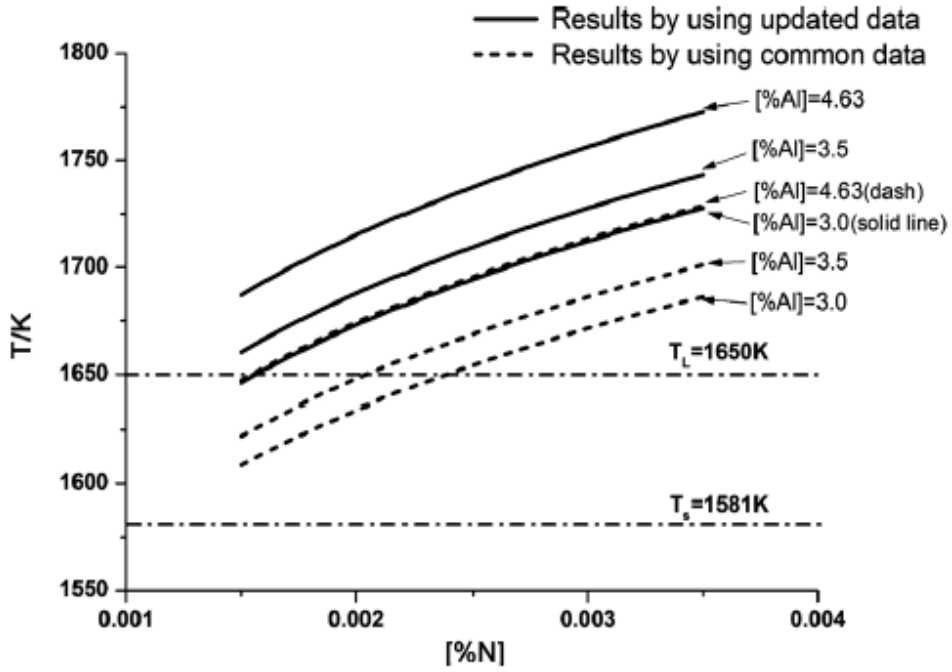

Figure 2-18: Solubility limit for nitrogen increases, for high manganese and increase in the aluminum content (Liu et al., 2016)

2.8.1.3 Thermodynamics of AlN inclusion precipitation

Paek et al. (2016), pointed out that there are considerable discrepancies in the Gibbs free energy of formation of AlN from previous studies. These authors considered the data, such as entropy of formation, and heat capacity of AlN from JANAF tables, but modified the enthalpy data based on experiments. The 'Present study' indicates the line proposed (Paek et al., 2016). Figure (2-19) shows the change in the Gibbs free energy for the formation of AlN and compared the author's work with previous research (Evans & Pehlke, 1964; Paek et al., 2013), which shows a good agreement with Paek et al., (2016).

However, the Gibbs free energy of AlN in the JANAF tables(Chase, 1998), was determined mainly based on the results of Hildenbrand & Hall (1963). Their results display a scatter in the data, along with several other researchers' work (Bolgar et al., 1968; Dreger, Dadape, & Margrave, 1962; Nakao, Fukuyama, & Nagata, 2002). Paek et al., (2016)

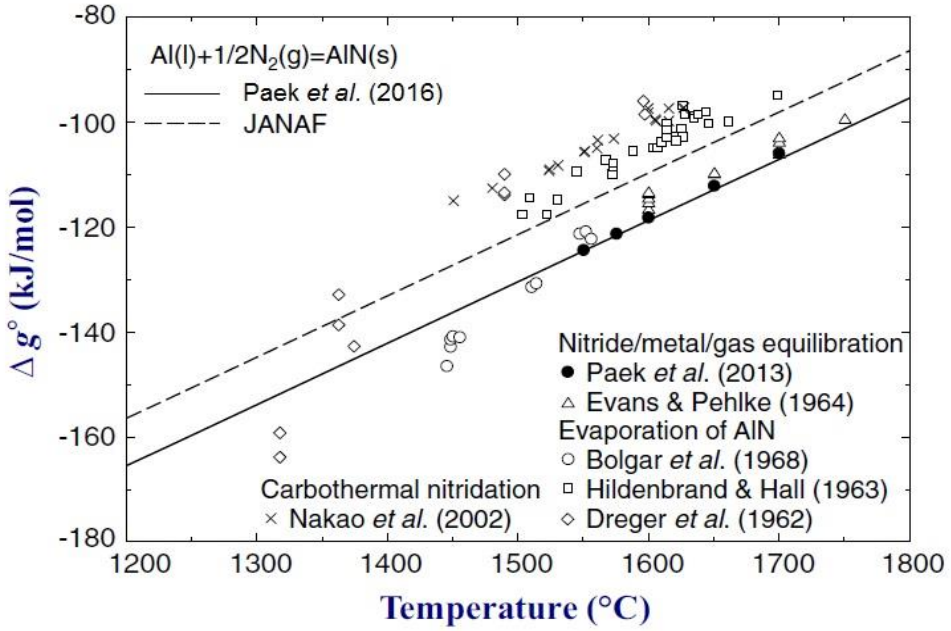

Figure 2-19: Standard Gibbs free energy of formation for AlN from liquid Al and N_2 gas(Paek et al., 2016)

proposed the Gibbs energy of nitrogen, for the Fe-Mn-Al-Si-C liquid solution, based on the evaluation of experimental data, but instead of using the classical Wagner interaction energy formalism, Paek et al., (2016) uses the Modified Quasichemical Model (MQM) for calculation, which results in good agreement with Paek et al., (2013) and with several other researchers. In the current research, we are using the Gibbs free energy data of AlN for dissolution (Paek et al., 2016).

$$[Al]+[N] = AlN_{(s)} \quad (2\text{-}28)$$

G^{o}_{AlN} =-316999.5+322.6T – 50.4T lnT +832748.2 T^{-1} -929.1$T^{0.5}$ -50107966 T^{-2} - 7862.0lnT (2-29)

2.8.2 Manganese Sulphide (MnS) inclusions

2.8.2.1 Source and origin of inclusions

The maximum S-content acceptable for high quality steel grades - such as Advanced High Strength Steels (AHSS) sheets, wheels, and tubes - has decreased over the years. It is therefore necessary to decrease the S-content during secondary steelmaking operations (i.e., during ladle refining, and before casting) in order to satisfy the ultra-low sulphur specifications. MnS inclusions affect the processing and properties of steel, and the effect may be influenced by many factors (Kalisz, Lelito, Szucki, Suchy, & Gracz, 2015). The most important factors include the sulphur content, the solidification rate, the degree of hot and cold deformation, and the hot working temperatures (Lehmann & Nadif, 2011).

2.8.2.2 Types of MnS inclusions

Oikawa et al. (1995) analyzed morphology control of primary and secondary MnS inclusions, during solidification of cast Fe-Mn-S steels. Different types of inclusions are

predicted based on the choice of stable or metastable phase diagrams. The morphology of MnS formed by primary crystallization, in sulfur-rich alloys, is classified under the first set of three types as: (i) spherical, (ii) dendritic, and (iii) angular. Meanwhile, the morphology of the secondary MnS formed in sulfur-lean alloys is classified under a different set of three types as: (i) monotectic, (ii) eutectic, and (iii) irregular eutectic. The occurrence of these morphologies is dependent on the nature of the oxides and nitrides that act as nuclei for the formation of MnS inclusions.

2.8.2.3 Studies on precipitation behavior of MnS inclusions

Wakoh, Sawai, & Mizoguchi (1996) studied the precipitation mechanism of MnS inclusions on oxide nuclei, by varying the S content in the steel. As the temperature decreases, and after the solidification of the steel, a small amount of MnS crystallizes on the surface of the oxide and acts as an embryo for MnS precipitation. The precipitation ratio of MnS on oxide particles, defined as the ratio of the number of oxide particles, acting as sites for MnS precipitation to the total number of oxide particles in steel. The MnS grows as a result of Mn and S diffusion in the steel. Based on experiments, the behaviour of MnS precipitation on oxide particles, in the case of 1 mass% Mn, was characterized according to S content as follows: (a) if sulphur is less than 0.002 mass%, the number of MnS particles precipitating on oxides was small, (b) for sulphur content between 0.002 to 0.01 mass percentage, the precipitation ratio was high for some oxides, that act as sites of MnS precipitation, (c) if sulphur was greater than 0.01 wt%, all oxide nuclei work as the precipitation sites for MnS.

Kim et al. (2000) observed MnS inclusion precipitates on MnO-SiO_2 inclusions in Si/Mn deoxidized steels, as shown in the figure (2-20). It is readily seen that of MnO-SiO_2 inclusions contains a small amount of sulfur, and MnS has precipitated out on it. The light area of the inclusion corresponds to the MnS phase, while the dark area is the MnO-SiO_2. They commented on the possibility of oxide and sulphide inclusions being precipitated as liquid phase (Kim et al., 2000). Studies also revealed a majority of MnS inclusion formations in oxide nuclei.

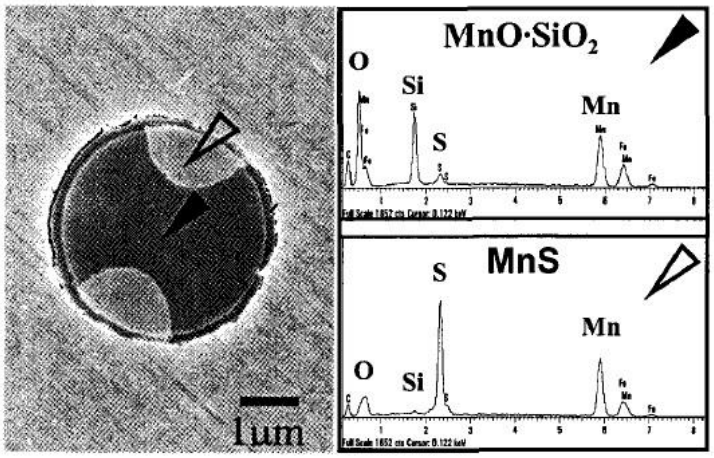

Figure 2-20: MnS precipitation on MnO-SiO_2 oxide inclusion. (Kim et al., 2000).

Figure (2-21) shows the solidus, where the MnO-SiO_2 is saturated with sulfur (Kim et al., 2001). Further decrease in the temperature facilitates the precipitation of MnS from the MnO-SiO_2 inclusion. The MnS precipitate grows, owing to the supply of Mn and S from the MnO-SiO_2 inclusion, as the solubility of Mn and S in the MnO-SiO_2 inclusion decreases during cooling. Based on this analysis, it is concluded that manganese silicate inclusions are initially in the liquid phase and solidify during cooling, and the center part of the inclusion is in solid state, whereas the outer part is in liquid phase.

Liu, Gu, & Cai (2002) proposed a mathematical model for the precipitation of oxide and sulfide inclusions, with microsegregation of solute elements Fe-Si alloys. A mechanism for the precipitation of sulfides on oxides was studied, in which liquid oxides in molten steel are treated as an oxide slag system (Liu et al., 2002). Optical basicity and sulfide capacity are introduced to calculate the equilibrium distribution ratio of sulfur between liquid oxides and molten steel during solidification. It is concluded that oxides with a low solidus temperature and high sulfide capacity of oxide inclusions, will encourage S dissolving in oxides and more sulfides precipitate on oxides.

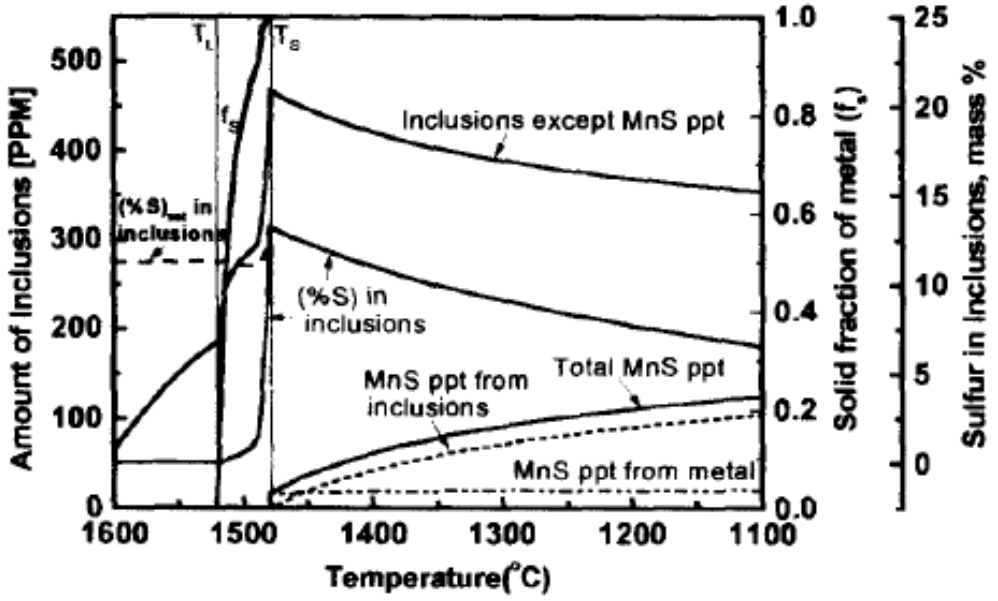

Figure 2-21: Precipitation behaviour of MnS inclusion during cooling (Kim et al.,2001)

Choudhary & Ghosh (2008) proposed that, while addition of Ca helps in modifying solid alumina inclusions into liquid calcium aluminate inclusions, the increasing sulphur content in steel transforms it into CaS or oxysulphide inclusions. Therefore steels require low sulphur contents, to obtain full modification of alumina into liquid calcium aluminate. The higher the concentration of Mn, the greater the concentration of MnS found in CaS–

MnS inclusions. This lowers the CaS activity, and further hinders the modification of oxide inclusions. However, the presence of Mn only has minor effects on inclusion modification during calcium treatment in most Al-killed steel. The sulfide inclusions are often a solid solution of CaS and MnS (Choudhary & Ghosh, 2008).

2.8.2.4 Thermodynamics of MnS inclusions

Woo, Kang, Gaye, & Lee, (2009) determined the eutectic temperature and composition for the MnO–MnS system to be 1256±3°C and 64±1 mass% MnS respectively. Moreover, the melting temperature of MnS, estimated by extrapolating the liquidus of MnS in the MnO–MnS binary system, was in agreement with previous findings (1655±5°C) (Staffansson, 1976). Several thermodynamic studies were carried out on the melting point of MnS (Ohtani, Oikawa, & Ishida, 2000; Oikawa et al., 1995). However, there was a discrepancy in the melting point of MnS ranging between 1530°C and 1655°C, (Kang, 2010) carried out a detailed analysis in predicting the melting point of MnS.

Kang (2010) carried out thermodynamic optimization by optimizing parameters of solid MnS, along with the liquid miscibility gaps in the Mn and MnS system. In that study, a value $S^{o}_{298\,K}$ (80.33 J/mol K) was chosen and $H^{o}_{298\,K}$ (-213.4 kJ/mol) was also adopted (Mills, 1974). Figure (2-22) shows the measured heat content data by Coughlin & Am (1950). This data was used by Mills (1974) to estimate the heat capacity of solid MnS. The data was also taken into consideration for the current study. The thick line in Figure(2-22) shows the calculated findings of Kang (2010), using the heat capacity function proposed

(Mills, 1974).

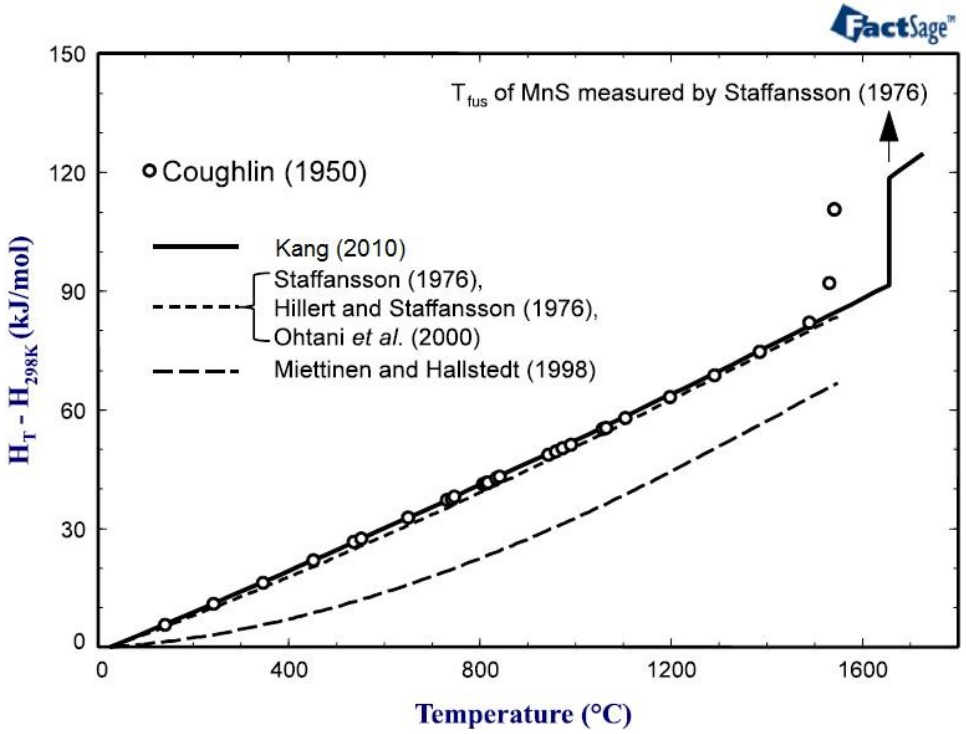

Figure 2-22: Heat content of measured MnS by drop calorimetry (Kang, 2010)

Below 1500°C, the agreement between Coughlin & Am (1950) data and the calculation in the Kang (2010) study is good. The long dashed line is the calculated heat content using parameters taken from Miettinen & Hallstedt (1998), while the short dashed line is the calculated heat content using the parameters Staffansson (1976) - subsequently adopted by Hillert & Staffansson (1976) and Ohtani et al., (2000). The latter three studies adopted an expression of Gibbs energy of formation for solid MnS. The enthalpy calculated by Kang (2010), which is indicated in the plot using Staffansson (1976), Hillert & Staffansson (1976), and Ohtani et al.,(2000) are shown to be in good agreement with the experimental data. The calculated heat content, from Miettinen & Hallstedt (1998) deviates from all the experimental data significantly.

3 Chapter

Thermodynamic and kinetics updates for high manganese steel

3.1 Inclusions in High manganese steel

Thermodynamics can be a useful tool for predicting the inclusion phase and composition of steel. The formation and evolution of inclusions are strongly dependent on concentrations of, even dilute, elements dissolved in the steel. Therefore, accurate thermodynamic data for both steel and inclusions are indispensable for the modelling of inclusions formation.

Kiessling (1980) carried out a study on the size distribution of oxide inclusions in a Si-killed steel ingot (with 100ppm oxygen). Figure (3-1) demonstrates the size distribution of inclusions. The total number of inclusions in this 6 ton ingot is about 3×10^{13}. It is observed that 98% of all inclusions are smaller than 0.2 μm, but these particles represent only 1-2% of the total oxygen content, as a result it will be impossible to remove all the oxide inclusions. Steel with only 1 ppm of oxygen and sulphur still contains 10^{10}-10^{12} inclusions per ton, with most of them being too small to resolve in the optical microscope. As the size of the inclusions decrease, the number of the inclusions per cm^3 increases. Regarding cleanness, the aim of different steelmaking methods, in addition to lowering the amount of inclusions, must therefore be to influence their size distribution, especially with an intent to avoid the largest ones, which are the most harmful in terms of physical properties.

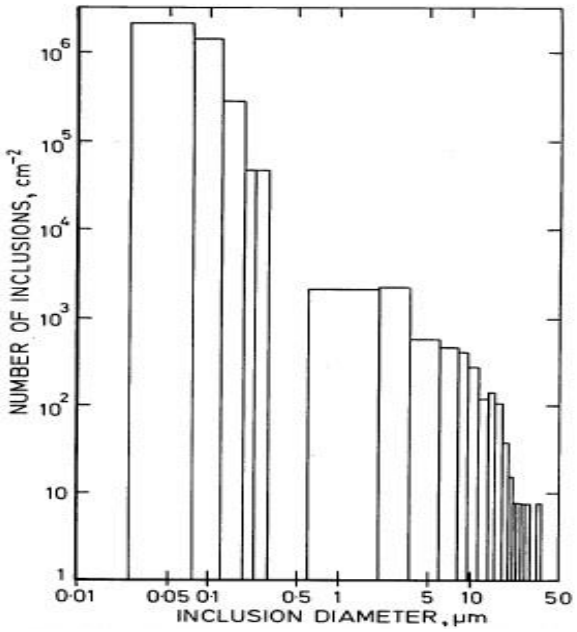

Figure 3-1: Size distribution of oxide inclusion in Si-killed steel ingot. The gap around 0.5µm is due to deficiencies in the observation (Kiessling, 1980)

3.2 Description of the Kinetic model for MnS and AlN inclusions

In this thesis, building on previous work on magnesium aluminate spinel formation(Galindo et al., 2015), a kinetic model is proposed for the growth of MnS and AlN inclusions in liquid steel. The model calculates the compositional changes in the inclusions, which has an influence on their diameter and on the liquid steel. To avoid the need for a nucleation step in the model, a number of pre-existing "seed" inclusions of each type are assumed to be present in the steel. These inclusions are sufficiently small to be of negligible impact on steel chemistry and the number is chosen based on plant data for the total number concentration of each inclusion type. The growth or shrinkage of the inclusions occurs in these preexisting seeds of MnS and AlN inclusions. The inclusion growth model is coupled with the slag-steel process model for ladle metallurgy.

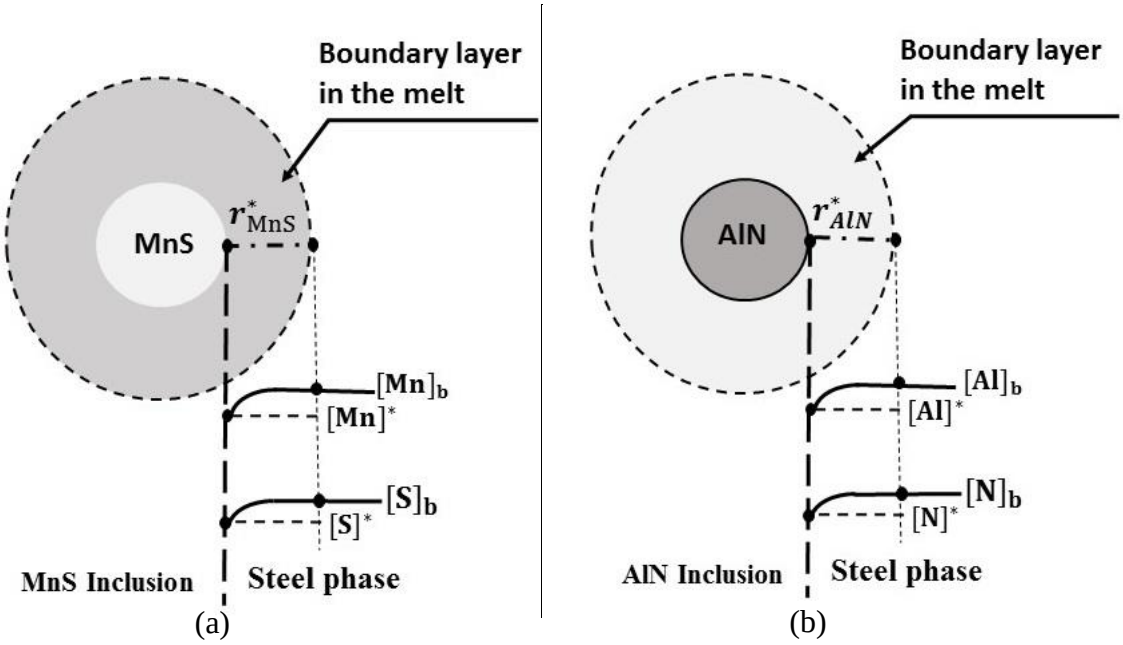

Figure 3-2: Schematic diagram of kinetic model for (a) MnS inclusion (b) AlN inclusion

3.2.1 Assumptions of the kinetic model for MnS and AlN inclusions

The kinetic steps, geometry and interface of the inclusion growth model are illustrated in Figure (3-2). The main assumptions of the model for both MnS and AlN inclusions are:

i. The kinetics of the process are mass transfer controlled.

ii. Local equilibrium exists between the elements at the inclusion-steel interface and inclusion. At the inclusion-steel interface, MnS and AlN, are in local thermodynamic equilibrium with the dissolved elements [Mn], [S] and [Al], [N].

iii. Spherical geometry for the MnS and AlN inclusions is assumed,

iv. Molar flux of [Mn] and [S] for the formation of MnS inclusions; [Al] and [N] for the formation of AlN inclusions are required to be equal to maintain stoichiometry.

The rate equations for each time step are solved considering thermodynamic and kinetic constraints.

3.2.2 Mass transfer of the species dissolved in the liquid steel

As mentioned by Szekely & Themelis (1971) and Oeters (1994), the diffusion boundary layer is a region adjacent to the interface, during mass transfer between a fluid and a solid or liquid phase, in which the concentration differs from that in the bulk of the fluid. This boundary layer is similar to the velocity and temperature boundary layers at interfaces for momentum and heat transfer. Szekely & Themelis (1971) suggested that basing mass transfer coefficients on knowledge of mass transfer rate between a solid and a fluid or between two fluids as more helpful than attempting to determine the concentration profiles. Well stirred fluids in movement offer negligible transport resistance within the bulk, concentration of species in the fluid is almost uniform and the only resistance to mass transfer exists in the boundary layer.

The equation for the mass transfer rate through the boundary layer from the bulk of the fluid to the spherical particle is

$$\mathrm{J_A} = \mathrm{k_A} 4\pi\, \mathrm{r}^{*2} \mathrm{C_V} \left(\mathrm{X_A^b} - \mathrm{X_A^*}\right) \tag{3-1}$$

Here, k_A is the mass transfer coefficient across the boundary layer in the melt, C_V is the molar density in the fluid phase, r^* is the particle radius, X_A^b is the molar fraction of the species A in the bulk of the fluid phase, and X_A^* is the molar fraction of the species A at the interface of the particle and boundary layer. The equation(3-1) only applies to the system involving either small concentrations of diffusing species or equimolar counter diffusion. The mass transfer coefficient, k_A, is associated with the geometry of the system, properties of the fluid and fluid flow conditions. k_A can be obtained from the Sherwood number (Sh), which is defined as:

$$Sh = \frac{k_A d}{D_A} \tag{3-2}$$

where, d is the diameter of the particle, and D_A is the diffusivity of the species in the fluid. Szekely & Themelis (1971) state that in the limiting case of a spherical particle in a motionless fluid, the Sherwood number at steady state conditions is equal to 2. Oeters (1994) explained that for liquid steel, if the particle diameter is smaller than 14 μm, calculation of the Sherwood number does not need to consider the flow of the melt and Sh = 2, which implies that at the boundary layer only mass transport by diffusion is possible, and that there is no convective contribution. Based on this argument, a Sherwood number of 2 can be adopted for all inclusion sizes relevant to the current study.

The mass transfer coefficients are calculated using the published diffusivities of the species in liquid iron, the values used are: $D_{[\mathrm{Mn}]} = 5.47\times 10^{-9} \mathrm{m}^2 \cdot \mathrm{s}^{-1}$ (Nagata, Ono, Ejima, & Yamamura, 1988), $D_{[\mathrm{S}]} = 4.3 \times 10^{-9}\ \mathrm{m}^2 \cdot \mathrm{s}^{-1}$ (Nagata et al., 1988), $D_{[Al]} = 3.5 \times 10^{-9} \mathrm{m}^2 \cdot \mathrm{s}^{-1}$ (Nagata et al., 1988) and $D_{[\mathrm{N}]} = 9.101\times 10^{-9}\ \mathrm{m}^2 \cdot \mathrm{s}^{-1}$ (Nagata et al., 1988) at 1600ºC. Therefore, the equations for the mass transfer rate through the boundary layer, for [Mn] and [S] diffusing from the bulk of the liquid steel phase, to the MnS inclusions surface are:

$$J_{[Mn]} = \mathrm{k_{Mn}} 4\pi\ \mathrm{r}^{*2} \mathrm{C_{Vm}} (\mathrm{X^b_{Mn}} - \mathrm{X^*_{Mn}}) \tag{3- 3}$$

$$J_{[S]} = \mathrm{k_S} 4\pi\ \mathrm{r}^{*2} \mathrm{C_{Vm}} (\mathrm{X^b_S} - \mathrm{X^*_s}) \tag{3- 4}$$

The equations for the mass transfer rate through the boundary layer, for [Al] and [N], diffusing from the bulk of the liquid steel phase to the AlN inclusions surface are:

$$J_{[Al]} = k_{Al} 4\pi\ r^{*2} C_{Vm} (X^b_{Al} - X^*_{Al}) \tag{3- 5}$$

$$J_{[N]} = k_N 4\pi\ r^{*2} C_{Vm} (X^b_N - X^*_N) \tag{3- 6}$$

where, X^{b}_{Mn}, X^{b}_{S}, X^{b}_{Al}, X^{b}_{N} are the bulk mole fractions in the steel phase; X^{*}_{Mn}, X^{*}_{s}, X^{*}_{Al}, X^{*}_{N} are the mole fraction at the interface between each inclusion and the steel; and C_{Vm} is the total molar concentration in the steel phase.

3.2.3 MnS inclusions kinetic model

3.2.3.1 Calculation of the MnS inclusion – steel interfacial equilibrium:

Taking MnS as an example, precipitation of inclusions, starts immediately after the product of Mn and S content in solution reaches the equilibrium solubility limit. Thermodynamic equilibrium, at the inclusion-steel interface, is calculated based on the equilibrium of [Mn] and [S] in steel with MnS. The calculation is possible by coupling the interfacial mass transfer rates of the components involved.

$$[Mn]+[S] = (MnS)_s \tag{3-7}$$

As discussed above, in the growth of MnS the fluxes of Mn and S must be equal according to the stoichiometry of the reaction.

$$k_{Mn}A\left(X^{b}_{Mn} - X^{*}_{Mn}\right) = k_S 4\pi\, r^{*2}\left(X^{b}_{S} - X^{*}_{S}\right) \tag{3-8}$$

From the reaction (3-7), K_{MnS} can be expressed as follows:

$$K_{MnS} = \frac{\alpha_{MnS(s)}}{h_{Mn}.h_S} = \frac{1}{f^{*}_{Mn}.[\%Mn].f^{*}_{S}.[\%S]} \tag{3-9}$$

Where $h_{[Mn]}$ and $h_{[S]}$ are the Henrian activities of manganese and sulphur relative to 1 mass% standard state in liquid iron, f_{Mn} and f_s are the activity coefficients of manganese and sulphur at the interface, respectively. From the Gibbs' free energy for the formation of MnS in liquid iron based on the standard state of infinitely dilute solution in liquid iron for manganese and sulphur, referred to hypothetical 1wt% solution, and on the

pure compound of MnS, where activity is 1. f_{Mn} and f_S can be calculated by the following equation:

$$lnf_i = \sum_{j=1}^{N} \varepsilon_{ij} X_j + \sum_{j,k=1}^{N} \varepsilon_{ijk} X_j X_k + lnf_{Fe} \quad (3\text{-}10)$$

Using Wagner's interaction parameter formalism, the first-order interaction parameter between manganese and sulphur, and the first-order and second-order self interaction parameter of manganese, lnf_{Fe}, were briefly described in the previous chapter. The equilibrium constant for the formation of pure solid MnS in liquid iron can be calculated:

$$log\ K_{MnS} = log \frac{1}{f_{Mn}[\%Mn] f_S[\%S]} = -log[\%Mn] - log[\%S] - logf_{Mn} - logf_S \quad (3\text{-}11)$$

where, parameters ε_{ij} and ε_{ijk} of the UIPF (Unified Interaction Parameter Formalism) can be calculated from e_i^j, and ρ_i^j, first-order and second-order interaction parameters, respectively, calculated using UIPF. For the calculation of equilibrium constant K_{MnS}, Gibbs' free energy for MnS (Kang, 2010; Mills, 1974) which is in raoultian reference state converted to henrian reference state was adopted in the present study:

G^o_{MnS} =-227 939.7765 + 241.3719T – 47.6976T lnT – 0.0037656T^2 (T < 1928)

From the equation (3-9), $$\frac{K_{MnS} \cdot f^*_{Mn} \cdot X^*_{Mn} \cdot (Mw_{Mn}) \cdot f^*_S \cdot X^*_S (Mw_S)}{\left(\frac{Mw_{Fe}}{100}\right)^2} = 1 \quad (3\text{-}12)$$

Here, Mw_{Fe}, Mw_{Mn} and Mw_S are the molecular weight percentages of Fe, Mn and S species, respectively; f^*_S and f^*_{Mn} are the Henrian activity coefficients calculated at the inclusion-steel interface; and K_{MnS} is the equilibrium constant of the MnS component.

From the equation (3-13), we obtain:

$$X_S^* = \frac{1}{\varepsilon * X_{Mn}^*} \tag{3-13}$$

Where, ε is assigned as:

$$\varepsilon = \frac{K_{MnS}.f_{Mn}^*.(Mw_{Mn}).f_S^*(Mw_S)}{\left(\frac{Mw_{Fe}}{100}\right)^2}$$

substituting (3-14) to the equation (3-9)

$$\left(X_{Mn}^b - X_{Mn}^*\right) = \frac{k_S}{k_{Mn}}\left(X_S^b - \frac{1}{\varepsilon * X_{Mn}^*}\right) \tag{3-14}$$

From the above equation

$$-\varepsilon\frac{k_{Mn}}{k_S}(X_{Mn}^*)^2 + \varepsilon\frac{X_{Mn}^*}{k_S}\left(X_{Mn}^b k_{Mn} - k_S X_S^b\right) + 1 = 0 \tag{3-15}$$

On solving the equation (3-15), the interfacial mole fractions of elements X_{Mn}^*, X_S^* can be obtained.

From the interfacial concentrations at inclusion-steel interfaces, we can calculate the flux of manganese and sulphur in the boundary layer.

$$J_{Mn} = k_{Mn}A(C_{Mn}^b - C_{Mn}^*) \tag{3-16}$$

$$J_S = k_S A(C_S^b - C_S^*) \tag{3-17}$$

Here, J_{Mn} and J_S are the flux of species in the boundary layer at the bulk and interface of the MnS inclusion; k_{Mn}, k_S are the mass transfer coefficients of the species, which are obtained from the equation (3-2); A is the surface area of the inclusion, C_{Vm} is the molar density in the metal phase.

$$J_{Mn} = k_{Mn}4\pi\, r^2 C_{Vm}(X_{Mn}^b - X_{Mn}^*) \tag{3-18}$$

$$J_S = k_S 4\pi\, r^2 C_{Vm}(X_S^b - X_S^*) \tag{3-19}$$

Where r is the radius of the MnS inclusion.

3.2.3.2 Calculation of change in the diameter for MnS inclusion:

Based on the change in the volume of inclusions, as shown in the equation (3-21), it is used to calculate the change the radius of the inclusions:

$$\frac{dV}{dt} = \frac{dV}{dn} * \frac{dn}{dt} \tag{3-20}$$

Here, dV is the change in volume with respect to time, dt; dn is the change in the number of moles; r is the radius of the MnS inclusion and Mw_{MnS} is the molecular weight of MnS inclusions.

$$V = \frac{Mass}{Density} = \frac{n * Mw_{MnS}}{\rho} \tag{3-21}$$

$$\frac{dV}{dn} = \frac{Mw_{MnS}}{\rho} \tag{3-22}$$

Similarly $\frac{\mathrm{dn}}{\mathrm{dt}} = \mathrm{J_{MnS}} = \mathrm{J_{Mn}} = \mathrm{J_S}$ (3-23)

Where V is the volume of inclusion, $V = \frac{4}{3}\pi r^3$ on differentiation $\frac{dV}{dr} = 4\pi r^2$, therefore

$$\frac{dV}{dt} = 4\pi r^2 \frac{dr}{dt} \tag{3-24}$$

Substituting (3-23),(3-24),(3-25) in (3-21)

$$4\pi r^2 \frac{dr}{dt} = \frac{Mw_{MnS}}{\rho} * J_{Mn} \tag{3-25}$$

$$\frac{dr}{dt} = \frac{Mw_{MnS}}{4\pi\rho} * k_{Mn} * C_{Vm} * \left(X^b_{Mn} - X^i_{Mn}\right) \tag{3-26}$$

Change of the manganese in the bulk due to the growth or shrinkage of the inclusions, can be calculated from the change of flux for a time interval with the number of MnS inclusion particles, which is given by:

$$\Delta N_{Mn,\ St-Inclusion} = \mathrm{J_{Mn}} * \text{number of MnS particles} * \mathrm{dt} \tag{3-27}$$

$$\Delta N_{S,\ St-Inclusion} = \mathrm{J_S} * \text{number of MnS particles} * \mathrm{dt} \quad (3\text{-}28)$$

The change in the number of moles of Mn, due to MnS inclusions, can be calculated from the change of flux for a time interval with a number of MnS inclusion particles. The concentration, in moles, of the dissolved species is updated for the next time step using first-order time integration:

$$[\mathrm{Mn}]_{t+1} = [\mathrm{Mn}]_t + \Delta[\mathrm{Mn}] \quad (3\text{-}29)$$

$$[\mathrm{S}]_{t+1} = [\mathrm{S}]_t + \Delta[\mathrm{S}] \quad (3\text{-}30)$$

With new concentrations in the steel, the thermodynamic equilibrium between inclusions and the steel is recalculated, which in turn provides the value of the boundary

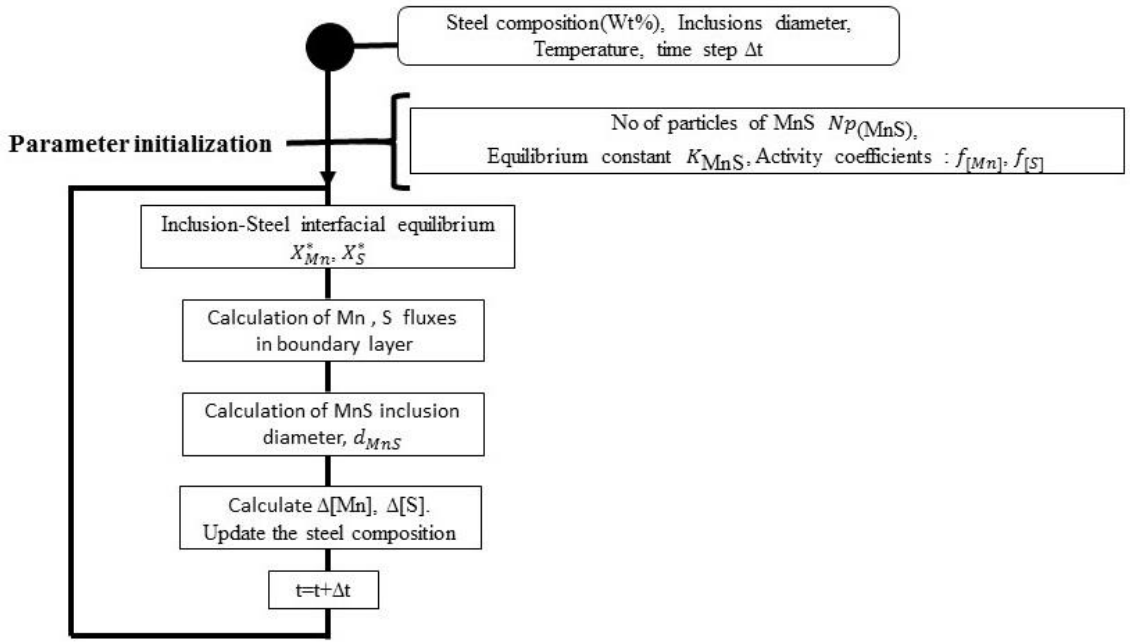

Figure 3-3: Scheme of time step procedure of the kinetic model for the growth/shrinkage of MnS inclusions

conditions for the time integration in the MnS inclusions. The stepping procedure for updating the concentration at each time step, is the basis of the kinetic model for the growth

or shrinkage of inclusions in the steel. A scheme of the algorithm is shown in Figure (3-3).

3.2.3.3 Results from the model for growth of MnS inclusion:

The performance of the kinetic model was evaluated in order to analyze the compositional changes in the steel and the MnS inclusions. For simplification of the system, the steel was assumed to contain only dissolved [Mn] and [S]. In these calculations, the mass of the steel was 160000 kg, the temperature was kept constant at 1843 K, the initial dissolved sulphur in the bulk of the steel was 650ppm, and the 10 weight percentage of manganese is considered, and the dissolved oxygen content is 5ppm.

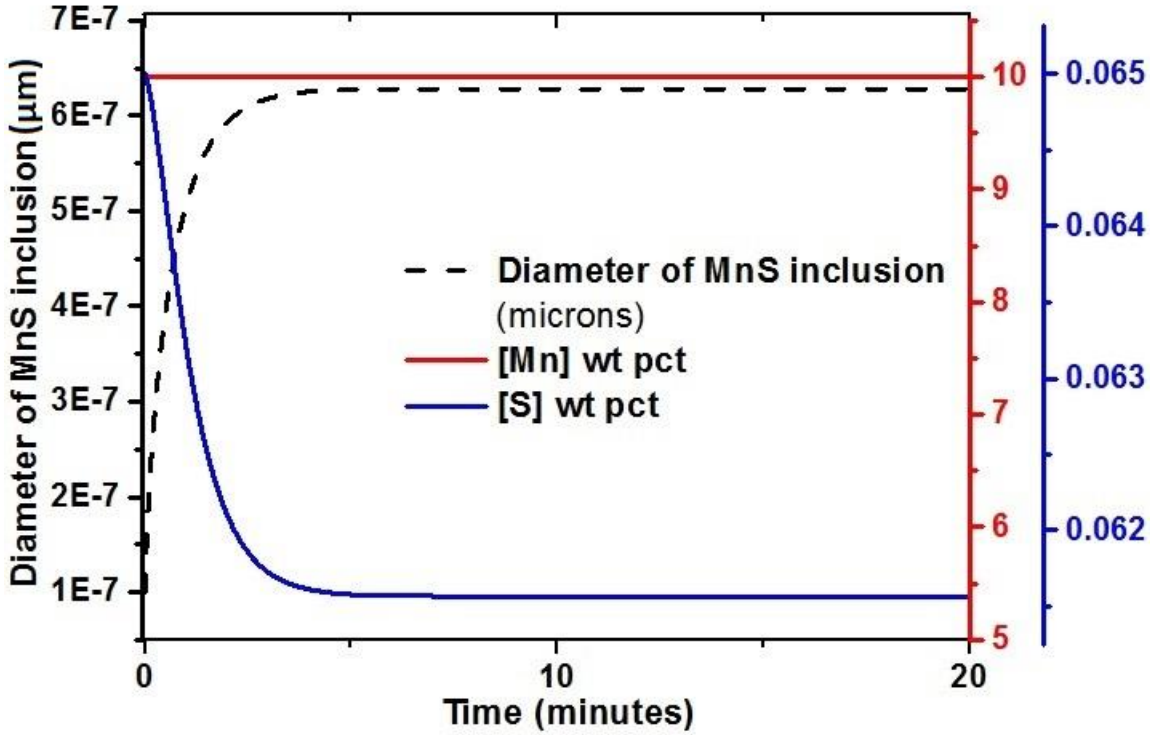

Figure 3-4:Calculated variation in the diameter of MnS inclusion respect to [Mn]and [S]wt%.

Finally, the total number of inclusions, Np, is assumed be 10^{10} particles per m^3, to start, of every modeled heat and was kept constant throughout the process. Initial MnS inclusions sizes are considered to be 0.1 micron in diameter. As discussed in the previous

chapter, MnS is a major inclusion in high manganese steel. Figure (3-4) shows the growth of the MnS inclusion diameter with a decrease in the [Mn] and [S] in the bulk steel.

The growth in diameters for MnS inclusions is shown, where the initial growth rate slows down with time and eventually reaches equilibrium with the [Mn] and [S] in the bulk steel after 5 minutes of the process. For the formation of MnS inclusions, [Mn] consumes the sulphur content in the bulk steel, until it reaches equilibrium.

3.2.4 AlN Inclusions in high manganese steel

It should be noted that high manganese contents significantly increase the solubility of N in liquid iron, while decreasing the melting temperature of the steels (Paek et al., 2013). In addition, aluminum nitride, AlN, can be easily formed. Paek et al., (2013) and Liu et al., (2015) pointed out that when the content of Al in high manganese steel increases, a lot of challenges arise during both the steelmaking and casting process. Although AlN inclusions are considered detrimental to surface quality and the mechanical properties of the final steel product, the critical N content for the AlN formation during ladle metallurgy, cooling and solidification is less predictable due to the lack of the thermodynamic information (Paek et al., 2016).

3.2.4.1 Calculation of the AlN inclusions – steel interfacial equilibrium:

As mentioned in the previous section, an argument can be made as to whether the observed large AlN particles were formed in liquid steel or precipitated in solid steel. Experimental work (Liu et al., 2016) on LCSM (Laser Scanning Confocal Microscope) further showed that AlN inclusions could precipitate in liquid TWIP steels. It is commonly accepted that, to form large particles and dendrites, a significant amount of thermodynamic

driving force is required.

$$[Al]+[N]=(AlN)_s \tag{3-31}$$

Thermodynamic equilibrium at the inclusion-steel interface is calculated based on the equilibrium of [Al] and [N] in the steel with AlN. Based on an equivalent set of assumptions to those made for the MnS inclusion formation in the section (3.2.3.1), we can derive a similar set of equations for calculating the equilibrium constant of AlN inclusions and flux of species in the boundary layer between the bulk and the interface of the AlN inclusions, which are represented as J_{Al} and J_N

$$J_{Al} = k_{Al} 4\pi r^2 C_{Vm} (X_{Al}^{b} - X_{Al}^{*}) \tag{3-32}$$

$$J_N = k_N 4\pi r^2 C_{Vm} (X_N^{b} - X_N^{*}) \tag{3-33}$$

The interfacial and bulk molar fraction of elements for aluminum X_{Al}^{*}, X_{Al}^{b} and nitrogen X_N^{*}, X_N^{b}, respectively, and r is the radius of AlN inclusions. For the calculation of the equilibrium constant K_{AlN}, gibbs free energy for AlN (Paek et al., 2016), in the Raoultian standard state, was adopted in the present study:

G_{AlN}^{o} =-316999.5+322.6T – 50.4T lnT +832748.2 T^{-1} -929.1$T^{0.5}$ -50107966 T^{-2} -7862.0lnT

3.2.4.2 Calculation of change in the diameter for AlN inclusion:

From Equation (3-26), which is similar to the MnS inclusion diameter calculation, we obtain:

$$4\pi r^2 \frac{dr}{dt} = \frac{Mw_{AlN}}{\rho} * J_{Al} \tag{3-34}$$

$$\frac{dr}{dt} = \frac{Mw_{AlN}}{4\pi\rho} * k_{Al} * C_{Vm} * \left(X_{Al}^{b} - X_{Al}^{i}\right) \tag{3-35}$$

Changes of the aluminum in the bulk, due to the growth or shrinkage of the

inclusions, can be calculated from the change of flux for a time interval with a number of AlN inclusion particles, which is given by:

$$\Delta N_{Al,\ St-Inclusion} = J_{Al} * \text{number of AlN particles} * dt \quad (3\text{-}36)$$

$$\Delta N_{N,\ St-Inclusion} = J_{N} * \text{number of AlN particles} * dt \quad (3\text{-}37)$$

A change in the number of moles of aluminum, due to the AlN inclusions, can be calculated from the change of flux for a time interval, with a number of AlN inclusion particles. The concentration of the dissolved species, is updated for the next time step using first-order time integration:

$$[Al]_{t+1} = [Al]_t + \Delta[Al] \quad (3\text{-}38)$$

$$[N]_{t+1} = [N]_t + \Delta[N] \quad (3\text{-}39)$$

With the new concentrations in the steel, the thermodynamic equilibrium between the inclusions and the steel is recalculated. This in turn provides the value of the boundary conditions for the time step of the mass transfer in the AlN inclusions. The stepping procedure for updating the concentration at each time step for AlN inclusions, is similar to the basis of the kinetic model for the growth or shrinkage of MnS inclusions in steel, as shown in figure (3-3).

3.2.4.3 Results from the kinetic model of AlN inclusions:

Kinetic model performance was evaluated in order to analyze the compositional changes in the steel and AlN inclusions. For simplification of the system, the steel composition was assumed to have the composition shown in table (3-1). In these calculations, the mass of the steel was 160000 kg, the temperature was kept constant at 1843 K, the initial dissolved nitrogen in the bulk of the steel was 60 ppm, and the 0.1 weight

percentage of aluminum is considered. The initial diameter of the inclusions was considered to be 0.1 microns. For a process time duration of 20 minutes, the diameter of AlN inclusions grows to 2.5 microns. Liu et al., (2016) and Wang et al.,(2016) observed that AlN inclusions comprise almost all of the inclusion particles in the liquid steel, at a size of about 2–5 μm. The LSCM (Laser Scanning Confocal Microscopy) experiment, further proved that AlN inclusions could precipitate in liquid TWIP steels. Additionally, work conducted on the Fe–25Mn–3Al–3Si TWIP steels (Zhuang et al., 2014), discovered a large number of AlN inclusions, of 5–15 μm, are found as dominant inclusions in TWIP steel. Figure (3-6) shows the growth of the inclusion diameter with a decrease of both [Al] and [N] in the bulk steel.

Table 3-1: Steel composition in weight percentage

Elements	**C**	**Mn**	**P**	**S**	**Si**	**Cu**	**Ni**	**Cr**	**Sn**	**Mo**	**Al**
Weight %	0.08	2	0.01	0.002	0.25	0	0.01	0.2	0	0.1	0.1

Elements	**N**	**Nb**	**Ca**	**B**	**Ti**	**Mg**	**O**	**Fe**
Weight %	0.006	0.0002	0	0	0.0006	0.00004	0.0005	Remaining

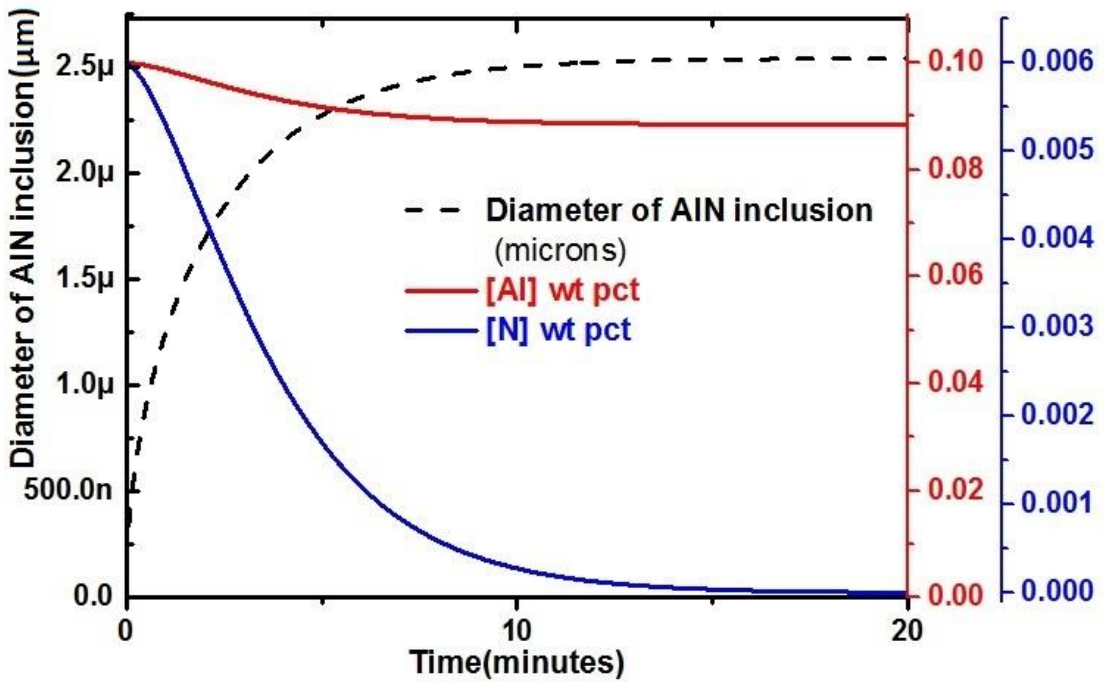

Figure 3-5: Calculated variation in the diameter of AlN inclusion with respect to[Al] and [N] weight percentage

The growth of the diameter for an AlN inclusion is shown, where the initial growth rate slows down with time and eventually reaches equilibrium with the [Al] and [N] in the bulk steel. For the formation of AlN inclusions, [Al] consumes the nitrogen content in the bulk steel until it reaches equilibrium. Np is the number of initial AlN particles of 10^{12}, which are taken into consideration from the bulk of the steel.

3.3 Kinetics and Thermodynamics for slag-steel system

Thermodynamic models, used in the study for liquid alloys and slags for production of steels, are coupled with the kinetic parameters that influence the slag/metal reactions in ladle refining. In this model, the kinetics of slag–steel reactions are based on the model of Robertson et al., (1984), which couples the oxidation-reduction reactions between the species dissolved in the steel and the respective oxide components in the slag. The slag-

steel reactions considered in the kinetic model of Graham & Irons, (2008) described that the compositional changes of the main components in the slag and steel, which include:

$$(FeO) = \{Fe\} + [O] \quad (3\text{-}40)$$

$$(CaO) = [Ca] + [O] \quad (3\text{-}41)$$

$$(MgO) = [Mg] + [O] \quad (3\text{-}42)$$

$$(SiO_2) = [Si] + 2[O] \quad (3\text{-}43)$$

$$(TiO_2) = [Ti] + 2[O] \quad (3\text{-}44)$$

$$(Al_2O_3) = 2[Al] + 3[O] \quad (3\text{-}45)$$

$$(MnO) = [Mn] + [O] \quad (3\text{-}46)$$

A schematic diagram of the mass transport process for the slag-steel reaction between (MnO), the [Mn] and [O] is shown in Figure (3-6). The driving force for mass transfer is the difference between the bulk concentrations, and the concentrations at the interface, where local thermodynamic equilibrium is assumed at the slag-steel interface.

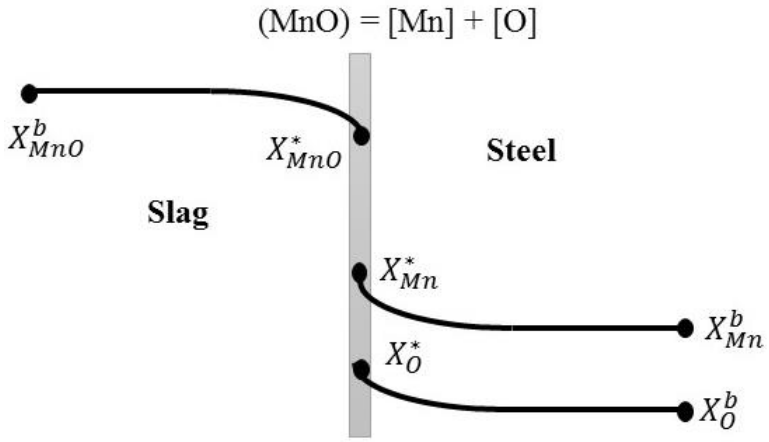

Figure 3-6: Mass transfer of the species from the bulk of the slag and steel phases

Our main objective is to develop and analyze a slag/metal model that provides robust tools, which can be used to understand the behavior of the elements and compounds

in the system during the processing for high manganese steel.

This thesis, considers the effects of inclusion growth in high manganese steel, coupled with the kinetics of slag metal reactions. This has required updates to the Graham & Irons (2008) model to include the kinetics of growth of MnS and AlN inclusions and an update, to the thermodynamics employed in the Graham & Irons (2008) model.

Kinetics of slag-steel reactions for low alloy steels are calculated with the kinetic model of Graham & Irons (2008) described in greater detail in the chapter two. Galindo et al., (2015), described the supply of [Mg] to the steel from the slag during ladle treatment for LCAK steels, along with additional features on the desulphurization and re-oxidation due to electrical arcing.

Understanding of the interaction between the steels is greatly aided by well-developed liquid oxide or slag models. There are a number of slag models that offer varied levels of success in representing the thermodynamics of liquid slags. For instance, the Cell model, the Generalized Central Atom (GCA) model (Lehmann & Zhang, 2010), Ionic model, the Modified Quasichemical Model (MQM) (Pelton & Chartrand, 2001; Pelton, Degterov, Eriksson, Robelin, & Dessureault, 2000), just to list a few.

In the current work, the cell model has been chosen to describe the slag system, because of the relative ease with which it can be embedded in the overall process model. The cell model, briefly described in the previous chapter, follows the approach proposed by Kapoor & Frohberg (1971) for binary and ternary systems, and was later extended to multicomponent systems (Gaye & Welfringer, 1984; Lehmann, Gaye, Yamada, & Matsumiya, 1990; Lehmann & Gaye, 1992).

3.3.1 Cell model Validation for binary systems in the slags

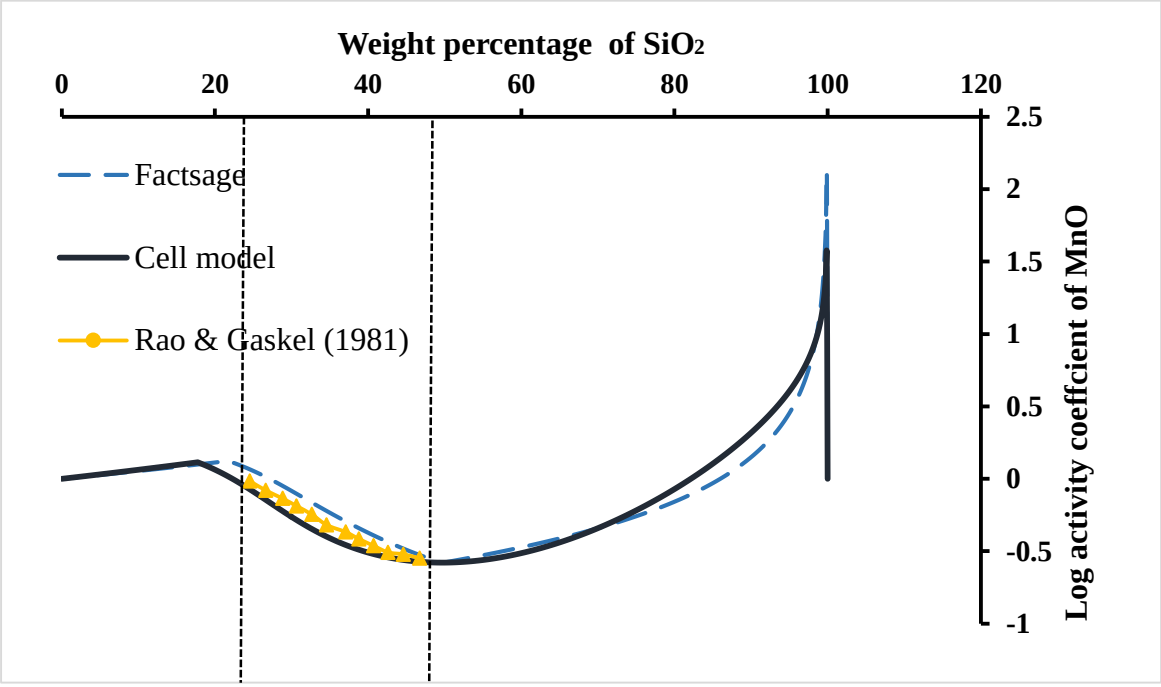

Figure 3-7: Comparison of Factsage, Cellmodel and experimental data SiO_2-MnO system,1500^oC (Rao & Gaskell, 1981)

Thermodynamic models for the SiO_2-MnO binary system, factsage and the cell model data are compared with experimental results (Rao & Gaskell, 1981) in Figure (3-7). Both models show excellent agreement with experimental data for the activity coefficient of MnO. Similarly, factsage agrees with the cell model results for the SiO_2-CaO system at 1500^{o}C, where the activity coefficient of CaO is plotted against the weight percentage of SiO_2 for the SiO_2-CaO system, as shown in the Figure (3-8). This displays agreement with experimental results (Carter & Macfarlane, 1957)(Sharma & Richardson, 1962) (Sawamura, 1962). However, in similar plots for the MnO-Al_2O_3 system the cell model, lacks agreement with the experimental data (Jacob, 1981) for the activities of MnO, which

are plotted against molefraction, as shown in the Figure (3-10).

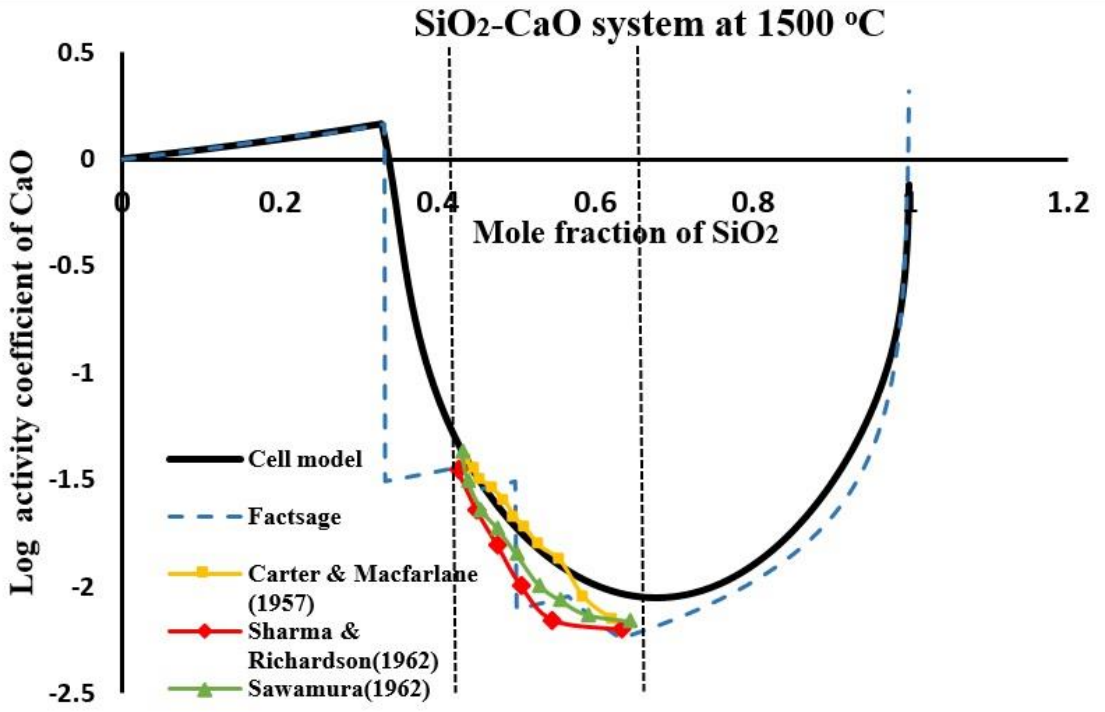

Figure 3-8: Comparison of Cellmodel, Factsage and experimental data for CaO-SiO_2 system at 1500°C.

Li, Morris & Robertson (1998) proposed interaction and formation energy values for the higher MnO content in the ferromanganese slags. However the values have not provided reasonable agreement with experimental data, therefore the formation and interaction energy values are unchanged in the model for W^1_{Mn-Ca} and E^1_{Mn-Ca} respectively.

When the binary system was extended to multi components, increase in the deviation of experimental data from the cell model was observed in the Al_2O_3 component of the slags. The activities of the components in the slag are calculated with the cell model, while for the species in steel, the Unified Interaction Parameter formalism is used.

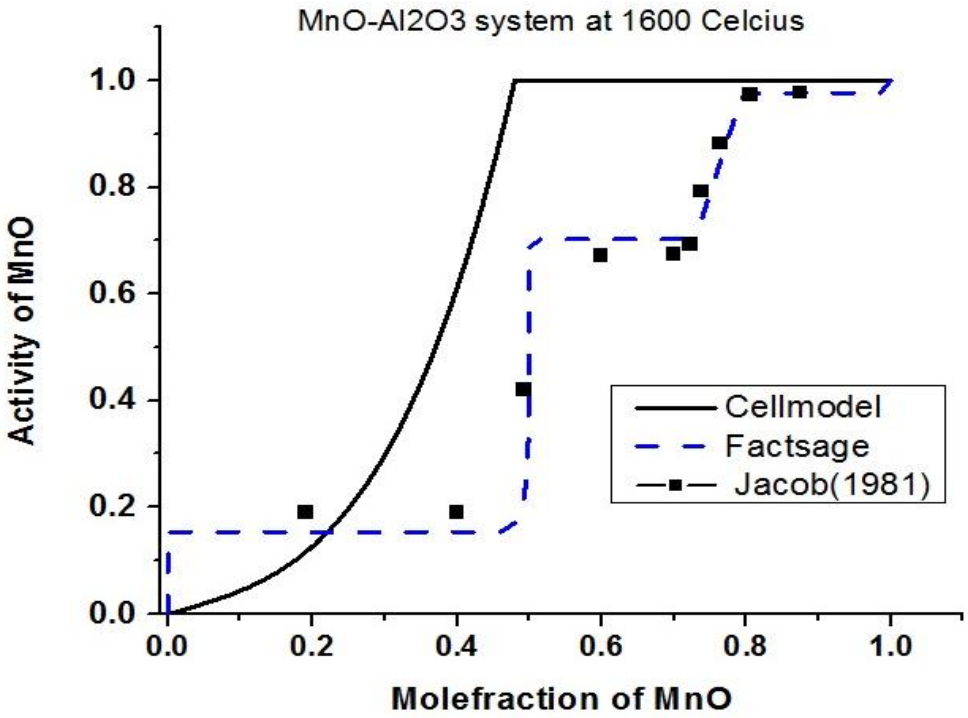

Figure 3-9: Comparison of Factsage, Cell model and experimental data (Jacob, 1981) for MnO-Al_2O_3 system, 1600°C

3.3.2 Thermodynamics updates for high manganese steel in slag-steel system

3.3.2.1 Updating interaction energy parameters & equilibrium constants in slag-steel system:

The thermodynamic data used to calculate the equilibrium with [Mn] and (MnO) were taken from previously published values (Takahashi & Hino, 2000), therefore, the equilibrium constant for the formation of MnO (K_{MnO}) is -11,900/T+5.10 at 1873K for <24Mn%. Based on Figure (3-12) and Figure (3-13), we can infer that the updated recommended equilibrium constant of MnO has a minor influence on the kinetic behavior of Mn wt% and MnO wt%, with time.

Moreover, the set of thermodynamic data used for calculating the activities of the liquid steel using UIPF (Unified Interaction-energy Parameter Formalism), have to be

evaluated for high manganese and high alloy steels. Here, the 1 wt % standard state with Fe as a solvent can be also used, but the validity of thermodynamic parameters (Henrian activity coefficients and interaction parameters) are limited to Fe-rich solutions, rather than in a wide range of solutions. Recommended first and second-order interaction parameters for the effect of other elements with manganese, taken from the review of the Japan Society for the Promotion of Science (Hino & Ito, 2010) are considered in the multicomponent kinetic model for slag-steel reactions,

The first and second-order interaction parameters, and their importance were briefly discussed in the previous chapter. Recommended first-order interaction parameters (ε_i^j) and second-order interaction parameters (ρ_i^j) (Hino & Ito, 2010) for high manganese steel, are shown in the Table (3-2). Figures (3-12),(3-13) and (3-14) shows the influence of recommended interaction parameters for high manganese steel.

Table 3-2: Updated First order and second order interaction parameters used in UIPF

i, j	(ε_i^j), (ρ_i^j)	i, j	(ε_i^j), (ρ_i^j)
C,C	0.14	***Si,O***	-0.25
C,Mn	-0.012	***Si,Si***	0.32
C,O	-0.34	***Si, Ti***	1.23
C,S	-0.046	***Al, Mn***	-0.004
Mn,Al	-0.012	***Al, N***	-0.004
Mn,C	0.004	***Al, Si***	0.060
Mn,Ca	-0.023	***N, Mn***	-0.02,-4.5e-5

Mn,Si	0	***N,O***	0.05
S, Al	0.035	***N,Si***	0.047
S, Ca	-2.87	***Ca,Ca***	-0.07
S, S	-0.028	***Ca,Mn***	-0.0156
Si,Al	0.063	***Ca,O***	-1.29
Si,C	0.18	***O,C***	-0.45
Si,Cr	-0.004	***O,Ca***	-0.14
Si, Mn	0	***O,Mn***	-0.037

3.3.2.2 Recommended update on desulphurisation model for high manganese steel

$$[\mathrm{S}] + \frac{1}{2}\mathrm{O}_2(\mathrm{g}) = [\mathrm{O}] + \frac{1}{2}\mathrm{S}_2(\mathrm{g}) \tag{3-47}$$

Desulfurization occurs as a reaction between steel, and top slag or slag droplets generated by inert gas stirring entrapped deep in the liquid bath (Lachmund et al., 2003). Therefore, the amount of slag and its composition, temperature, and the liquid bath stirring intensity, are important process parameters for steel desulfurization. For sulphur, the equilibrium partition coefficient, L_S', for desulphurization with slag is calculated using:

$$L_S' = \frac{C_S' \cdot f_S^* \cdot K_S}{[h_O^*]} \tag{3-48}$$

In expression (3-48), h_O^* is the activity of dissolved [O] in steel at the slag-steel interface, that satisfies the multicomponent thermodynamic equilibrium of all the reactions. K_S is the equilibrium constant for desulphurization with the top slag, f_S^* is the activity coefficient of the dissolved [S] at the slag-steel interface, and $C_S^{'}$ is the modified sulphide capacity calculated by empirical correlation, as a function of optical basicity of the slag.

The precision of the sulphide capacity depends on the activity calculations. Young et al., (1992) modified and proposed a model to calculate the sulphide capacity of slag, using the optical basicity (Sosinsky et al., 1986) concept. In the kinetic model for the LMF, Graham & Irons (2008) used the model proposed by Young et al., (1992) to calculate sulphide capacity. The Young et al., (1992) model employs represented in Equations(3-50) and (3-51).

The optical basicity (Λ) value for a given slag composition can be calculated using

$$\Lambda = X_1\Lambda_1 + X_2\Lambda_2 + \cdots + X_i\Lambda_i \tag{3-49}$$

Where, X_i is the equivalent fraction of component oxides, and Λ_i is the optical basicity values of the respective components. The optical basicity values based on Young et al., (1992) data are shown in the table (3-3)

Table 3-3: Optical basicity values of Young et al., (1992)

Components	**CaO**	**MgO**	**Al_2O_3**	**SrO**	**FeO**	**MnO**	**ZnO**	**Cr_2O_3**	**Fe_2O_3**	**BeO**
Optical basicity	1.00	0.78	0.60	1.10	1.00	0.98	0.95	0.70	0.77	1.15

$$\log C_S = -13.913 + 42.84\Lambda - 23.82\Lambda^2 - \left(\frac{11710}{T}\right) - 0.02223(wt\%SiO_2) - 0.02275(wt\%Al_2O_3) \qquad \Lambda < 0.8 \tag{3-50}$$

$$\log C_S = -0.6261 + 0.4808\Lambda - 0.7197\Lambda^2 - \left(\frac{1697}{T}\right) - \left(\frac{2587\,\Lambda}{T}\right) + 0.0005144(wt\%FeO) \qquad \Lambda \geq 0.8 \tag{3-51}$$

However, the accuracy of the Young et al., (1992) model is low. Nzotta et al. (1999) suggested an optimized model, developed at KTH, for predicting the sulphide capacities. This model was used to predict the sulphide capacities of some of the typical BF, EAF and LF slags. These workers considered all of the complex polymeric ions as a dissociated species, and reported that the optical basicity model (Young et al., 1992) over-predicts L_S compared to their model (Nzotta et al., 1999). Many parameters are required for optimized calculations, using the KTH model and it uses complex interaction parameters for binary, ternary and multicomponent systems. Since a large number of parameters are required for calculating the sulphide capacity, Zhang et al., (2013) modified the optical basicity values for four major elements and proposed a new sulphide capacity expression based on the previous model (Young et al., 1992).

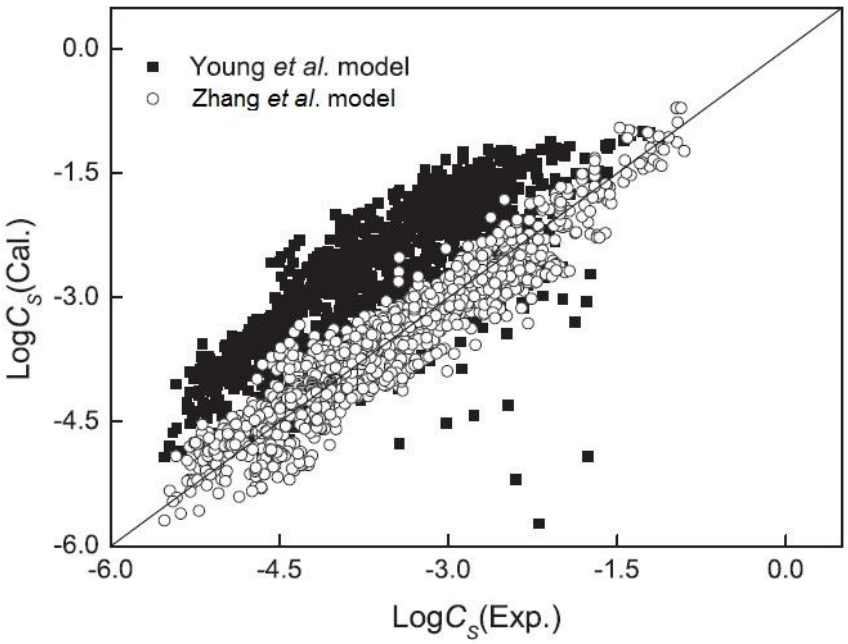

Figure 3-10: Comparison of sulphide capacities using Young et al. model (1992) and Zhang, Chou, and Pal model (2013).

Figure (3-10), compares the calculated sulphide capacities of Young et al., (1992)

indicated, alongside the alternative model of Zhang et al., (2013). Experimental data is compared with the calculated values of both models. The model proposed by Young et al., (1992) showed a significant deviation from the calculated values of Zhang et al., (2013) for the CaO-MgO-FeO-MnO-TiO_2-Al_2O_3-SiO_2-CaF slag system.

Figure (3-11) compares the calculated sulphide capacities, indicated as the "KTH model" (Nzotta et al., 1999) and the calculated sulphide capacities of Zhang et al., (2013), which shows reasonable agreement with the experimental data for the slag systems compared to the KTH model (Nzotta et al., 1999).

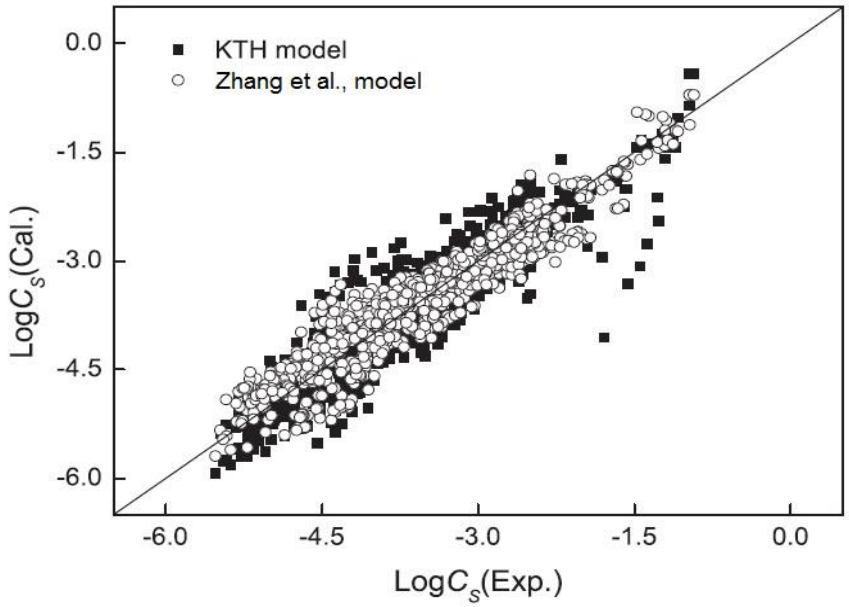

Figure 3-11: Comparison of the sulphide capacity data of Zhang et al., (2013) and the KTH model (Nzotta et al., 1999)

Optical basicity values are modified in the model of Zhang et al., (2013), and are indicated as " * " in Table (3-4), and the new sulphide capacity expression is shown in the equation (3-52).

Table 3-4: Zhang et al., (2013) model's updated optical basicity values

Components	**CaO**	**MgO**	**Al_2O_3**	**SiO_2***	**FeO***	**MnO***	**TiO_2***	**CaF_2***
Optical basicity	1.00	0.78	0.61	0.48	1.24	1.43	0.61	0.88

The new sulphide capacity expression:

$$\mathrm{Log}C_S = -6.08 + \frac{4.49}{\Lambda} + (15893 - 15864/\Lambda)/T \quad (3\text{-}52)$$

Eight parameters are required for calculating the sulphide capacity, based on the optical basicity concept (Zhang et al., 2013).

Recently, Hao & Wang, (2015) proposed an updated sulphide capacity model for the CaO-Al_2O_3-SiO_2-MgO slags based on the corrected optical basicity values. It considers the charge effect compensation of Ca^{2+} to $[AlO_4]^{5-}$ on sulfide capacity, which will enhance the accuracy of the prediction in the case of basic Al_2O_3 containing slags.

The predicted mean deviation of the Young et al. (1992) model, Zhang et al., (2013) model, the KTH (Nzotta et al., 1999) model and Hao & Wang, (2015) are 38.23%, 12.56%, 7.07%, 3.23% respectively (Hao & Wang, 2015). Although the mean deviation for the Hao & Wang, (2015) model was less compared to that of Zhang et al., (2013), it only includes CaO-Al_2O_3-SiO_2-MgO slag systems, and does not consider other components in the slag. Although, the KTH model(Nzotta et al., 1999) has a mean prediction error of 7.1%, it uses complex interaction parameters, based on calculations of sulphide capacity. Zhang et al., (2013) model considered 8 slag components and optical basicity parameters for the calculation of sulphide capacity, resulting in a mean deviation error from the experimental data for the slag components of 12.56%, which is reasonable error when compared to the

Young et al., (1992) model. Therefore the model of Zhang et al is used in the current work because it offers the best balance of precision and versatility.

The mass transfer balance for desulphurization is:

$$k_m^S C_{V_m}\left(X_{S,m}^b - X_{S,m}^*\right) = k_{sl}^S C_{V_{sl}}\left(X_{S,sl}^* - X_{S,sl}^b\right) \quad (3\text{-}53)$$

Using equation (3-53) with the equilibrium partition coefficient, L_s', the interfacial concentration of $X_{S,m}^*$ and $X_{S,sl}^*$ are obtained and the flux of sulphur may be calculated. Figure (3-14) shows the effect of the updated model on the calculated desulphurization behaviour at high and low stirring conditions. Although the changes in the Figure (3-12) and (3-13) are negligible in practical terms the data presented mirrors the equivalent calculation for MnO in the slag, providing confidence that the model is operating properly.

Once all the interfacial mole fraction values are calculated at a time step t, the update of the slag and steel bulk concentrations proceeds with a first-order time integration:

$$M_xO_y|_{t+1(new)} = M_xO_y|_{t(old)} + \Delta M_xO_y|_t \quad (3\text{-}54)$$

$$M|_{t+1(new)} = M|_{t(old)} + \Delta M|_t \quad (3\text{-}55)$$

The values in equations (3-56) and (3-57), are in moles of the respective species, the changes in moles for the composition during a time step, Δt, are calculated using:

$$\Delta M_xO_y|_{t,Sl-St} = -k_{sl}^{M_xO_y}.A.C_{V_{sl}}\left(X_{M_xO_y}^b - X_{M_xO_y}^*\right).\Delta t \quad (3\text{-}56)$$

$$\Delta M|_{t,\ Sl-St} = -k_m^M.A.C_{V_m}\left(X_M^b - X_M^*\right).\Delta t \quad (3\text{-}57)$$

Where, k_m^M and $k_{sl}^{M_xO_y}$ are the mass transfer coefficients in m/sec for convective transport in the metal and slag; $C_{V_{sl}}$ and C_{V_m} are the total molar concentrations of the metal and slag phase respectively.

3.3.2.3 Recommended updates for high manganese steel:

For better understanding of the steelmaking process, kinetic behaviour provides insight into the mechanism of reactions, in which slag and metal are involved. Moreover, many reactions occur simultaneously during the ladle process, which leads to each of the reactions influencing the kinetic behavior of others. Since within the slag-steel model, slag-steel reactions are interconnected, modifications in the thermodynamics will have an impact on the kinetic behavior of the process. Figure (3-12), (3-13) and (3-14) shows the output from the model comparing kinetic behavior before and after thermodynamic updates. The updated final model for [S], [Mn], (MnO) weight percentage is plotted against processing time (minutes). The following thermodynamic parameters have been upgraded:

- Interaction parameters
- Desulphurization model
- Equilibrium constant for high manganese compositions

3.3.3 Results from the updated kinetic model for high manganese steel

The performance of the kinetic model was evaluated in order to analyze the thermodynamic updates, and the influence of compositional changes in the steel and the slag system for high manganese steel. Since there is a lack of data available for the process conditions of high manganese steel, the initial composition of the steel and slag system were unknown. For simplification of the system, the steel composition was assumed to contain 15 wt% of Mn, Table (3-5) contains the detailed species composition of steels and slag. In these calculations, the mass of the steel was 160000 kg, the temperature was kept constant at 1873 K, the total oxygen of the system was 5 ppm, and the high stirring

condition (20 Nm^3/hr), are all taken into consideration for a better understanding of the kinetic behaviour of the process. No electrical arcing and additions are considered in the process, due to the influence of temperature and re-oxidation of elements in the process, respectively. Process simulation would occur for 20 minutes. Mass transfer ratios are used to describe the different slag-metal equilibria reactions. Constant mass transfer ratios were found to be sufficient for describing the state of LMF. Based on Graham & Irons (2008) recommendations, the mass transfer ratios considered are: k_{FeO}/k_{Fe} : 0.15, k_{MnO}/k_{Mn} : 0.15, k_{SiO2}/k_{Si} : 0.005, and k_{Al2O3}/k_{Al} : 1.

Table 3-5: Steel and slag composition in weight percentage for updated kinetic model

Steel Composition:

Elements	**C**	**Mn**	**P**	**S**	**Si**	**Cu**	**Ni**	**Cr**	**Sn**	**Mo**	**Al**
Weight %	0.056	15	0.004	0.0200	0.3	0	0	0.22	0	0	0.3

Elements	**N**	**Nb**	**Ca**	**B**	**Ti**	**Mg**	**O**	**Fe**
Weight %	0.004	0.0002	0.0001	0.0001	0.0006	0.00004	0.0005	Remaining

Slag composition:

Oxides	**K_2O**	**P_2O_5**	**TiO_2**	**CaS**	**FeO**	**CaO**	**MnO**
Weight%	0	0	0.5	0.5	3	47	2

Oxides	**SiO_2**	**MgO**	**Al_2O_3**	**Other oxide**
Weight%	5	8	30	4

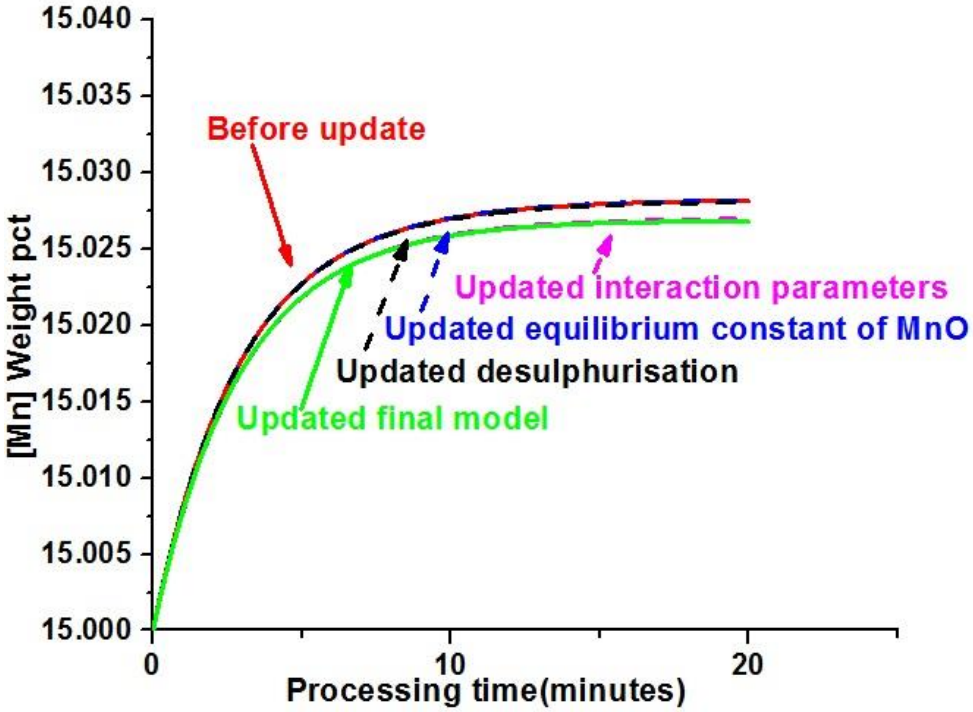

Figure 3-12: Comparison of updated model with unmodified model kinetic behavior of [Mn] wt%

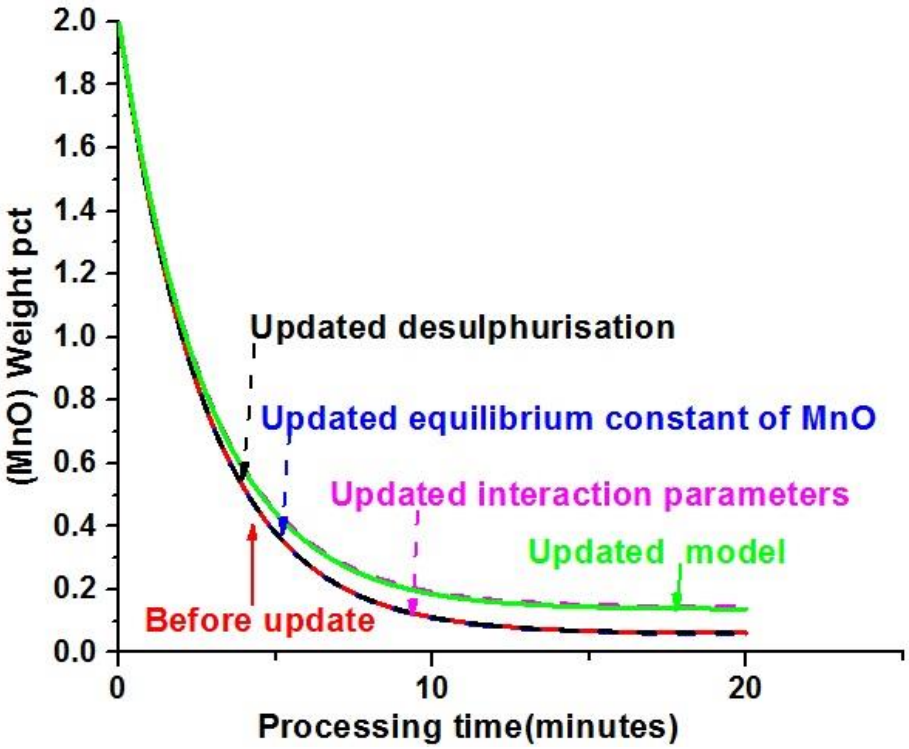

Figure 3-13: Comparison of updated model with unmodified model kinetic behavior of (MnO) wt%

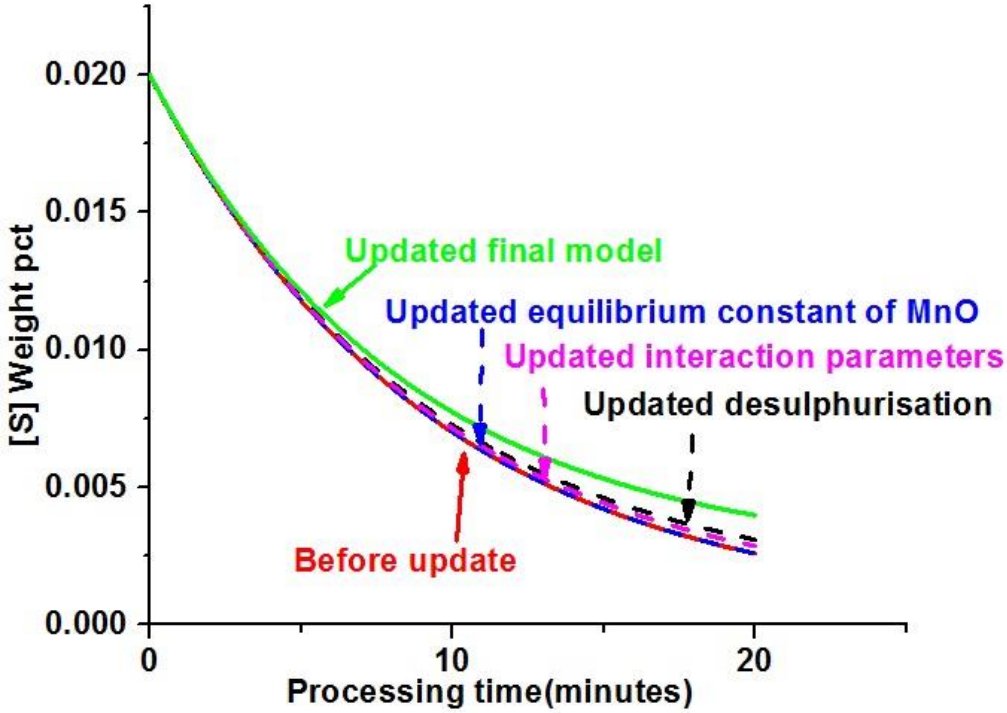

Figure 3-14: Comparison of updated model with unmodified model kinetic behavior of [S] wt%

3.3.4 Coupling of kinetic model for MnS and AlN inclusions in the ladle for high manganese steel

A kinetic model for inclusion growth in the ladle furnace has been discussed, for both AlN and MnS inclusions, in the previous section of this chapter. The coupling of the kinetic model for the slag-steel reactions in the ladle furnace, and the model for growth of inclusions is now made through the variation in the bulk concentrations of [Mn] and [S] for MnS inclusions, and [Al] and [N] for AlN inclusions in the steel during a time step, Δt, with a first-order time update:

$$[\mathrm{Mn}]_{t+1} = [\mathrm{Mn}]_t + \Delta[\mathrm{Mn}]_{t,\mathrm{St-Sl,Desulphurisation}} + \Delta[\mathrm{Mn}]_{t,\mathrm{St-Inclusion(MnS)}} \quad (3\text{-}58)$$

$$[\mathrm{S}]_{t+1} = [\mathrm{S}]_t + \Delta[\mathrm{S}]_{t,\mathrm{St-Sl,Desulphurisation}} + \Delta[\mathrm{S}]_{t,\mathrm{St-Inclusion(MnS)}} \quad (3\text{-}59)$$

$$[\mathrm{Al}]_{t+1} = [\mathrm{Al}]_t + \Delta[\mathrm{Al}]_{t,\mathrm{St-Sl,Desulphurisation}} + \Delta[\mathrm{Al}]_{t,\mathrm{St-Inclusion(AlN)}} \quad (3\text{-}60)$$

$$[N]_{t+1} = [N]_t + \Delta[N]_{t,St-Inclusion(AlN)} \quad (3\text{-}61)$$

The update by time step for [Mn] includes the variation due to the slag-steel reaction and mass transfer to the inclusions. In the case of [S] and [Al], the update of time step considers the balance for the slag-steel reactions, and desulphurization from the equations (3-58) to (3-61), as well as the mass transfer to the inclusions. For dissolved [N], the model considers the mass transfer to the inclusions, nitrogen is not present in the slag and slag-steel reactions are not considered.

A scheme with the organization of the coupled kinetic model for the three phases is shown in Figure (3-15).

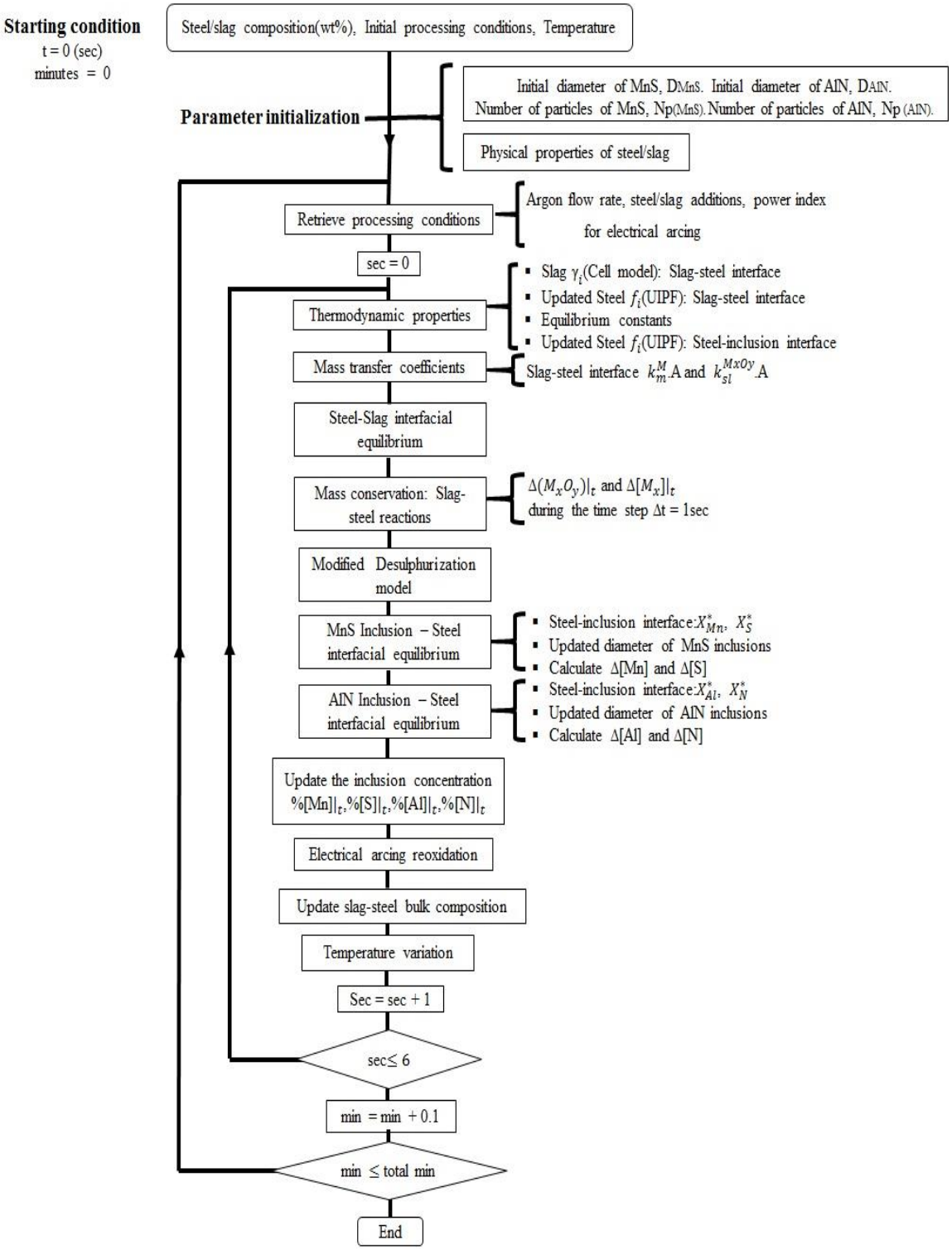

Figure 3-15: Coupled kinetic model for the slag, steel and inclusions (MnS, AlN) for high manganese steel

4 Chapter

Coupled kinetic model of Steel-Slag-Inclusion for high manganese steel in the ladle

4.1 Kinetic model analysis of slag-steel reactions for high manganese steel

Non-metallic inclusions arising during steel processing are mostly removed in the ladle, mainly during argon purging. However, small inclusions precipitate and grow in liquid steel during ladle refining and during cooling, either in the tundish or during casting, The former may be removed in the tundish, however, in the casting mold, new inclusions are produced in liquid steel for two reasons: decrease in the equilibrium solubility product with decreasing temperature, and the segregation of liquid steel components at the solidification front (Kalisz & Rzadkosz, 2013).

The goal of process model for high manganese steel is to verify the consistency of the model and its assumptions, and to assess the robustness of the simulation results, as they relate to the slag-steel-inclusion system for high manganese steel. In the work of Graham & Irons (2008), their coupled kinetic model for the slag-steel reactions, is based on the model by Robertson et al.(1984), but considered the industrial conditions of the ladle metallurgy furnace and the refining of low carbon aluminum killed steel.

The coupled kinetic model for the slag-steel-inclusions (updated in the present work) is used in the analysis presented here. The analysis considers industrial processing conditions for higher manganese steels; validation is based on data from the highest

manganese heats available to the author which do not really reach the level of 'high manganese steel' but do offer the "best available possibility" to evaluate trends with increasing manganese. Furthermore, the analysis of industrial conditions, based on the work of Graham & Irons (2008), will act as a guideline for high manganese steel analysis. This analysis will provide an insight in the steel-slag-inclusions (MnS and AlN) reaction of the kinetic process for high manganese steel.

4.2 Analysis of the coupled kinetic model with variations in the industrial heats

4.2.1 Retrieval of processing parameters from the ladle furnace operations

As described by Graham (2008), the multicomponent kinetic model considers the processing parameters applied for each heat. The information retrieved to reproduce the conditions in the ladle furnace includes: the initial mass of steel in the ladle furnace, estimation of the slag volume based on slag depth measurement, temperature measurement, argon gas flow rate of the 2 bottom porous plugs, and the energy applied for heating with electrical arcing. The chemical composition of the slag and steel at the beginning of the ladle treatment were also measured. During the course of each heat, additional samples of the slag and steel were taken to monitor the refining process. Due to confidentiality of the present industrial data and scarce availability of other industrial ladle process parameters for high manganese steel, several heat data parameters would be considered from Graham & Irons (2008) work, for the analysis of the process model. Additionally, slag and steel compositions are assumed for the process model.

4.2.2 Slag/steel additions

Input data to test the model are based on steel plant data for all the different materials for slag/steel additions are stated as follows: Al (cones), Al (briquettes), Al (wire), FeMn, FeTi, KRK Ti, FeCb, CaSi, C, CaO, FeSi. The maximum content of manganese available for a typical ladle process heat is 0.2wt% for FeMn alloy additions of 200 Kg, for hypothetical heat of 160 tonne ladle which are used to evaluate the model, FeMn alloy additions of 12000 Kg are required.

4.2.2.1 Ferromanganese alloy additions

During iron and steel production, manganese is mostly added to the molten steel in the form of ferromanganese (FeMn) or silicomanganese alloy. The chemical composition of ferromanganese alloys will be in range of, Mn: 65.6-81.9%, Si: 2.29-12.3%, Fe: 6.77-18.9%, C: 2.88-7.25 %, and S: 0.021-0.036% (Saridikmen, Kucukkaragoz, & Eric, 2007). For our present analysis, Mn: 82%, S: 0.02%, Si: 6%, and Fe: 11.98% is used in the calculation of FeMn alloy additions. In order to get the desired manganese weight percentage in the steel, for high manganese steel, large amounts of FeMn alloys are added during the process. The present model considers the concentration of associated elements present in the FeMn alloy additions.

4.2.3 Mass transfer coefficient ratios in the slag-steel phases

For this kinetic model, the mass transfer of species between the slag and steel is described by coupling the different slag-steel reactions in order to satisfy the multicomponent equilibrium at the interface, and to balance the mass transfer rates in both phases. The mass transfer coefficients, k_M^m, for all the dissolved species in steel are assumed

to be equal, since the diffusivities of the solutes in molten steel have similar values. As summarized by Szekely & Themelis (1971), for majority of cases the overall transfer between the slag and steel is controlled by resistance in the steel phase, even though the diffusivities and mass transfer coefficients in steel are greater than in the slag. It is noticed from equation (4-1), a large value of partition coefficient L, indicates metal control in the steel-slag reactions.

$$\frac{1}{k_{ov}} = \frac{1}{k_m} + \frac{1}{L.k_{sl}} \tag{4-1}$$

Here,k_{ov} is the overall mass transfer coefficients including both slag and steel.It is apparent from this equation that for elements that partition strongly to the slag $k_{ov} = k_m$. This is the rationale behind the rather too general statement by Szekely & Themelis (1971) regarding control in the metal phase. The mass transfer coefficients of the components in the slag, k^{sl}_{MxOy}, are calculated from individual ratios with the mass transfer coefficient of the species in steel. $k^{sl}_{\mathrm{MxOy}} / k^{m}_{\mathrm{M}}$, this approach was proposed in the model by Robertson and colleagues (1984) and also used in the kinetic models by Kitamura et al., (1991), Okuyama et al.,(2000) and Harada et al., (2013).

Graham & Irons (2010) proposed the use of separate mass transfer ratios for the transport of species in the slag, that is: k^{sl}_{FeO}/k^{m}_{Fe}, k^{sl}_{MnO}/k^{m}_{Mn}, k^{sl}_{SiO2}/k^{m}_{Si}, k^{sl}_{TiO2}/k^{m}_{Ti} and $k^{sl}_{Al2O3}/k^{m}_{Al}$. The value of each ratio was selected in order to obtain agreement with the measured industrial compositions in the slag and steel. Detailed analysis on the mass transfer coefficient ratios were carried out by Galindo et al. (2015), who performed sensitivity analysis for the mass transfer coefficient ratios of k^{sl}_{FeO}/k^{m}_{Fe}. Based on the work carried out in the last section of this chapter for k^{sl}_{FeO}/k^{m}_{Fe} and suggestions from the steel

makers, k_{FeO}^{sl}/k_{Fe}^{m} of 0.15 and k_{MnO}^{sl}/k_{Mn}^{m} of 0.15 was used for the present kinetic model. In this kinetic model, the assumption of transport control in the steel side is applied by equating the ratios of the mass transfer coefficients, k_{CaO}^{sl}/k_{Ca}^{m}, $k_{MgO}^{sl}/k_{Mg}^{m}$and $k_{Al2O3}^{sl}/k_{Al}^{m}$, to unity.

4.2.4 Stirring analysis for the inclusions

Argon gas stirring is applied with two bottom porous plugs. Typical variations in the gas flow rate, illustrated in Figure (4-1), are employed in the current work to evaluate the performance of the model for high manganese steel. The stirring power, ε, is calculated using the expression derived by Pluschkell (1981).

$$\varepsilon = \left(\frac{101330}{273}\right).\left(\frac{Q.T}{M}\right).ln\left(\frac{\rho.g.h}{101330}\right) \quad (4\text{-}2)$$

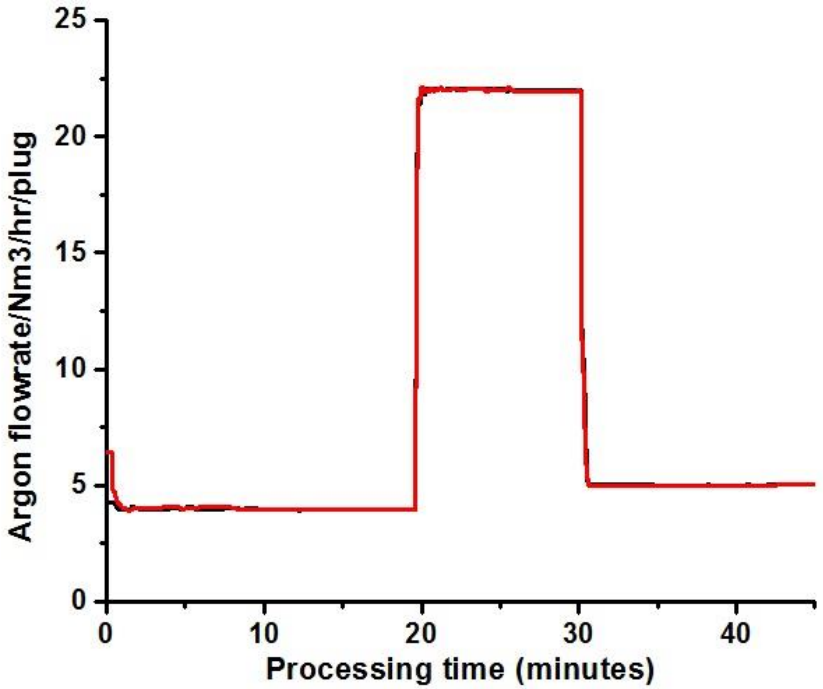

Figure 4-1: Gas stirring during treatment from an industrial heat

Where Q, is the argon gas flow rate [Nm^3/sec], M is the total mass of the steel [kg],

ρ is the steel density [kg/m^3], and h is the depth of the gas injection [m], T is the temperature [Kelvin]; which is included in the model by temperature updates due to electric arcing.

4.3 Kinetic model analysis of slag-steel reaction with single additions of FeMn alloys

The coupled kinetic model for the slag-steel model (excluding MnS and AlN inclusion from the coupled kinetic model) was used, considering the industrial processing conditions of the refining heats without calcium treatment. Assumptions are considered for initial steel and slag compositions shown in the Table (4-1), due to the unavailability of industrial data for high manganese steel. Large additions of FeMn (Ferromanganese) alloys, added as single time additions, are assumed to be at 1873K during the process. Isothermal conditions are maintained throughout the process at 1873K. Stirring condition data used were from Graham & Irons (2008), the entire process took almost 45 minutes.

Table 4-1: Initial bulk composition of steel and slag compositions in wt%

Steel composition:

Elements	C	Mn	P	S	Si	Cu	Ni	Cr	Sn	Mo	Al
Weight %	0.05	0.1	0.006	0.033	0.007	0.1	0.03	0.06	0	0	0.03

Elements	N	Nb	Ca	B	Ti	Mg	O	Fe
Weight %	0.006	0.0002	0.0002	0.0001	0.0007	0.00001	0.0005	Remaining

Slag composition:

Oxides	K_2O	P_2O_5	TiO_2	CaS	FeO	CaO	MnO
Weight%	0.005	0.01	0.32	0.46	2.92	48.26	1.87

Oxides	SiO_2	MgO	Al_2O_3	Other oxides
Weight%	4.86	8.89	28.59	3.81

Based on discussions with industrial partners, their interest in producing high manganese steel with manganese typically in the range of 5-10 wt%. In the current case, ferromanganese was added for a required manganese content of 5%. Figure (4-2) illustrates the weight percentage of manganese and stirring conditions, which is controlled by an argon flow rate measured in (Nm^3/hr), plotted with respect to processing time in minutes. Ferromanganese alloy additions are carried out as a one-time addition at the 16 minute mark

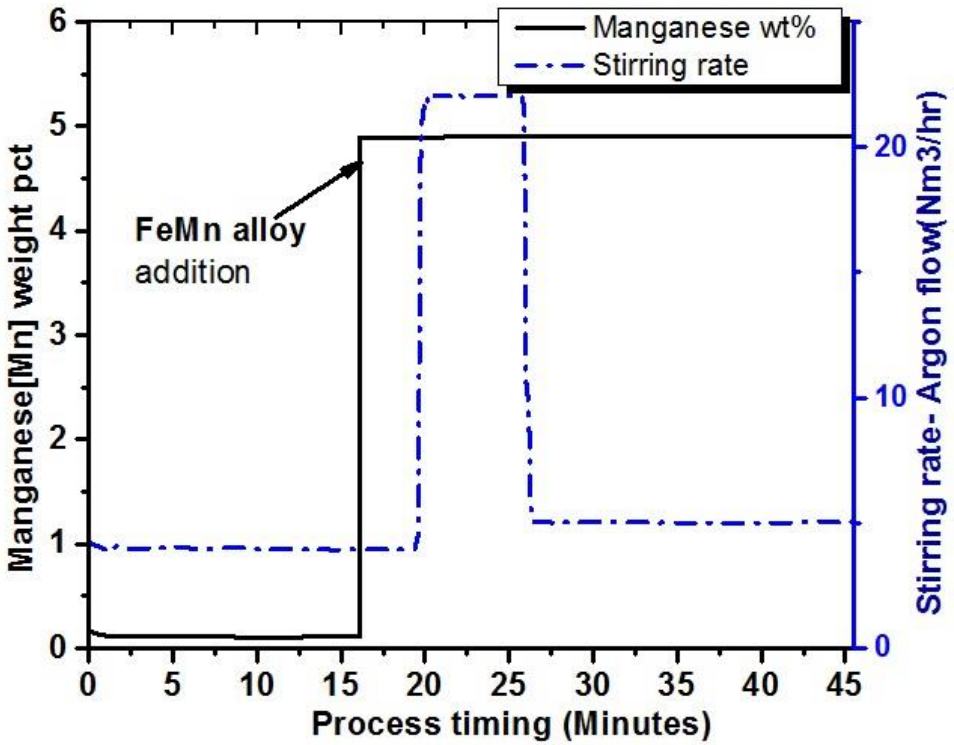

Figure 4-2: Calculated bulk content of [Mn] in the steel for one time FeMn alloy addition and with the stirring rate

of the process. Under low stirring conditions, the addition causes a sudden increase in the manganese weight percentage. Furthermore, at high stirring conditions from 20 to 26

minutes, the manganese content has a negligible change in composition of the steel.

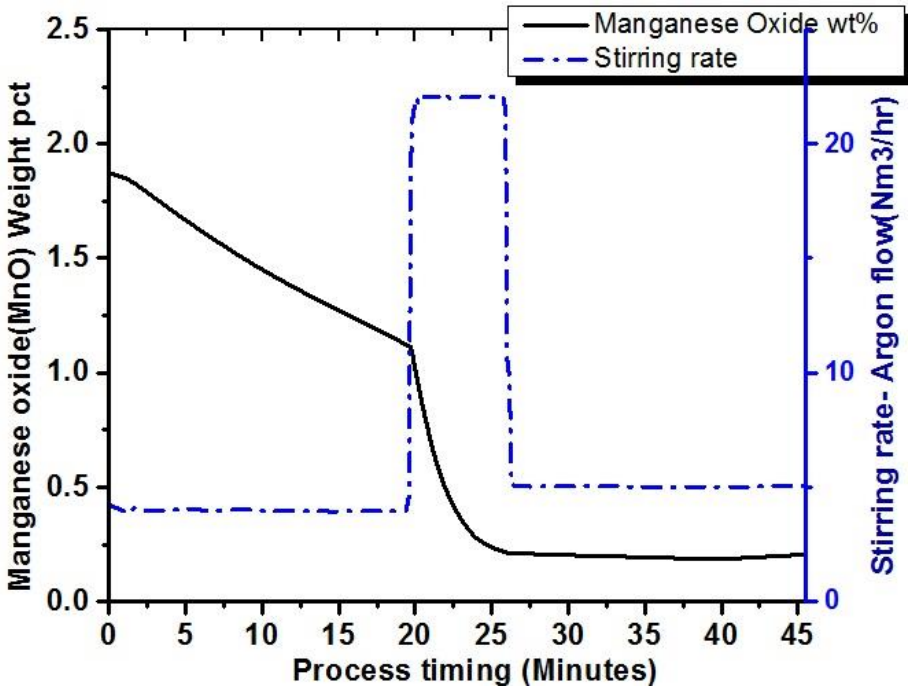

Figure 4-3: Calculated bulk content of (MnO) in the slag for one time FeMn alloy addition and with the stirring rate

Results from the analysis for MnO wt% in the slag, with the argon flow rate shown in figure (4-3), we could observe a gradual decrease in MnO wt% at low stirring regime. Even with the addition of FeMn alloys, 16 minutes into the process, reduction of manganese oxide from the slag occurs without any influence of FeMn alloy additions. Changing to the high stirring regime caused a drastic increase in the rate of MnO reduction. MnO reduction from the slag made a negligible difference to the steel because of the low slag to steel weight ratio of 1:63.

However, further analysis on the mass balance of the updated model for the high alloy contents with respect to steel and slag is required. It can be observed from the analysis that the wt% of the FeO (ferrous oxide) and MnO (manganese oxide) in the slag decreased

and reduced to iron and manganese in the steel.

4.3.1 Analysis of oxygen content for the mass balance of slag-steel kinetic model

Oxygen is one of the most important elements to control during ladle refining. It is especially important to lower the dissolved oxygen content, so that oxides and CO gas are not formed during solidification and also to promote desulphurization of the steel. The steel in a converter or an electric arc furnace usually has a high oxygen content, which normally is set by equilibrium with dissolved carbon. However, it also depends on the slag and alloy composition in the steel. During the tapping of steel into the ladle, predeoxidation is normally carried out. The typical dissolved oxygen content is 30–200 ppm, at a steel temperature of 1600^{o}C. Often, the dissolved oxygen content needs to be lowered further to produce steel of a lower inclusion content. Here, aluminum in the form of wire or ingots is added to the steel. This typically lowers the dissolved oxygen to approximately 2–5 ppm at steelmaking temperatures and creates alumina inclusions in the steel some of which will float out during ladle treatment.

4.3.1.1 Model assumptions for mass balance analysis of slag-steel reaction

During ladle refining, reoxidation of the steel, due to reaction with the slag and electrical arcing, can occur. Analyzing the mass balance of slag-steel reactions under different oxygen contents in the steel considering 5ppm and 60ppm under low and high gas stirring regimes, which were the reported conditions from ArcelorMittal Dofasco (Graham & Iron, 2008). Figures (4-4) show the change in MnO in the slag as a function of dissolved oxygen and stirring conditions. Data for the low gas flowrate,5 Nm^3/hr per plug, is represented by dotted lines, while data for the high gas rate, 20 Nm^3/hr per plug, is

represented by solid lines. The influence of inclusions in the steel was not considered for this analysis. Time zero in this figure was set at the point where ferromanganese was added. The mass of the steel in these calculations was set to 164500 kg, while the initial mass of the slag was 2590 kg. Isothermal conditions were fixed at 1600°C. The initial composition of the steel and slag are shown in Table (4-2).

Table 4-2: Initial steel and slag composition in wt% for mass balance analysis

Steel composition:

Elements	**C**	**Mn**	**P**	**S**	**Si**	**Cu**	**Ni**	**Cr**	**Sn**	**Mo**	**Al**
Weight %	0.05	**5**	0.006	0.004	0.007	0.1	0	0.06	0	0	0.03

Elements	**N**	**Nb**	**Ca**	**B**	**Ti**	**Mg**	**O**	**Fe**
Weight %	0.006	0.0002	0.0001	0.0001	0.0006	0.00004	0.0005	Remaining

Slag composition:

Oxides	**K_2O**	**P_2O_5**	**TiO_2**	**CaS**	**FeO**	**CaO**	**MnO**
Weight%	0.005	0.01	0.32	0.46	2.92	47.76	2.87

Oxides	**SiO_2**	**MgO**	**Al_2O_3**	**Other oxide**
Weight%	4.86	8.89	28.09	3.81

Based on the mass balance analysis, Figure (4-4) shows the weight percentage of manganese oxide in the slag as a function of time and stirring conditions. For the case of high stirring, by the end of the 20 minutes, there is a significant decrease in the manganese oxide content in the slag for both 5ppm and 60ppm initial oxygen in the steel. Whilst this is reflected in a negligible change of manganese in the steel from 5 to 5.01wt%, a significant

change in the slag MnO content would have an influence on the sulphur partition ratio.

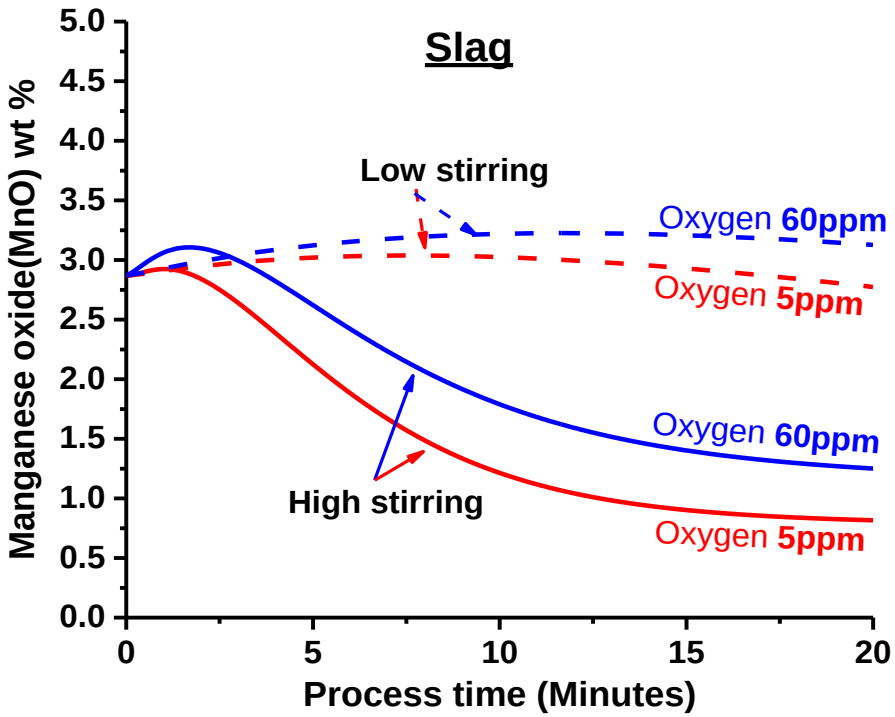

Figure 4-4: Calculated bulk content of (MnO) in the slag under high and low stirring conditions for 5 and 60ppm of oxygen in the bulk steel

From the plots, as expected the steel with an initial 60 ppm oxygen shows a higher MnO weight percentage in the slag, compared to the 5ppm oxygen case. Under low stirring conditions the model predicts a slight increase in MnO which is likely caused by FeO in the slag oxidizing Mn in the metal.

4.3.2 Coupled kinetic model analysis on slag-steel-inclusion with multiple additions of FeMn alloys

Analysis of the coupled kinetic model of slag-steel-inclusion for high manganese steel is performed for multiple additions of FeMn alloys during different time intervals. Examinations of the effect on manganese recovery in the steel, as one time additions of FeMn alloy throughout the process. Moreover, investigations are performed on FeMn alloy

additions at multiple time points in the ladle refining process. Equal proportions of ferromanganese alloys were added at three intervals to obtain 5 wt% in the steel. FeMn alloys are assumed to be added at 1873K during the process.

4.3.2.1 Model assumptions for multiple addition of FeMn alloy influencing inclusion growth

Assumptions are made for initial steel and slag compositions, because of the lack of industrial data for high manganese steel. Isothermal conditions are maintained throughout the process at 1873K. Assuming 0.1 wt% of aluminum in the steel, due to additions of aluminum during pre-deoxidation, no further additions of aluminum are carried out during the process. Stirring condition data are used from Graham & Irons (2008). The blue dotted line indicates the argon flow rate (Nm^3/hr), which is plotted with the manganese content in the steel over the processing time in minutes, as shown in Figure (4-5). Considering, the entire duration of the process is 40 minutes.

MnS and AlN inclusion models are coupled in the slag-steel model to observe the growth/shrinkage of the inclusions during the alloying additions. Moreover, the diameter of the MnS and AlN particle nucleation sites are unknown, therefore we assumed the seed of particles to be 0.1 microns. Assuming total number of seed inclusions, N_p, as $10^{12}/m^3$ at

the start of the heat analysis, which are dispersed in the ladle and are kept constant throughout the process.

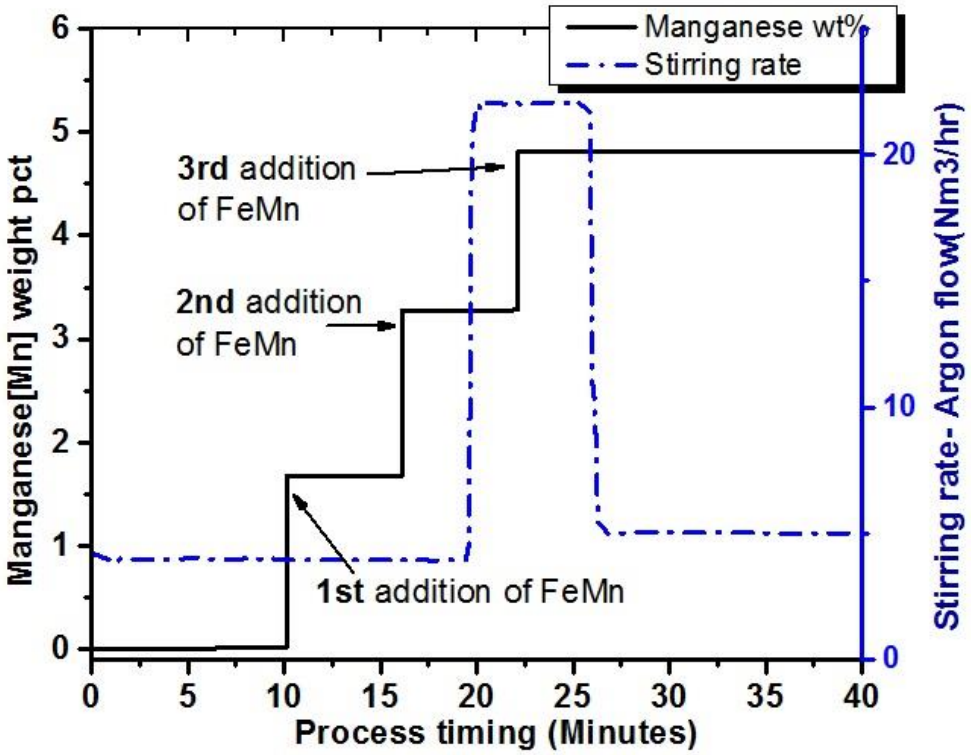

Figure 4-5: Calculated bulk content of [Mn] in wt% for multiple additions of FeMn alloy under stirring conditions of industrial heat

Results from the analysis indicates negligible change at the end of the process regarding the manganese content in the steel, comparing both the one time and multiple addition of FeMn alloys. Although FeMn additions are carried out during the process, growth of MnS inclusions could not be observed. The growth and equilibrium stability of MnS inclusions will be discussed later in this chapter. AlN inclusions grew during the process.

Figure (4-6) shows the increase in diameter of AlN inclusions as a function of time. The growth of AlN inclusion ceases after 4 minutes, because the nitrogen content in

the steel is consumed.

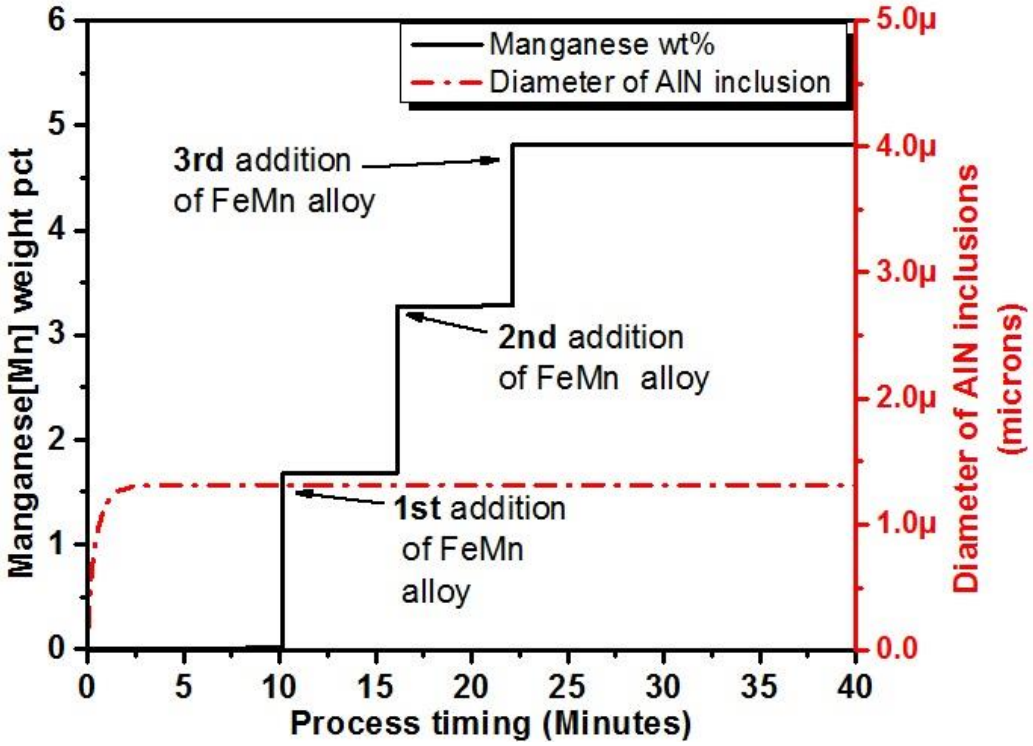

Figure 4-6: Calculated bulk content of [Mn] in wt% for multiple additions of FeMn alloy, dashed lines correspond to the diameter of the AlN inclusions

4.4 Analysis of inclusions in high manganese steel

Simulation models of reaction systems are routinely created to understand reaction mechanisms, kinetic behavior and process yields under various operating conditions. From this perspective, a model will help to support or disprove a given description of reality. However, as mentioned by Saltelli et al. (2012), models are built on the presence of uncertainties of various levels, such as the kinetic and thermodynamic values used for the calculations. In contexts where very complex kinetic models were used, the term sensitivity analysis often refers to a 'what-if' analysis, where the input factors of the simulation procedure are varied one at a time. As mentioned by Pianosi et al.(2016), through sensitivity

analysis we gain essential insights on model behavior, its structure, and its response to changes in the model inputs.

The formation and evolution behavior of MnS and AlN are discussed based on thermodynamics and kinetics to enhance understanding of the formation behavior of main inclusions in high manganese steel.

4.4.1 Analysis of kinetic behavior of AlN inclusion

The present work deals with the growth behavior of AlN precipitates during kinetic process modelling of high manganese steel. As aluminum shows high chemical affinity to both oxygen and nitrogen in steel, the correct determination of whether the conditions are favorable for AlN formation depends on the thermodynamic equilibrium of the inclusions. The structure of active aluminum nitride forms in the liquid state, which was explained in previous chapters, requires sufficient levels of aluminum and nitrogen content in steel.

4.4.1.1 Analysis for the nitrogen content in the steel in the model validation

Further analysis was carried out for slag-steel-inclusion model for duration of 20 minutes. The initial steel and slag composition considered for the analysis is shown in table (4-2), with an assumed aluminum content of 0.1 wt%. Additionally, the initial inclusion diameter is considered to be 0.1 microns and the number of seed particles (N_p) of the inclusions is considered to be $10^{12}/m^3$. The evolution of inclusions depends on the concentration of Al and N in the steel. In this sensitivity analysis, the concentration of nitrogen in the steel is a variant of 1ppm, 20ppm, 40ppm, 60ppm, and 80ppm. Isothermal

temperature of 1570^{o}C is maintained thorough out the process. No nitrogen pick from the atmosphere was considered in the model.

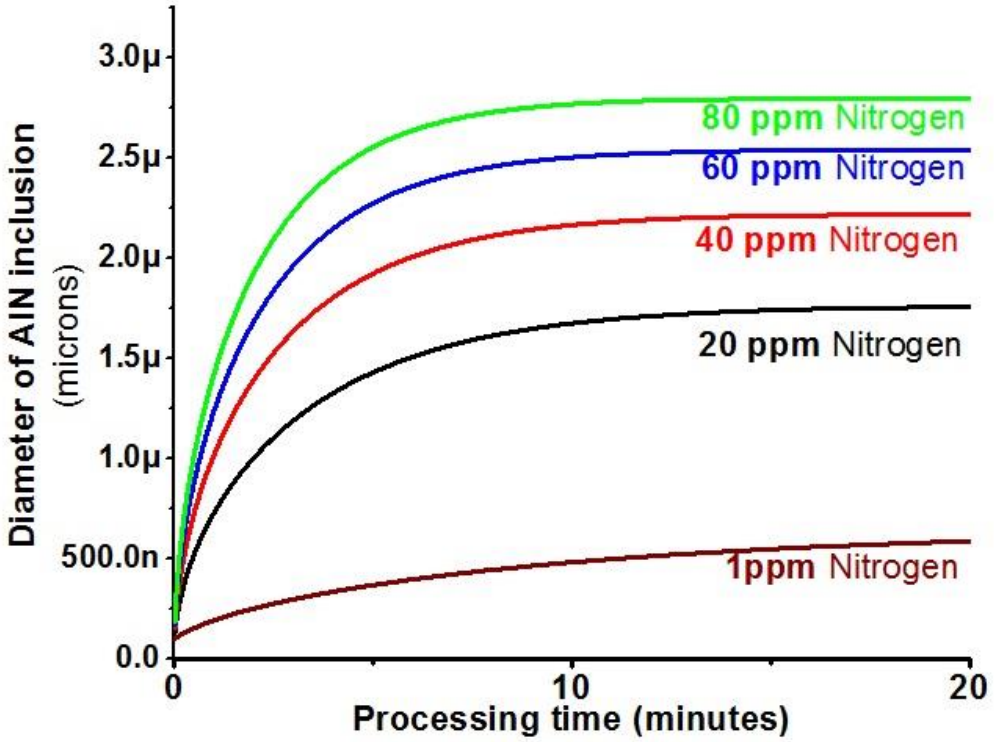

Figure 4-7: Calculated diameter of AlN inclusions for different nitrogen contents in steel for steel-slag-AlN inclusion system at 1843K

Results from the analysis show that, as the concentration of nitrogen in the steel increases, the diameter of AlN inclusion increases, as shown in figure (4-7). Moreover, the effect of high and low stirring conditions does not have any influence on the growth of the diameter of AlN inclusions. The indifference of stirring conditions on particle growth can be related to the assumed value of Sherwood number of 2 for small inclusions in this calculation.

4.4.1.2 Sensitivity analysis for the total number of inclusions in the model validation

Sensitivity analysis investigates how the variation in the output of a numerical model can be attributed to variations of its input factors. The more realistic conditions for the number of inclusions during steel refining involve processes for the removal, during different operations in the ladle furnace. Due to the size of inclusions, the liquid steel and the inclusions move as a unit. As a result, inclusions can be removed from the steel by reaching the slag-steel interface, where they can be absorbed in the slag (Holappa, 2014).

AlN precipitated from liquid steel, either floats out from liquid steel or remains as solid inclusions, which present as non-metallic inclusions during the casting process. In calculations with the coupled kinetic model, the number of inclusions N_p is varied. Furthermore, N_p is obtained by assuming the number of nucleation sites for the growth of inclusions. Based on the information provided by the industrial partners, the number of particles could be in the range of 10^{10} - $10^{13}/m^3$. The sensitivity analysis is carried out by varying the number of particles per m^3. Initial composition with 0.1wt% aluminum of the steel and slag chemistry, shown in table (4-2) are considered, remaining parameters are kept constant. From the results in figure (4-8), we observe that as the number of particles of AlN inclusions increase, the diameter of inclusions decrease. This is due to the decrease in concentration distribution of nitrogen and aluminum per inclusion particle present in the steel.

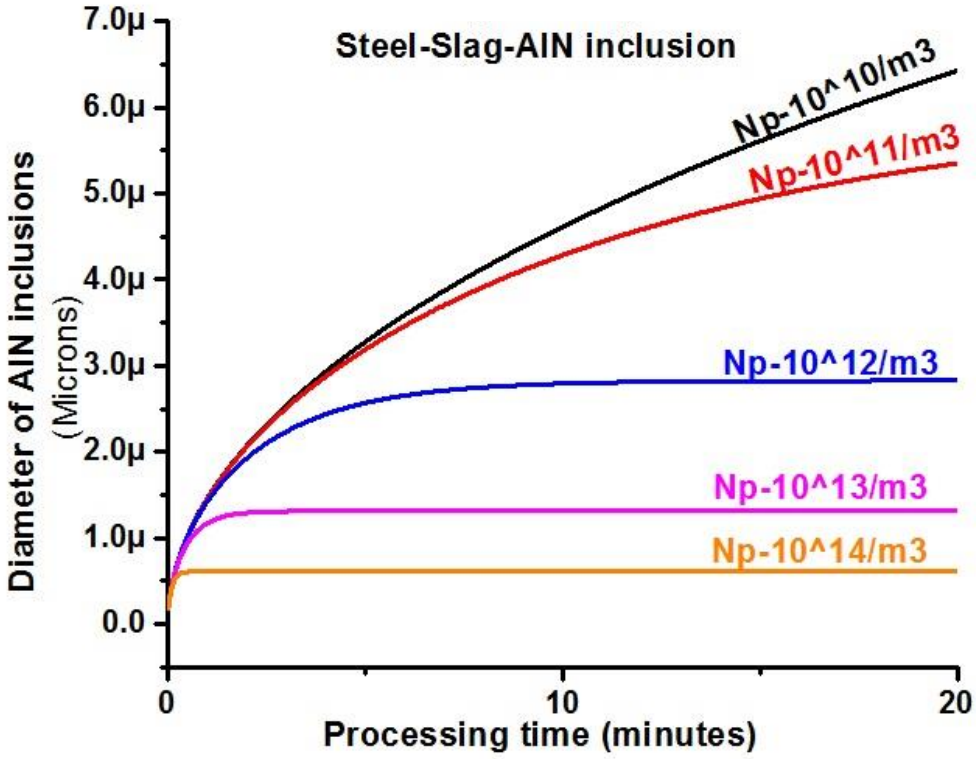

Figure 4-8: Calculated diameter of AlN inclusions for different number of particles, Np/m^3 in the steel

4.5 Kinetic analysis on the equilibrium solubility and growth of MnS inclusion

MnS inclusions in steel are formed from reaction (4-3)

$$[Mn] + [S] = (MnS) \quad (4\text{-}3)$$

The growth of MnS inclusion initiates when the concentration product of [Mn] and [S] reaches the equilibrium solubility product, and the MnS grows under mass transport control of manganese and sulphur in the liquid steel. The equilibrium solubility product values of Mn and S are calculated by the thermodynamic equilibrium values (Kang, 2010), which are discussed in the previous chapter. For most steels, [Mn] and [S] levels are not

high enough for the formation of MnS at liquid steel temperatures. Therefore, the MnS inclusion is commonly not found in liquid steel. However in high manganese steel, the increase in percentage of [Mn] has the potential to cause MnS formation leading to the need of further investigation on the growth of MnS inclusions.

4.5.1 Phase stability for the formation of MnS inclusion

The phase stability diagram of the MnS inclusion formation, for required amount of sulphur and manganese weight percentage with respect to temperature, is shown in figure (4-9).

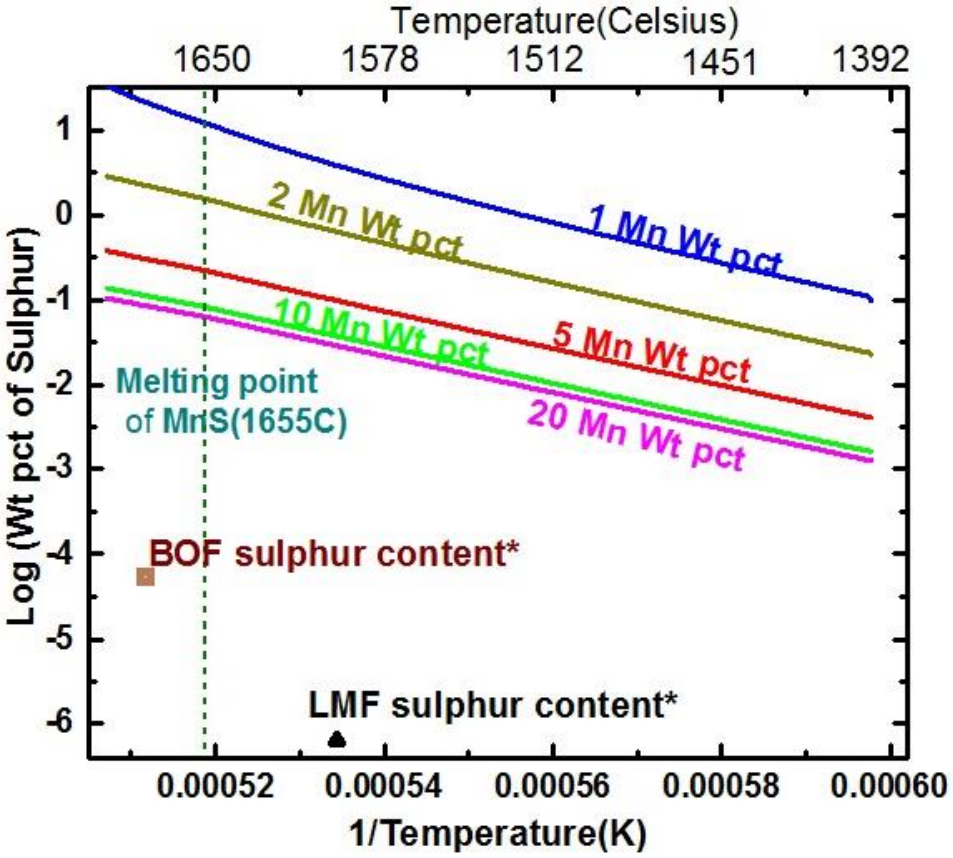

Figure 4-9: Phase stability of MnS inclusion, with respect to temperature (Kelvin)

The different manganese weight percentage concentrations of 1, 2, 5, 10, 20,

respectively, are plotted for the sulphur content in the steel by varying the temperature range, between 1400°C to 1700°C, using the thermodynamic equilibrium constant (Kang, 2010). Melting point of MnS (Staffansson, 1976), 1655±5°C, is indicated in figure (4-9). A change of slope is observed at the melting point, indicating the change of MnS inclusions from solid to liquid inclusions.

The required amount of sulphur and manganese for the formation of MnS inclusions is 900ppm and 16wt%, respectively. This quantity is much greater than the typical amount of sulphur and manganese content observed during steel making process. Typical sulphur content obtained from the industrial data from BOF and LMF process are below the phase stability of MnS inclusion as shown in the Figure(4-9). The above mentioned concentrations are obtained from the analysis carried out in coupling the slag-steel-MnS inclusion model, for the formation and growth of inclusions at 1570°C, using thermodynamic equilibrium constants (Kang, 2010), as shown in Table (4-3).

From the thermodynamic data collected from different sources for free energy, constants for MnS formation as described by Equation (4-4) listed in table (4-3).

$$[Mn]_{1wt\%}+[S]_{1wt\%}=MnS_{(s),1wt\%} \quad (4-4)$$

Table 4-3: Thermodynamic equilibrium constant values and Gibbs free energy of MnS at 1843K.

	ΔG^{o}_{MnS}(J/mole) (at 1843K)	K_{MnS} (at 1843K)	References
Log K_{MnS}= 6890/T-4.16	14872.35	0.37	(Yan, Guo, & Blanpain, 2014)
Log K_{MnS}=-8817.0/T+5.16	-13264.3	2.37	(Choudhary & Ghosh, 2009)
*G^{o}_{MnS} =-227939.7765 + 241.3719T – 47.6976TlnT – 0.0037656T^2 (J/mole) for T < 1928K	4870.572	0.875	(Kang, 2010) referenced from (Mills, 1974)
$\Delta G^{o}_{MnS} = -168822 + 98.22T$ (J/mole)	12197.46	0.45	(Choudhary & Ghosh, 2008)
LogK_{MnS} = -8627/T+4.745	2259.626	0.86	(Wei, Liu, & Cai, 2002)
Log [%Mn].[%S]= -9200/T +5.3	-10871.7	2.03	(Oikawa et al., 1995)
Log K_{MnS}=-9433/T+5.19	2530.222	0.84	(Barin, Knacke, & Kubaschewski, 1973)
Log K_{MnS}=-6885/T+4.14	14262.43	0.39	(Turkdogan, 1975)
Estimated from the Industrial heat chemistry	-87356.5	299.20	Industrial estimate

'*' Note: indicates that G^{o}_{MnS} is in Raoultian state, converted to Henrian state using $\Delta G^{o}_{Mn,(1wt\%)} = 4080 - 38.2T$, $\Delta G^{o}_{\frac{1}{2}S_2,(1wt\%)} = -135000 + 23.4T$ (Seetharaman, McLean, Guthrie, & Sridhar, 2000)

From the values listed in Table (4-3), for K_{MnS} or ΔG^{o}_{MnS}, we observe the low equilibrium constant values for the formation of solid MnS inclusions at 1843K. The equilibrium constant for MnS formation from (Kang, 2010) is used for the updated kinetic model. However, the model predicts that the initial MnS seed inclusions dissolve in the steel. Moreover, growth of MnS inclusions cannot happen from the seed MnS inclusions, even at 10 wt% Mn and 600ppm of sulphur. However, samples taken from industrial heats exhibit MnS inclusions at 2 wt% of manganese and 20-40ppm of sulphur in the steel. If we use melt compositions apparently in equilibrium with the observed MnS inclusions, we can estimate an equilibrium constant, K_{MnS} = 299.20 at 1843K. It is to be noted that the author recognizes that these inclusions are unlikely to be in equilibrium with the melt but for MnS to form, the concentrations of sulphur and manganese must at least be at the equilibrium value. In other words, equilibrium is a conservative assumption in this case. This value does not agree with any of the literature values shown in Table (4-3). This discrepancy in the formation and growth of MnS inclusion could be caused during the solidification of the industrial samples, which would occur if the cooling rate was sufficiently slow.

Choudhary & Ghosh, (2008) suggested that for most steels [Mn] and [S] levels are not high enough for the formation of MnS in the bulk liquid as in the case of high manganese steel. Therefore, MnS inclusion is commonly not found in liquid steel. However, as the steel solidifies, [Mn] and [S] are rejected from the solidifying dendrites, causing an increase in their concentration in the remaining liquid (interdendritic segregation). Choudhary & Ghosh, (2009) also supported the contention that MnS inclusions in steel are formed exclusively due to segregation of Mn and S in the

interdendritic spaces towards the end of solidification. (Kalisz et al., 2015) also mentioned that formation of MnS inclusion occurs, when the steel solidifies, as a result of elemental segregation phenomena at the solidification front and further cooling of ingot.

4.6 Shortcomings and analysis of the updated kinetic model for slag-steel reaction

There are several shortcomings which have to be considered while running the slag-steel model:

4.6.1 Analysis on the crashing of the slag-steel model

The updated high manganese steel model crashes when the Al content is above 4 wt% in steel. Furthermore for higher than 3 wt% and less than 0.001 wt% of [Al] shows abnormal behavior with Al_2O_3 in the slag during the process. There might be several reasons for the crash and abnormal behavior of the code, based on the analysis of slag-steel model:

i. Robertson (1995) mentioned the Newton-Raphson solver, which was used in the Robertson model, was inclined to break down if unable to find a solution to the equations, or if accurate initial guesses are not available at every step of the calculations. He suggests that problems are really due to the complexity of the non-linear equations.

ii. Zhang et al., (2007) suggested that the error in the Al_2O_3 component of the cell model deviates with experimental data, with increase in Al_2O_3 content in the system. Increase in error of Al_2O_3, eventually leads to crashing of the model. Even though, the cell model uses binary interaction parameters predicting the binary behaviors

accurately, Zhang et al., (2007) point out that large errors in Al_2O_3 seen in the phase diagram in the CaO-Al_2O_3-SiO_2 system, and they proposed an approach to modify it by introducing ternary parameters to the cell model.

4.6.2 Analysis of mass leakage in the slag-steel closed system

The leakage of mass in the kinetic model was evaluated in order to analyze the compositional changes in the steel and slag, with the respective total mass considering the steel and slag in the system.. In these calculations, the temperature was kept constant at 1873 K, the initial dissolved oxygen in the bulk of the steel was 40 ppm, a 15 wt% of manganese is considered along with aluminum of 1.5wt%. Here, we carried out an analysis considering the total mass in the system as 163000 kg, considering steel mass as 160000 kg, and slag mass as 3000 kg in the ladle.

From figure (4-10), we can infer that there is difference in the total mass with a system experiencing high stirring condition, with and without considering the desulphurization process in the slag-steel system. Even though the desulphurization model is updated, mass leakage occurs considering the desulphurization in the slag-steel reactions. Although there is a minor mass leakage in the system, elements lost due to leakages and process leading to mass leakages is uncertain, which might lead to major changes or effects in the slag-steel reaction model. Further analysis on the species or the component that causes leakage in the system was carried out.

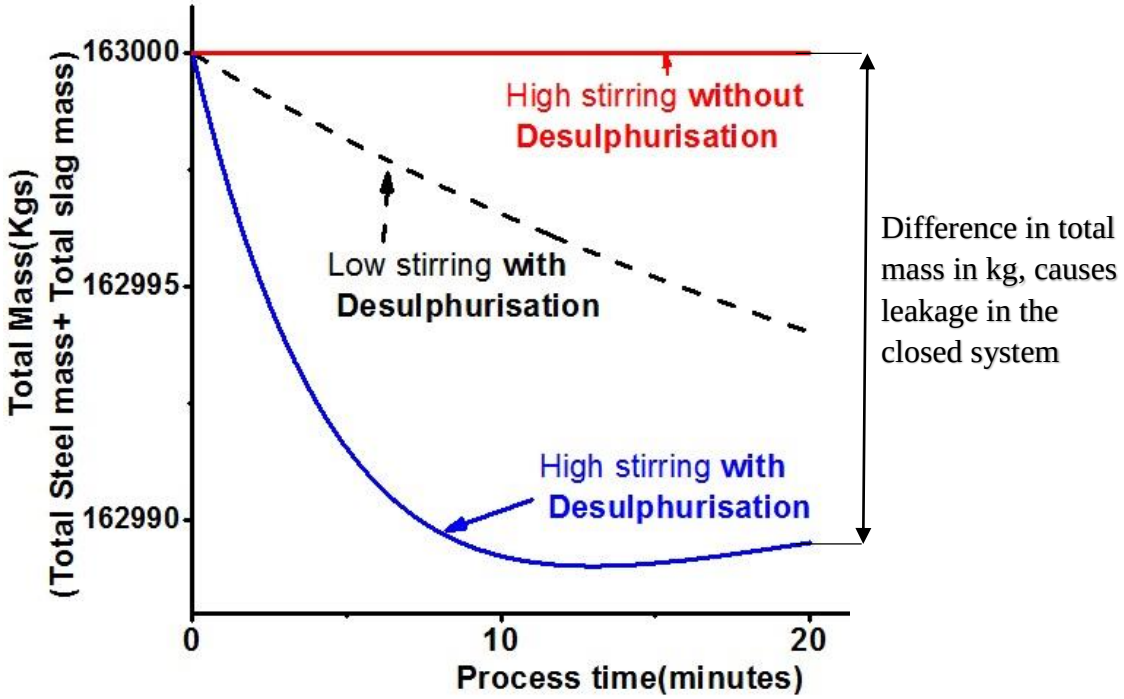

Figure 4-10: Difference in the calculated total mass in the slag-steel system with and without considering desulphurization process

Galindo & Irons (2015) carried out the mass balance update of sulphur in the slag and steel based on Graham & Irons' (2008) model, which includes an additional effect considering that [O] is released to the steel mostly in accordance to:

$$(CaO) + [S] = (CaS) + [O] \qquad (4\text{-}5)$$

Assuming that the oxygen released at the interface reacts with [Al], then:

$$2[Al] + 3[S] + 3(CaO) \rightarrow 3(CaS) + (Al_2O_3) \quad \text{at } 1600^oC \qquad (4\text{-}6)$$

Mass transfer ratios are $k_{FeO}/k_{Fe} = 0.008$; $k_{MnO}/k_{Mn} = 0.15$; $k_{SiO2}/k_{Si} = 0.005$; $k_{Al2O3}/k_{Al} = 1$

Table (4-4) shows the kilomoles of respective species and compounds for equation (4-5) at the end of the 20 minute process time.

Table 4-4: Comparison of kilomoles for the species and compounds considering with and without desulphurization process in the kinetic model for k_{FeO}/k_{Fe} = 0.008

	[Al] (kilomoles)	[S] (kilomoles)	(CaO) (kilomoles)	(CaS) (kilomoles)	(Al_2O_3) (kilomoles)
Without desulphurization	27.722	0.9981	25.147	0.4678	9.7906
With desulphurization	27.1911	0.18001	24.329	1.2859	10.0562

Δ (change in kilomoles) = without including desulphurization process – including desulphurization process in the slag-steel system.

Δ[Al] = 0.531 kilomoles ; Δ[S] = 0.8181 kilomoles; Δ(CaO) = 0.8181 kilomoles;

Δ(CaS) = -0.8181 kilomoles; $\Delta(Al_2O_3)$ = - 0.2656kilomoles;

For Δ[Al] from the product of Δ(CaS) and $\Delta(Al_2O_3)$ is

$$\Delta[Al] = \Delta[S]\left(\frac{2\ moles\ of\ [Al]}{3\ moles\ of\ [O]}\right) = 0.8181 * \left(\frac{2}{3}\right) = 0.5454 \text{ kilomoles}$$

Error in Δ[Al] = Δ[Al] in product - Δ[Al] in reactant

= 0.5454 – 0.531 = 0.0144 kilomoles

Therefore 0.0144 kilomoles becomes 0.388Kgs of Δ[Al] (1 kilomole = 27 kgs of Al)

Calculating the relative difference for Al:

$$= \left|1 - \frac{\Delta[Al] \text{ in product}}{\Delta[Al] \text{ in reactant}}\right| * 100 = \left|1 - \frac{0.5454}{0.531}\right| * 100 = \mathbf{2.7\%}$$

Desulphurization process in the slag-steel kinetic model causes a relative difference of 2.7% of Al, which is a source for mass leakage in the system.

4.6.2.1 Analysis of change in the mass transfer ratio of slag-steel reactions

Consider increasing the mass transfer ratio of k_{FeO}/k_{Fe} to 0.15, while the rest of the conditions and parameters remains the same from the previous analysis. Mass transfer ratios are k_{FeO}/k_{Fe} = 0.15; k_{MnO}/k_{Mn} = 0.15; k_{SiO2}/k_{Si} = 0.005; k_{Al2O3}/k_{Al} = 1.

Table (4-5) shows the kilomoles of respective species and compounds for equation (4-5) at the end of the 20 minute process time:

Table 4-5: Comparison of kilomoles for the species and compounds considering with and without desulphurization process in the kinetic model for k_{FeO}/k_{Fe} = 0.15

	[Al] (kilomole)	**[S] (kilomole)**	**(CaO) (kilomole)**	**(CaS) (kilomole)**	**(Al_2O_3) (kilomole)**
Without desulphurization	28.517	0.99813	25.144	0.4678	9.3930
With desulphurization	28.348	0.7442	24.890	0.7218	9.4774

Δ(Change in kilomoles) = Without desulphurization process - With desulphurization process in the slag-steel system.

Δ[Al] = 0.169 kilomoles ; Δ[S] = 0.254 kilomoles; Δ(CaO) = 0.254 kilomoles; Δ(CaS) = -0.254 kilomoles; $\Delta(Al_2O_3)$ = - 0.0844 kilomoles;

For Δ[Al] from $\Delta(Al_2O_3)$ = $\Delta[S]\left(\frac{2\ moles\ of\ [Al]}{3\ moles\ of\ [S]}\right)$= $0.2539\left(\frac{2}{3}\right) = 0.1692$ kilomoles

Error in Δ[Al] = Δ[Al] in product - Δ[Al] in reactant

= 0.1692– 0.169 = 0.0002 kilomoles

Therefore 0.0002 kilomoles becomes 0.388kgs of Δ[Al]

If we calculate the relative difference for Al

$$= \left|1 - \frac{\Delta[\text{Al}] \text{ in product}}{\Delta[\text{Al}] \text{ in reactant}}\right| * 100 = \left|1 - \frac{0.1692}{0.169}\right| * 100 = 1.18\%$$

From the analysis, we can infer that increasing the mass transfer ratios of $k_{\text{FeO/Fe}}$, the relative difference of aluminum decreases. Moreover, leakage in the closed system is caused by the aluminum in the bulk steel during the desulphurization process.

5 Chapter

Summary and Conclusions

5.1 Summary of the objectives

The main objectives of this research were to build on a previously developed ladle metallurgy model to accommodate the growth of inclusions expected in high manganese steel, and to modify the data used in the model to include higher manganese-oxide concentrations in the slag and higher manganese concentrations in the metal. These models have been updated for high manganese contents in the steel in the ladle metallurgy furnace. These two objectives were achieved as demonstrated in Chapters 3 and 4 of the thesis. The important outcomes of this research are:

- The process model can now predict the growth of manganese sulphide (MnS) and aluminum nitride (AlN) inclusions in molten steel. The model is based on mass transport at the steel-inclusion interface.
- Validation of changes to the coupled reaction model for MnS and AlN inclusions, as well as slag-steel reactions. Typical industrial conditions were employed for validation.
- Analysis of the coupled kinetic model, updated in this study, for the slag, steel, and inclusions (MnS and AlN) has been carried out. It compared the effect of the different processing conditions in the ladle furnace for the presence and growth of inclusions.

  This work provides further understanding of the types of inclusions, presence and

growth of manganese sulphide and aluminum nitride inclusions during the refining process of high manganese steel in the ladle furnace. The results of this study are expected to be useful for industrial steelmakers and process metallurgists, in order to have an overall understanding of the factors which cause and promote the presence and growth of inclusions in the ladle refining process.

5.2 Conclusions

1. The process model, which was developed to describe kinetics of coupled multicomponent slag-metal reactions (Graham & Irons, 2008), works for high manganese contents, which follows the mass balance of the reaction system with thermodynamic updates for high manganese steel. The coupled inclusion model with slag-steel reactions is one of the kinetic models that describe the changes in the growth and dissolution of inclusions in high manganese steel.

2. Close examination of the cell model predicting the thermodynamic properties, for a binary component system for ferromanganese slags, showed good agreement with the experimental data. However, extending the prediction of the cell model for multi-components in the slag, shows poor agreement with experimental results. One possible approach suggested by Zhang et al. (2007), was to modify the cell model that used binary parameters for prediction of slag behavior, by designing an approach introducing ternary parameters that account for an accurate prediction of the of slag.

3. From the analysis of available data, the mass transfer ratio of Fe/FeO influences the aluminum leakage in the steel. The results support the increase in the mass transfer

ratio of FeO/Fe from 0.008 to 0.15, and reduces the leakage of aluminum in the steel-slag system.

4. Analysis of available thermodynamic data shows that manganese aluminate spinel should not be expected to form during ladle treatment of high manganese steel. The major inclusion types are MnS (Manganese Sulphide), AlN (Aluminum Nitride), Al_2O_3 (Alumina), and $MgAl_2O_4$ (Magnesium Aluminate spinel).

5. Based on the calculations from the coupled kinetic model for slag-steel-MnS inclusions, the formation of MnS inclusions will not be observed at expected levels of manganese and sulphur at steel making temperatures. MnS inclusions observed in steel are likely to have formed during cooling and solidification.

6. Considering the calculation in the coupled kinetic model for slag-steel-AlN inclusions, presence and growth of inclusions are observed in the molten steel.

5.3 Future work

This project work resulted in increased knowledge about the operation and inclusions present in the ladle metallurgy furnace for high manganese steel. Identified topics which require further research are summarized below as**:**

1. The modification of the slag-steel-inclusion kinetic model, in order to introduce the effects of atmospheric reoxidation and nitrogen pickup during the periods of high gas stirring, when the steel is exposed to the atmosphere. This will have an influence on the presence and growth of inclusions in high manganese steel.

2. More work has to be carried out in determining the percentage of manganese in the

steel, which causes the conversion of the Henrian reference state to Raoultian reference state in the thermodynamic calculations. Henrian reference state corresponds to 1 weight percentage of standard state with Fe used as a solvent, then the validity of thermodynamic parameters (Henrian activity coefficients and interaction parameters) can be only limited in a Fe-rich solution, rather than in a wide range of solutions. This could lead to the usage of Raoultian reference state for non-dilute solutions. Additions for high manganese weight percentage in the steel, during the ladle refining process, could lead to the usage of a Raoultian reference state in thermodynamic calculations.

3. One of the major challenges in the usage of UIPF (Unified Interaction Parameter Formalism), are the several primary and secondary interaction parameters for high manganese steel that have either not been published and/or evaluated for high alloy contents in the steel. Further work should focus on evaluating these required parameters for high manganese, aluminum, and silica contents in the steel.

4. Further work is required to provide a complete description of the changes in the mass transfer coefficients of FeO, MnO, and SiO_2 in the slag. The mass transfer ratios and determination of those values, based on the industrial sampling analysis of steel, slag and inclusions, could provide significant information on this topic.

5. Extend the present kinetic model available for the growth of MnS and AlN inclusions, to include a kinetic model for the nucleation of inclusions. In addition to the present inclusions, supplementary introduction of other major inclusions such as alumina (Al_2O_3), and complex inclusions in the coupled kinetic model for high

manganese steel, could lead to the robust nature of the kinetic model.

6. The leakage of aluminum from desulphurization in the slag-steel kinetic model is insignificant and known from the analysis. Work has to be performed in estimating the exact source of the leakage of aluminum during the desulphurization process.

7. Further research has to be carried out in determining the number of particles from the area fraction of inclusion to the volume fraction of inclusion, from the inclusion analysis. This helps with establishing a thorough understanding of the inclusion behavior, during the process in the ladle metallurgy furnace, for high manganese steel.

8. Future work has to be performed on including the gas system in the slag-steel reaction model, since large amounts of ferromanganese additions are carried out in making high manganese steel, and manganese has high volatility. Moreover, the coupling of gas systems will further improve the predictability of the coupled multicomponent slag-steel-inclusion model for high manganese steel.

References:

Andersson, M., Hallberg, M., Jonsson, L., & Jönsson, P. (2002). Slag-metal reactions during ladle treatment with focus on desulphurisation. *Ironnmaking & Steelmaking*, *29*(3), 224–232.

Andrew, J. H., Maddocks, W. R., & Fowler, E. A. (1931). Equilibrium of the Systems MnS-MnO, MnS-MnSiOa and MnS-Fe; SiOi. *J. Iron Steel Inst.*, *124*, 295–325.

Asai, S., Kawachi, M., & Muchi, I. (1983). Mass Transfer Rate in Ladle Refining Processes. *SCANINJECT III, 3rd International Conference on Injection Metallurgy*, pp. 12:1–12–29.

Aydin, H., Essadiqi, E., Jung, I. H., & Yue, S. (2013). Development of 3rd generation AHSS with medium Mn content alloying compositions. *Materials Science and Engineering A*, *564*, 501–508. http://doi.org/10.1016/j.msea.2012.11.113

Bale, C. W., & Pelton, A. D. (1990). The Unified Interaction Parameter Formalism" Thermodynamic Consistency and Applications. *METALLURGICAL TRANSACTIONS A*, *21A*.

Bartlett, L., & Van Aken, D. (2014). High Manganese and Aluminum Steels for the Military and Transportation Industry. *Jom*, *66*(9), 1770–1784.

Billur, F., Dykeman, J., & Altan, T. (2014). Three generations of advanced high strength steels for automotive applications, Part III. *Stamping Journal*, (December 2013).

Bolgar, A. S., Gordienko, S. P., Ryklis, E. A., & V.V. Fesenko: Khim. Fiz. Nitridov, G.V.

Samsonov, E. (1968).*Naukova Dumka, Kiev*, 151–56.

Bouaziz, O., Zurob, H., & Huang, M. (2013). Driving force and logic of development of advanced high strength steels for automotive applications. *Steel Research International*, *84*(10), 937–947.

Chase, M. W. (1998). *Jr: NIST-JANAF Thermochemical Tables*.

Chin, K., Cho, W. T., Kim, S. K., Kim, Y., Song, T. J., & Kim, T. (2015). Development of TWIP steel in POSCO Contact data Summary 1 . Mechanical properties of TWIP steel 2 . Hydrogen Delayed Fracture (HDF) of TWIP Steels 3 . Galvanizability and Weldability of TWIP steel, (June), 65–68.

Choi, J. K., Lee, S.-G., Park, Y.-H., Han, I.-W., & Morris Jr., J. W. (2012). High Manganese Austenitic Steel For Cryogenic Applications. *The Twenty-Second International Offshore and Polar Engineering Conference*, *4*, 29–35.

Choudhary, S. K., & Ghosh, A. (2008). Thermodynamic Evaluation of Formation of Oxide–Sulfide Duplex Inclusions in Steel. *ISIJ International*, *48*(11), 1552–1559.

Choudhary, S. K., & Ghosh, A. (2009). Mathematical Model for Prediction of Composition of Inclusions Formed during Solidification of Liquid Steel. *ISIJ International*, *49*(12), 1819–1827.

Cicutti, C., Valdez, M., Perez, T., Petroni, J., Gomez, A., Donayo, R., & Ferro, L. (2000). Study of slag-metal reactions in an LD-LBE converter. *6th International Conference on Molten Slags, Fluxes and Salts,* 367.

Coughlin, J. P., & Am., J. (1950). *Chem. Soc*, (72), 5445–5447.

Darken, L. S. (1967). Thermodynamics of binary metallic solutions. *AIME MET SOC TRANS*, *239*(1), 90–96.

Deo, B., & Boom, R. (1993). *Fundamentals of Steelmaking Metallurgy*.

E.T.Turkdogan. (1975). BOF Steelmaking,RD Pehlke, WF Porter, RF Urban and JM Gaines, eds. *Iron Steel Soc. AIME*.

Evans, D. B., & Pehlke, R. D. (1964). *Trans. Met. Soc. AIME*, *230*, 1651–56.

Galindo, A., A. Irons, G., S.Coley, K., & Sun, S. (2015). *KINETICS OF THE FORMATION OF MAGNESIUM ALUMINATE INCLUSIONS*.

Gaye, H., & Welfringer, J. (1984). Modelling of the thermodynamic properties of complex metallurgical slags. *Second International Symposium on Metallurgical Slags and Fluxes*.

Ghosh, A. (2001). *SECONDARY Principles and Applications*. *New York*.

Gigacher, G., Pierer, R., Wiener, J., & Bernhard, C. (2006). Metallurgical aspects of casting high-manganese steel grades. *Advanced Engineering Materials*, *8*(11), 1096–1100.

Glasser, O. (1926). *Centralbl. Mineral. Geol. Palaeontol. Abh. Abt*, *A*, 81–96.

Grajcar, A., Galisz, U., & Bulkowski, L. (2011). Non-metallic inclusions in high manganese austenitic alloys. *Archives of Materials Science and Engineering*, *50*(1),

21–30.

Grajcar, A., Galisz, U., Bulkowski, L., Opiela, M., & Skrzypczyk, P. (2012). Modification of Non-metallic Inclusions in High-strength Steels Containing Increased Mn and Al Contents. *Journal of Achievements in Materials and Manufacturing Engineering*, *55*(2), 245–255.

H. Gaye, & J. Lehmann. (1997). Modelling of Slag Thermodynamic Properties From Oxides to Oxisulphides. *MOLTEN SLAGS, FLUXES AND SALTS '97 CONFERENCE*, 27–32.

Hao, X., & Wang, X. (2015). A New Sulfide Capacity Model for CaO-Al2O3 -SiO2 - MgO Slags Based on Corrected Optical Basicity. *Steel Research International*, *87*(3), 359–363.

Harada, A., Maruoka, N., Shibata, H., & Kitamura, S. (2013). A Kinetic Model to Predict the Compositions of Metal, Slag and Inclusions during Ladle Refining: Part2. Condition to Control the Inclusion Composition. *ISIJ International*, *53*(12), 2118–2125.

Helmut, L., Xie, Y., Thorsten, B., & Wolfgang, P. (2003). Slag emulsification during liquid steel desulphurisation by gas injection into the ladle. *Steel Research International*, *74*, 77–85.

Hildenbrand, D. L., & Hall, W. F. (1963). The Vapourization Behavior of Boron Nitride and Aluminum Nitride. *J. Phys. Chem*, *67*, 888–93.

Hillert,] M., & Staffansson, L. (1976). A thermodynamic analysis of the phase equilibria in the Fe-Mn-S system. *Metall. Trans. B*, (7), 203–211.

Hils, G., Newirkowez, A., Kroker, M., Grethe, U., Schmidt-Jrgensen, R., Kroos, J., & Spitzer, K. H. (2015). Conventional and tailored Mn-bearing alloying agents for the production of high manganese steel. *Steel Research International*, *86*(4), 411–421.

Hino, M., & Ito, K. (2010). *Thermodynamic Data for Steelmaking*.

I.Barin, O.Knacke, & O.Kubaschewski. (1973). *Thermochemical properties of inorganic substances*.

Jung, I. H., Kang, Y.-B., Decterov, S., & Pelton, A. D. (2004). Thermodynamic Evaluation and Optimization of the MnO-Al2O3 and MnO-Al2O3-SiO2 Systems and Applications to Inclusion Engineering. *Metallurgical and Materials Transactions B*, *35*(April), 259–268.

K.J.Graham, & A. Irons, G. (2008). *Integrated ladle metallurgy control*.

K.Takahashi, & M.Hino. (2000). Equilibrium between Dissolved Mn and O in Molten High-Manganese Steel. In *High Temp.Mater.Proc.*, (p. 1).

Kalisz, D., Lelito, J., Szucki, M., Suchy, J. S., & Gracz, B. (2015). Modeling of MnS precipitation during the crystallization of grain oriented silicon steel. *Metalurgija*, *54*(1), 139–142.

Kalisz, D., & Rzadkosz, S. (2013). Modeling of the Formation of AlN Precipitates During Solidification of Steel. *Archives of Foundry Engineering*, *13*(1), 63–68.

Kang, S. E., Tuling, A., Banerjee, J. R., Gunawardana, W. D., & Mintz, B. (2011). Hot ductility of TWIP steels. *Materials Science and Technology*, *27*(1), 95–100.

Kang, Y. B. (2010). Critical evaluations and thermodynamic optimizations of the Mn-S and the Fe-Mn-S systems. *Calphad: Computer Coupling of Phase Diagrams and Thermochemistry*, *34*(2), 232–244.

Kang, Y., Sahebkar, B., Scheller, P. R., Morita, K., & Sichen, D. (2011). Observation on Physical Growth of Nonmetallic Inclusion in Liquid Steel during Ladle Treatment. *Metallurgical and Materials Transactions B*, *42*(3), 522–534.

Kang, Y.-B., Chang, C.-H., Park, S.-C., Kim, H.-S., Jung, I.-H., & Lee, H.-G. (2005). Thermodynamics of Inclusions Engineering in Steelmaking and Refining. *ICS 2005 - The 3rd International Congress on the Science and Technology of Steelmaking*, *3*(8), 154–162.

Kapoor, M. L., & Frohberg, M. G. (1971). Theoretical treatment of activities in silicate melts.

Kiessling, R. (1980). Critical assessment Clean steel - a debatable concept. *Metal Science*, (May), 161–172.

Kim, H. S., Lee, H.-G., & Oh, K.-S. (2001). MnS precipitation in association with manganese silicate inclusions in Si/Mn deoxidized steel. *Metallurgical and Materials Transactions A*, *32*(6), 1519–1525.

Kim, W.-Y., Kang, J.-G., Park, C.-H., Lee, J.-B., & Pak, J.-J. (2007). Thermodynamics of

Aluminum, Nitrogen and AlN formation in Liquid Iron. *ISIJ International*, *47*(7), 945–954.

Kitamura, S., Kitamura, T., Shibata, K., Mizukami, Y., Mukawa, S., & Nakagawa, J. (1991). Effect of Stirring Energy, Temperature and Flux Composition on Hot Metal Dephosphorization Kinetics. *ISIJ International*, *31*(11), 1322–1328.

Lai, W. B., Yu, J. K., Du, C. M., Zhang, L., & Wang, X. L. (2015). Refinement of inclusions in molten steel by electric current pulse. *Materials Science and Technology*, *31*(13), 1555–1559.

Lehmann, J., & Nadif, M. (2011). Interactions Between Metal and Slag Melts: Steel Desulfurization. *Reviews in Mineralogy and Geochemistry*, *73*, 493–511.

Lehmann, J., & Zhang, L. (2010). The generalized central atom for metallurgical slags and high alloyed steel grades. *Steel Research International*, *81*(10), 875–879.

Li, H., Morris, A. E., & Robertson, D. G. C. (1998). Thermodynamic Model for MnO-Containing Slags and Gas- Slag-Metal Equilibrium in Ferromanganese Smelting, *29*, 1181–1191.

Liu, H., Liu, J., Michelic, S., Wei, F., Zhuang, C., Han, Z., & Li, S. (2016). Characteristics of AlN inclusions in low carbon Fe–Mn–Si–Al TWIP steel produced by AOD-ESR method. *Ironmaking & Steelmaking*, *43*(3), 1743281215Y.000.

Liu, Z., Gu, K., & Cai, K. (2002). Mathematical model of sulfide precipitation on oxides during solidification of Fe-Si alloy. *ISIJ International*, *42*(9), 950–957.

Margules, M. (1895). Über die Zusammensetzung' der gesättigten Dämpfe von Mischungen. *Sitz-Ber. Math.-Naturw. KI. Bayer. Akad. Wiss. Miinchen Lla*, *104*, 1243.

Miettinen, J., & Hallstedt, B. (1998). Thermodynamic assessment of the Fe-FeS-MnS-Mn system. *Calphad*, *22*(2), 257–273.

Mills, K. C. (1974). *Thermodynamic Data for Inorganic Sulphides, Selenides and Tellurides*.

Nagata, K., Ono, Y., Ejima, T., & Yamamura, T. (1988). Chapter 7 - Diffusion. In Y. Kawai & Y. Shiraishi (Eds.), Handbook of Physico-chemical Properties at High Temperatures. In *Handbook of Physico-chemical Properties at High Temperatures. Tokyo: ISIJ*.

Nzotta, M. M., Sichen, D., & Seetharaman, S. (1999). A study of the sulfide capacities of iron-oxide containing slags. *Metallurgical and Materials Transactions B*, *30*(5), 909–920.

Oeters, F. (1994). *Metallurgy of Steelmaking*.

Ohtani, H., Oikawa, K., & Ishida, K. (2000). Optimization of the Fe-rich Fe-Mn-S ternary phase diagram. *High-Temperature Materials and Processes*, *19*(3-4), 197–210.

Oikawa, K., Ishida, K., & Nishizawa, T. (1997). Effect of Titanium Addition on the Formation and Distribution of MnS Inclusions in Steel during Solidification. *ISIJ International*, *37*(4), 332–338.

Oikawa, K., Ohtani, H., Ishida, K., & Nishizawa, T. (1995). The Control of the Morphology of MnS Inclusions in Steel during Solidification. *ISIJ International*, *35*(4), 402–408.

Ollette. (1961). Physical chemistry of process metallurgy, Part 2, GR St-Pierre, ed. *Interscience, Part 2*, 1065.

P.T. Carter, & Macfarlane, T. G. (1957). Thermodynamics of Slag systems. *J. Iron Steel Inst. (London)*, *185*, 54–66.

Paek, M., Jang, J., Jiang, M., & Pak, J. (2013). Thermodynamics of AlN Formation in High Manganese-Aluminum Alloyed Liquid Steels, *53*(6), 973–978.

Paek, M. K., Chatterjee, S., Pak, J. J., & Jung, I. H. (2016). Thermodynamics of Nitrogen in Fe-Mn-Al-Si-C Alloy Melts. *Metallurgical and Materials Transactions B: Process Metallurgy and Materials Processing Science*, *47*(2), 1–20.

Paek, M.-K., Jang, J.-M., Kang, H.-J., & Pak, J.-J. (2013). Reassessment of AlN(s)=Al+N Equilibration in Liquid Iron. *ISIJ International*, *53*(3), 535–537.

Park, J. H., Kim, D. J., & Min, D. J. (2012). Characterization of nonmetallic inclusions in high-manganese and aluminum-alloyed austenitic steels. *Metallurgical and Materials Transactions A: Physical Metallurgy and Materials Science*, *43*(7), 2316–2324.

Pelton, A. D., & Bale, C. W. (1986). A modified interaction parameter formalism for non-dilute solutions. *METALLURGICAL TRANSACTIONS A*, *17*(July), 2–6.

Pelton, A. D., & Chartrand, P. (2001). Solutions, *32*(June).

Pianosi, F., Beven, K., Freer, J., Hall, J. W., Rougier, J., Stephenson, D. B., & Wagener, T. (2016). Sensitivity analysis of environmental models: A systematic review with practical workflow. *Environmental Modelling & Software*, *79*, 214–232.

Pluschkell, W. (1981). Grundoperationen Pfannenmetallurgishcher Prozesse. *Stahl Und Eisen*, *101*(13-14), 97–103.

R.W.Young, J.A.Duffy, G.J.Hassall, & Z.Xu. (1992). Use of optical bascity concept for determining phospohorous and sulphur-metal partitions. *Ironmaking & Steelmaking*, *19*, 202–219.

Rao, B. K. D. P., & Gaskell, D. R. (1981). The thermodynamic activity of MnO in melts containing SiO2, B2O3, and TiO2. *Metall. Trans. B*, *12B*, 311–17.

Robertson, D. G. C. (1995). The Computation of the Kinetics of Reactions between Multiple Phases. In *EPD Congress, The Minerals, Metals & Material Society* (pp. 347–361).

Robertson, D. G. C., B.Deo, & S.Ohguchi. (1984). Multicomponent mixed-transport-control theory for kinetics of coupled slag_metal and slag_metal_gas reactions_ application to de-S of molten iron_Robertson,Deo(IMSM,'84).pdf. *Ironmaking & Steelmaking*, *11*(1).

Roehl, G. (1913). About Sulfide Inclusions in Iron and Steel: A Contribution to the Theory of Desulphurization of Irons. *Stahl Eisen*, *33*, 565–567.

S.Kim, H., Lee, H.-G., & OH, K.-S. (2000). Precipitation behavior of MnS on oxide inclusions in Si/Mn deoxidized steel. *METALS AND MATERIALS*, *6*(4), 305–310.

Saridikmen, H., Kucukkaragoz, C. S., & Eric, R. H. (2007). Sulphur behaviour in ferromanganese melting. In *INFACON XI* (Vol. 2, p. 10).

Sawamura:, K. (1962). Activity of Lime in Blast furnace Type slags. *Tetsu-to-Hagane´ Overseas*, *2*, 219–25.

Seetharaman, S., Mclean, A., Guthrie, R., & Sridhar, S. (2000). *Treatise on Process metallurgy, process fundamentals*. *Elsevier publication* (Vol. 1).

Shannon, G. N., & Sridhar, S. (2005). Modeling Al2O3 Inclusion Separation across Steel–Slag Interfaces. *Scandinavian Journal of Metallurgy*, *34*, 353–362.

Sharma, R. A., & Richardson, F. D. (1962). Activities of lime-alumina melts. *J. Iron Steel Inst. (London), 200*, 373–79.

Shibata, Z. (1928). The equilibrium diagram of the iron sulphide-manganese sulphide system. *Tech. Rep. Tohoku Imp. Univ, 7*, 279_289.

Silverman, E. N. (1961). *Trans. Metall. Soc*, (AIME 221), 512–517.

Sosinsky, D., Sommerville, I., & McLean, A. (1986). Sulphide, Phosphate, Carbonate and Water Capacities of Metallurgical Slags. In *Process Technology Proceedings*.

Srinivasan, C. R. (1989). In *National Seminar on Secondary Steelmaking* (p. 15).

Staffansson, L. I. (1976). On the Mn-MnS phase diagram. *Metallurgical Transactions B*,

7(1), 131–134.

Szekely, J., & Themelis, N. (1971). *Rate phenomena in process metallurgy*.

Tix, A. (1956). *J. Metals*, *8*, 420.

Vedani, M., Dellasega, D., & Mannuccii, A. (2009). Characterization of Grain-boundary Precipitates after Hot-ductility Tests of Microalloyed Steels. *ISIJ International*, *49*(3), 446–452.

Wagner, C. (1952). Thermodynamics of Alloys. *Addison-Wesley*, 47–51.

Wagner, C. (1962). Thermodynamics of Alloys. *Addison-Wesley*, p. 51.

Wakoh, M., Sawai, T., & Mizoguchi, S. (1996). Effect of S Content on the MnS Precipitation in Steel with Oxide Nuclei. *ISIJ International*, *36*(8), 1014–1021.

Wang, Y.-N., Yang, J., Wang, R.-Z., Xin, X.-L., & Xu, L.-Y. (2016). Effects of Non-metallic Inclusions on Hot Ductility of High Manganese TWIP Steels Containing Different Aluminum Contents. *Metallurgical and Materials Transactions B.*

Wei, J., Liu, Z., & Cai, K. (2002). A Coupled Mathematical Model of Microsegregation and Inclusion Precipitation during Solidification of Silicon Steel. *ISIJ International*, *42*(9), 958–963.

Xin, X. L., Yang, J., Wang, Y. N., Wang, R. Z., Wang, W. L., Zheng, H. G., & Hu, H. T. (2015). Effects of Al content on non-metallic inclusion evolution in Fe–16Mn– x Al–0.6C high Mn TWIP steel. *Ironmaking & Steelmaking*.

Yan, P., Guo, M., & Blanpain, B. (2014). In situ observation of the formation and interaction behavior of the Oxide/Oxysulfide inclusions on a liquid iron surface. *Metallurgical and Materials Transactions B*, *45*(3), 903–913.

Yin, H. (2006). Inclusion characterization and thermodynamics for high-Al advanced high-strength steels. *Iron and Steel Technology*, *3*(6), 64–73.

Zhang, G.-H., Chou, K.-C., & Pal, U. (2013). Estimation of Sulfide Capacities of Multicomponent Slags using Optical Basicity. *ISIJ International*, *53*(5), 761–767.

Zhang, L., & Lehmann, J. (2004). Application of the generalised central atom model to sulphur containing oxide slags.

Zhang, L., Sun, S., & Jahanshahi, S. (2007). An Approach to Modeling Al2O3 Containing Slags with the Cell Model. *Journal of Phase Equilibria and Diffusion*, *28*(1), 121–129.

Zhang, X. F., Lu, W. J., & Qin, R. S. (2013). Removal of MnS inclusions in molten steel using electropulsing. *Scripta Materialia*, *69*(6), 453–456.

Zhuang, C., Liu, J., Mi, Z., Jiang, H., Tang, D., & Wang, G. (2014). Non Metallic Inclusions in TWIP Steel. *Steel Research International*, *85*(10), 1432–1439.